CHEMICAL REVIEWS

Review

Cite This: Chem. Rev. XXXX, XXX, XXX−XXX

pubs.acs.org/CR

Nanoscale Phenomena in Lithium-Ion Batteries

Sung-Kyun Jung,[†,‡,∥] Insang Hwang,[†,∥] Donghee Chang,[†,∥] Kyu-Young Park,[†,∥] Sung Joo Kim,[†] Won Mo Seong,[†] Donggun Eum,[†] Jooha Park,[†] Byunghoon Kim,[†] Jihyeon Kim,[†] Jae Hoon Heo,[†] and Kisuk Kang*[,†,‡,§]

[†]Department of Materials Science and Engineering, Research Institute of Advanced Materials (RIAM), Seoul National University, Gwanak-ro 1, Gwanak-gu, Seoul 151-742, Republic of Korea

[‡]Center for Nanoparticle Research, Institute for Basic Science (IBS), Seoul National University, Gwanak-ro 1, Gwanak-gu, Seoul 151-742, Republic of Korea

[§]Institute of Engineering Research, College of Engineering, Seoul National University, 1 Gwanak-ro, Gwanak-gu, Seoul 151-742, Republic of Korea

ABSTRACT: The electrochemical properties and performances of lithium-ion batteries are primarily governed by their constituent electrode materials, whose intrinsic thermodynamic and kinetic properties are understood as the determining factor. As a part of complementing the intrinsic material properties, the strategy of nanosizing has been widely applied to electrodes to improve battery performance. It has been revealed that this not only improves the kinetics of the electrode materials but is also capable of regulating their thermodynamic properties, taking advantage of nanoscale phenomena regarding the changes in redox potential, solid-state solubility of the intercalation compounds, and reaction paths. In addition, the nanosizing of materials has recently enabled the discovery of new energy storage mechanisms, through which unexplored classes of electrodes could be introduced. Herein, we review the nanoscale phenomena discovered or exploited in lithium-ion battery chemistry thus far and discuss their potential implications, providing opportunities to further unveil uncharted electrode materials and chemistries. Finally, we discuss the limitations of the nanoscale phenomena presently employed in battery applications and suggest strategies to overcome these limitations.

CONTENTS

Special Issue: Beyond Li Battery Chemistry

Received: June 28, 2019

DOI: 10.1021/acs.chemrev.9b00405
Chem. Rev. XXXX, XXX, XXX−XXX

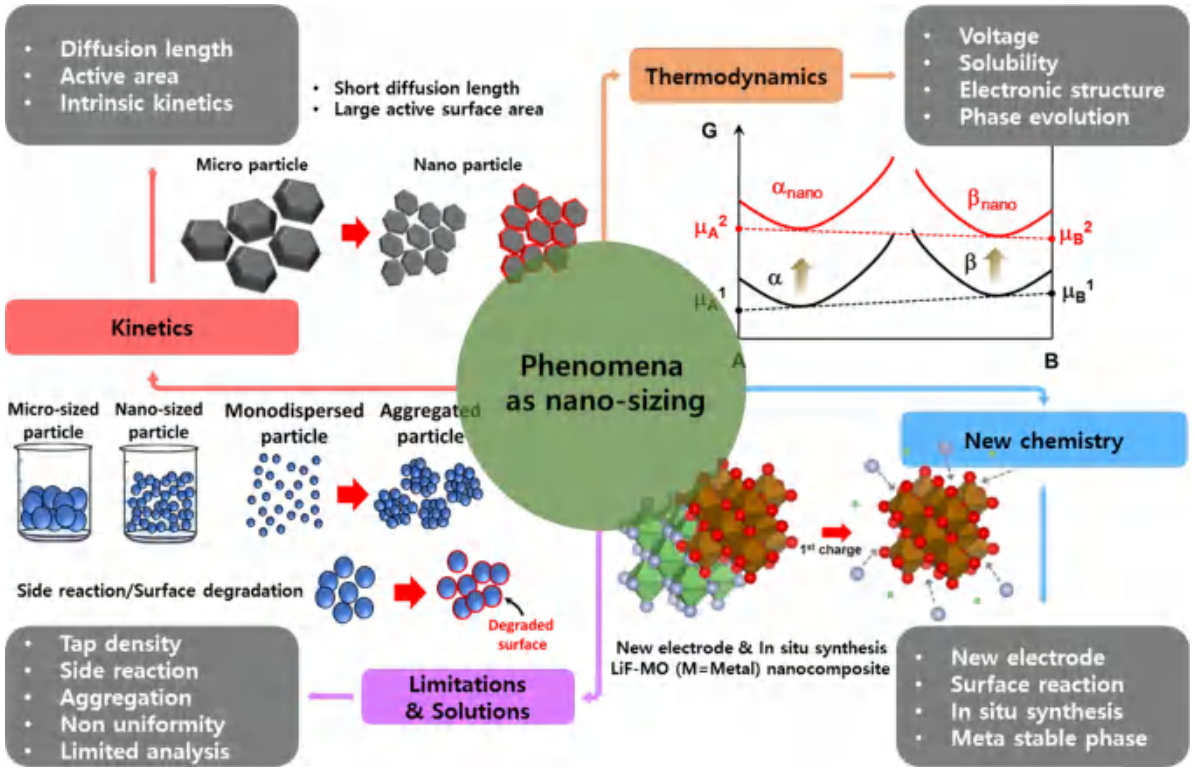

Figure 1. Nanosizing phenomena of electrode materials in battery science.

1. INTRODUCTION

The emergence of lithium-ion batteries (LIBs), energy storage systems with high energy density, has enabled ubiquitous energy utilization while overcoming the time and space issues of limited energy resources and distribution. With the intense demands of large-scale applications such as electric vehicles, the need for LIBs with higher performance is escalating. Over the past few decades, various electrode reactions have been explored for efficient Li ion storage in electrode materials for LIBs, and their fundamental physical and chemical natures were scrutinized in the hope of maximizing their practical energy and power density. The intrinsic properties of electrode materials that undergo intercalation, conversion, or alloying reactions have been extensively studied with respect to their structural evolution, phase transformations, and ionic/electronic conductivities, which were found to be critically linked to the performance of LIBs. Extrinsic physicochemical factors affecting battery performance such as the size/morphology/assembly of Li host materials have been considered to complement the intrinsic limits of those electrode materials.[1−3]

The strategy of nanosizing was adopted as a facile solution for improving the sluggish diffusion kinetics of Li ions and the limited surface area of conventionally synthesized electrode materials for charge transfer.[3] This led to drastically improved ionic and charge transfer kinetics with enhanced power and cycle performance, opening a new era combining “nano” and “battery” systems. Many reports have successfully demonstrated boosted electrochemical performance through the use of nanomaterials, which is well illustrated by the effects of reduced size/dimensions on battery kinetics.[4] The transition of the dimensions of the Li host material from the micro to the nano scale not only enhances the kinetics but also often leads to a thermodynamic change in the battery reactions, a newly observed phenomenon (Figure 1). The higher surface-area-to-volume ratio of nanomaterials significantly alters the free energy of the bulk state,[5] resulting in modified thermodynamic properties in terms of chemical potentials, defect solubility, and electronic structure, which are tied to the energy density, reaction path, and redox properties of battery materials.[6−8] These nanoscale phenomena also opened a path to discovering novel energy storage mechanisms and enabled the design of new types of electrodes.[9] For example, the decoupling of electron and ion storage in nanocomposites has been suggested as a way to overcome the limitations of current intercalation materials, and new energy storage mechanisms are continuously being uncovered.[10,11] Most recently, nanoscale phenomena have been exploited to explore nonground-state thermodynamics for the design of metastable materials.[12] Mechanochemical reactions at the nanoscale have allowed the design of rock-salt-type cathodes with percolated lithium diffusion and anion redox capability.[13−16] Exploration of these new nanoscale phenomena could offer novel ways to tackle the current borders of LIB chemistry and aid in their better understanding.

Herein, we review the various approaches to exploiting nanoscale materials that have been employed in LIB chemistry,

DOI: 10.1021/acs.chemrev.9b00405
Chem. Rev. XXXX, XXX, XXX−XXX

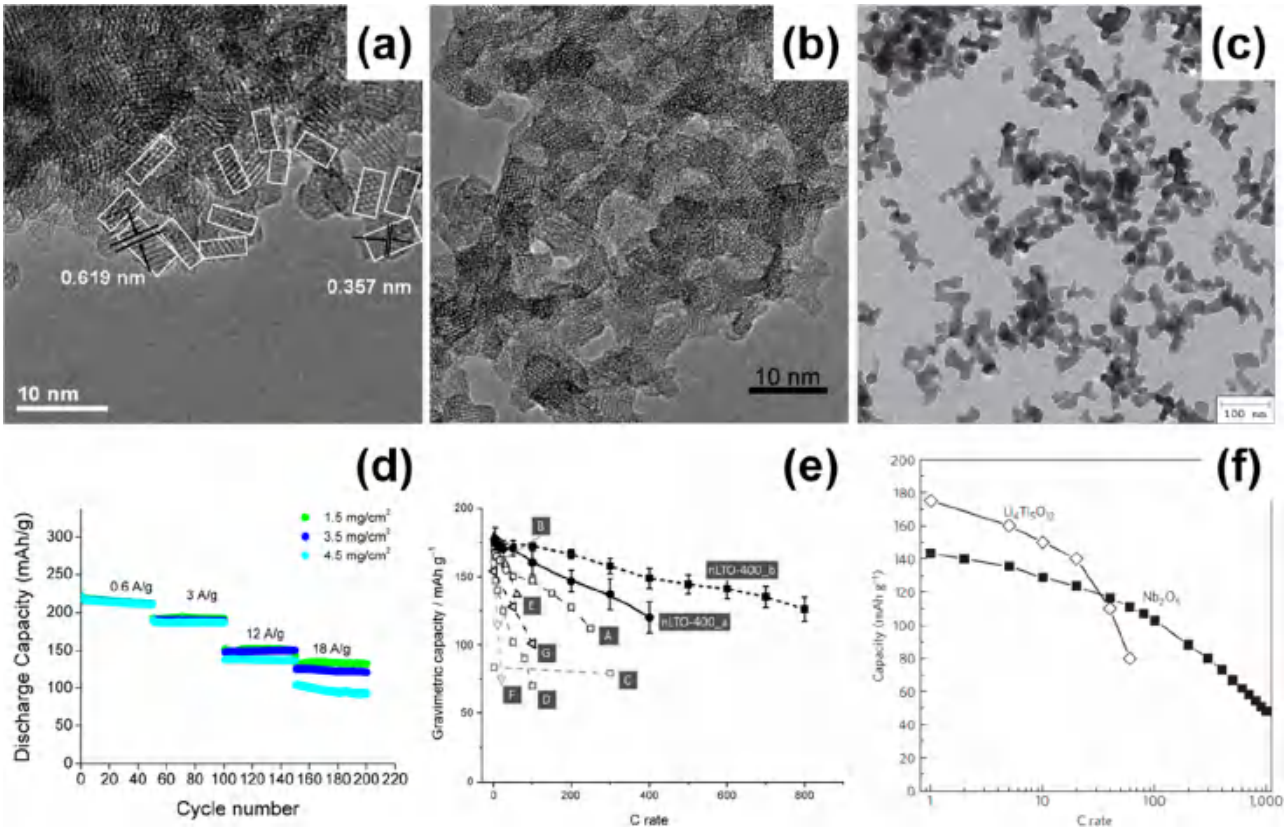

Figure 2. High-resolution TEM images and rate capabilites of half-cells composed of lithium metal and (a,d) nanosized TiO_2(B),[20] (b,e) $Li_4Ti_5O_{12}$,[24] and (c,f) T-Nb_2O_5,[27,28] respectively. Reprinted with permission from refs 20,24,27 Copyright 2011−2012 Wiley-VCH Verlag GmbH & Co. KGaA. Reprinted with permission from ref 28. Copyright 2013 Springer Nature.

from improving specific electrochemical properties to exploring new electrode materials. In addition, we spotlight the potential applicability of nanoscale phenomena and suggest feasible directions for further exploration. The hurdles involved in adopting nanomaterials, such as a low tap density, high cost of synthesis, side reactions at the surface, aggregation among nanoparticles, and nonuniformity of the oxidation state or chemical distribution, are also discussed in relation to real-world applications. Finally, we explain the need for an in-depth understanding of the nanoscale phenomena by introducing state-of-the-art analytical techniques that can be used to overcome the currently limited spatial/time resolution of conventional analysis techniques.

2. PART 1: GENERAL NANOSCALE PHENOMENA: KINETICS, THERMODYNAMICS, AND MECHANICS

2.1. Accelerating the Reaction Kinetics

The nanosizing of electrode materials has most frequently been carried out with the aim of improving their rate capability, which is essential to achieve fast charge/discharge in lithium batteries. Several important phenomena can be expected from the nanosizing of electrode materials, including: (1) reducing the charge-carrier transport path length, (2) enhancing the charge-transfer reaction at the surface, and (3) modifying the material properties by size effects. In this section, we focus mainly on these nanoscale phenomena along with representative examples.

The electrochemical reactions in LIBs generally involve the solid-state diffusion of lithium ions within the electrode material and the transfer of lithium ions at the interface of electrode and electrolyte. The size reduction of the electrode material leads to a decrease of the diffusion length required for the lithium ions and an increase of the interfacial area between the electrode and electrolyte, thereby aiding in improving the rate capability. When charge carriers travel through the bulk of the material, the finite diffusivity induces an increase of the impedance of the electrochemical system. Additionally, the overall electrochemical reaction rate is inversely proportional to the dimension of the electrode material.[17] From Fick's first law of diffusion and random walk theory, the diffusion length L can be defined as

$$L \sim \sqrt{D \times t} \quad (1)$$

where D is the diffusion coefficient of the charge carriers and t is the time required to diffuse into the bulk of the electrode material. Here, to achieve a high charge/discharge capacity, the diffusion coefficient of an electrode material should be high enough for the electrode to complete the reaction. Or, by reducing the particle size, the diffusion time can be shortened, ultimately leading to an improved rate capability for a given material.

There have been a number of reports on the synthesis of nanomaterials of electrodes aimed at the enhancement of power capability. Anode materials have been more actively fabricated with nanostructures than cathode materials, presumably due to their more facile synthetic routes, and examples include TiO_2−bronze (TiO_2(B)),[18−21] $Li_4Ti_5O_{12}$,[22−25] and orthorhombic Nb_2O_5 (T-Nb_2O_5).[26−30] These exemplary anode materials have been of particular

DOI: 10.1021/acs.chemrev.9b00405
Chem. Rev. XXXX, XXX, XXX−XXX

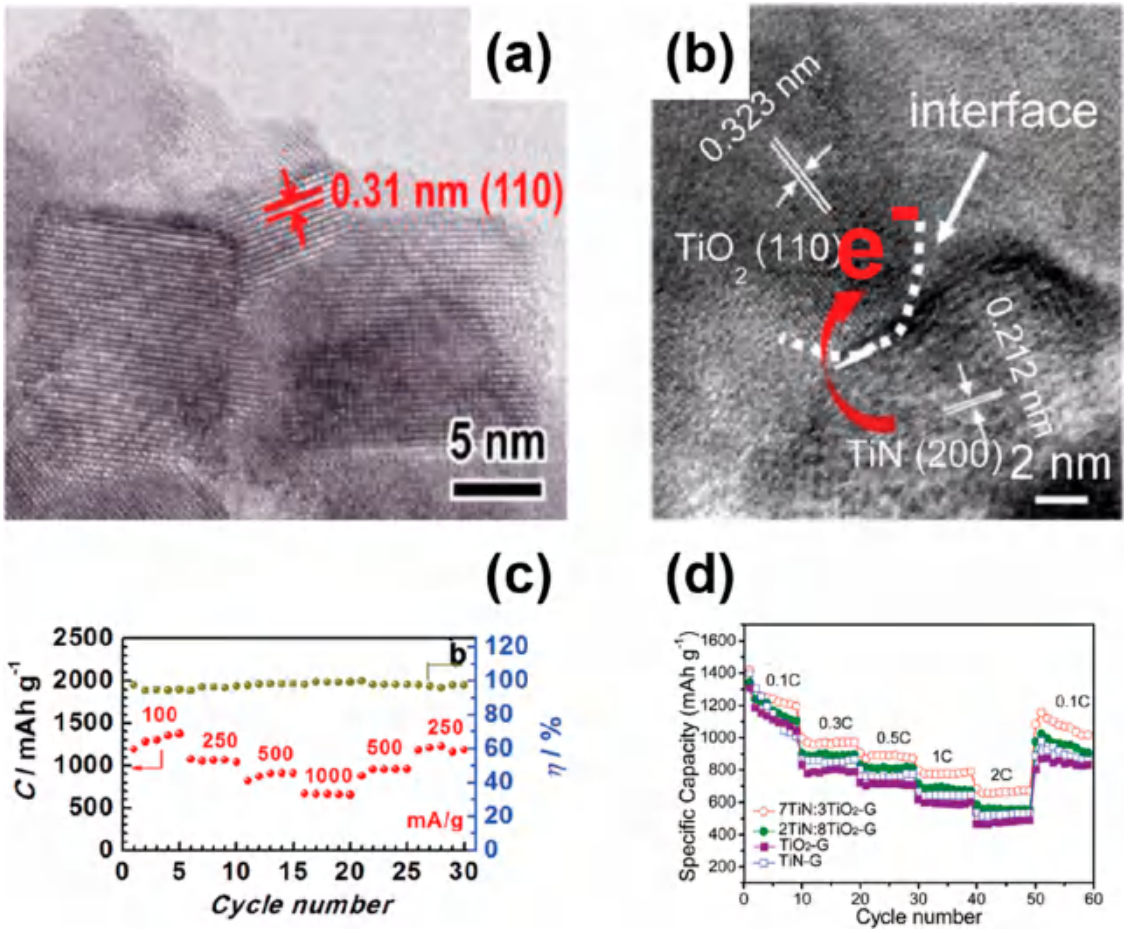

Figure 3. (a,b) High-resolution TEM images of nanosized (a) RuO_2[62] and (b) TiO_2−TiN.[66] (c) Rate capability of a Li−O_2 cell with the cathode framework composed of RuO_2 shown in (a). Reproduced with permission of ref 62. Copyright 2015 Wiley-VCH Verlag GmbH & Co. KGaA (d) Rate capability of Li−S cell with the cathode framework composed of TiO_2−TiN shown in (b). Reproduced with permission of ref 66. Copyright 2017 The Royal Society of Chemistry.

interest as nanosized electrodes due to their stability, which is attributed to them, either forming a robust solid-electrolyte interphase (SEI) layer at the surface or operating in a voltage range that does not induce the formation of a SEI layer.[18,31] Ren et al.[20] reported that TiO_2(B) nanoparticles with sizes of approximately 2.5 × 4.3 nm^2 delivered a capacity of ∼130 mAh g^{-1} at a surprisingly high current density of 18 A g^{-1} (Figure 2a,d). Li et al.[21] succeeded in synthesizing porous TiO_2(B) nanosheets attached to a nanowire, forming a bunched hierarchical structure. This structure provided a lithium storage capacity of 159 mA g^{-1} at a current density of 6.7 A g^{-1} (equivalent to 20 C). The rate capabilities in these two examples are the highest reported for TiO_2 electrodes to date. Spinel $Li_4Ti_5O_{12}$, which is known to undergo a first-order transition upon lithium insertion/deinsertion with a negligible volume change, has also been subject to nanosizing. Feckl et al.[24] synthesized $Li_4Ti_5O_{12}$ with a nanoporous framework with crystalline domains 3−4 nm in size that could endure rates up to 140 A g^{-1} (equivalent to 800 C), delivering 73% of its theoretical capacity (Figure 2b,e); this rate capability is the highest among all $Li_4Ti_5O_{12}$ electrodes reported to date. T-Nb_2O_5 has been reported to operate via a surface-limited lithium insertion reaction, so-called "intercalation pseudocapacitance", enabling low-hindrance migration via unique diffusion path topologies.[30] This allows the rate capability of T-Nb_2O_5 to be even further increased upon nanosizing with large surface areas. Interestingly, a capacity of ∼40 mAh g^{-1} was reported at a rate of 1000 C, even for a thick electrode (40 μm) composed of nanocrystalline T-Nb_2O_5 (Figure 2c,f).[28] Later, Lou et al. also synthesized three-dimensional ordered macroporous T-Nb_2O_5, further improving its rate capability.[29] The nanostructured conversion-reaction electrode materials such as α-Fe_2O_3 and Co_3O_4 also benefit from the nanosizing strategy. While the conversion-reaction itself induces the formation of the nanoparticles during the reaction, the large, tailored reaction surface area obtained from nanostructuring not only compensates for the intrinsically sluggish kinetics but can also suppress the irreversible phase transformations observed in uncontrolled microcrystalline structures.[32−38] Xiao et al.[39] recently reported a rate capability up to 20 A g^{-1} for Co_3O_4 by fabricating hierarchical nanobundles. Guo et al.[35] reported a mesoporous yolk−shell octahedron structure of α-Fe_2O_3 that can endure a rate of 1 A g^{-1}.

Representative cathode materials such as $LiCoO_2$,[40−44] $LiFePO_4$,[42,45−47] and $LiMn_2O_4$[42,48−50] have been also examined in the nanostructured electrodes. For these materials, various morphologies such as nanofibers,[43] nanowires,[47] nanotubes,[50] nanoplates,[42,48] and hierarchical structures[44] have been fabricated and demonstrated to be effective in improving the rate capability. In some cases, the nanostructures were designed along a specific crystallographic direction considering the intrinsic lithium diffusion pathway. For

DOI: 10.1021/acs.chemrev.9b00405
Chem. Rev. XXXX, XXX, XXX−XXX

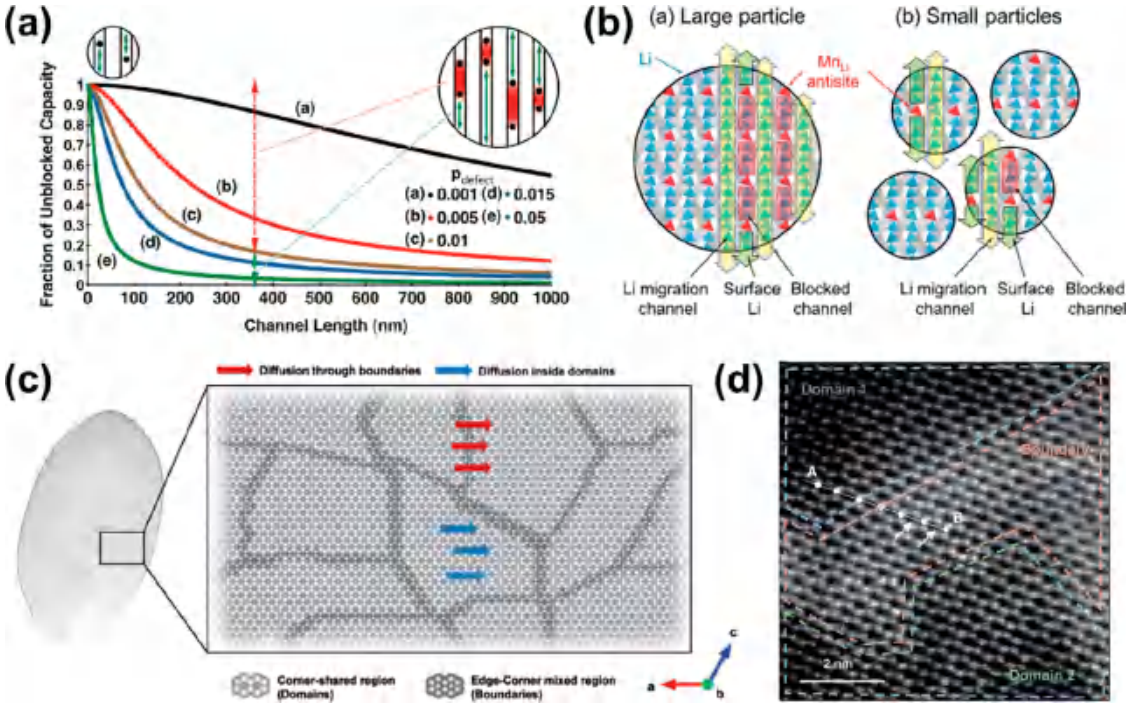

Figure 4. Effect of immobile antisite defects embedded in the one-dimensional lithium transport channels in (a) $LiFePO_4$[51] and (b) $LiMnBO_3$.[70] Reproduced with permission of ref 51. Copyright 2010 American Chemical Society. Reproduced with permission of ref 70. Copyright 2015 Wiley-VCH Verlag GmbH & Co. KGaA. (c) Schematic illustration of the role of an intrinsic nanodomain in $LiFeSO_4F$ and (d) observation of that nanodomain by HAADF-STEM.[69] Reproduced with permission of ref 69. Copyright 2017 Wiley-VCH Verbg GmbH & Co. KGaA.

example, $LiFePO_4$ has open structures with one-dimensional channels in the [010] direction, and Malik et al. reported that the ionic diffusivity can be significantly enhanced by the reduction of the path along the direction, which is vulnerable to the blocking antisite defect.[51] Later, Guo et al. demonstrated that controllable growth of the (010) facet in the synthesis of $LiFePO_4$ leads to an effective enhancement of the charge transfer reaction.[40,52] For spinel electrodes, which have three-dimensional diffusion channels, the crystallographic dependency was less substantial; however, it was shown that truncated octahedral spinel $LiMn_2O_4$ and shape-controlled $LiNi_{0.5}Mn_{1.5}O_4$ could deliver much higher power performance.[53,54]

In addition to conventional transition metal oxide electrodes, other types of electrode materials for post-LIBs have also taken advantage of the nanosizing strategy. For instance, electroactive organic electrodes have been subjected to nanoscaling because of their generally poor electron and lithium-ion transport properties, and size reduction could offer a promising measure to improve the rate capability and to achieve full capacity utilization.[55−58] It was reported that nanosized $Li_4C_8H_2O_6$ could successfully present enhanced reversible capacities and rate capabilities up to 10 C in lithium-ion cells, which is comparable to the results found for conventional electrode materials.[58] Moreover, similar effects could be observed for sodium-containing organic electrodes such as $Na_2C_6O_6$ in sodium-ion cells.[56] Other post-LIB chemistries such as lithium−oxygen (Li−O_2) and lithium−sulfur (Li−S) batteries have benefited from the nanoscale design of current collectors or host materials for discharge products. Considering the low electrical conductivity of the discharge products (Li_2O_2 for the Li−O_2 system or Li_2S for the Li−S system), many researchers have attempted to build a novel nanostructured framework that can provide a large number of reaction sites for discharge products along with an efficient pathway for electron conduction. For instance, nanostructured gold,[59] graphene,[60,61] RuO_2,[62,63] Co_3O_4,[64] and $MnMoO_4$[65] have been employed to achieve high-rate Li−O_2 batteries. Fabrication of a hierarchical structure composed of porous RuO_2 hollow spheres led to an increase of the surface area for the Li_2O_2 deposition, which resulted in a high discharge capacity of 668 mAh g^{-1} even at 1000 mA g^{-1} (Figure 3a,c).[62] For the Li−S system, nanostructured TiO_2−TiN,[66] VN,[67] and carbon nanofibers[68] have been explored to achieve improved rate capability. Yang et al. reported that a nanostructured TiO_2−TiN coating layer (Figure 3b) on a separator promoted LiPS nucleation and allowed fast conversion into insoluble products, resulting in better rate capabilities than Li−S cells with uncoated, and graphene-only coated, TiO_2 cells (Figure 3d).

Unconventional effects of nanosized electrodes were found in work by Malik et al. and Seo et al., who demonstrated that the detrimental role of defects present in the electrode material could be mitigated by size reduction.[51,69] Malik et al.[51] reported that when the diffusion of guest ions follows a one-dimensional path, which does not allow any detours, the path can be simply blocked by immobile point defects such as antisite defects. This finding suggested that nanosizing can be beneficial in reducing the immobile trapped region indicated in red in Figure 4a. Numerical simulations showed that as the channel length decreases, the probability of diffusion channels being blocked by two point defects significantly drops. This phenomenon was demonstrated in several electrode materials with one-dimensional diffusion paths, including $LiFePO_4$[51] and $LiMnBO_3$[70] (Figure 4(a,b), in a combined study of first-principles calculations and experiments. It was noted that this

DOI: 10.1021/acs.chemrev.9b00405
Chem. Rev. XXXX, XXX, XXX−XXX

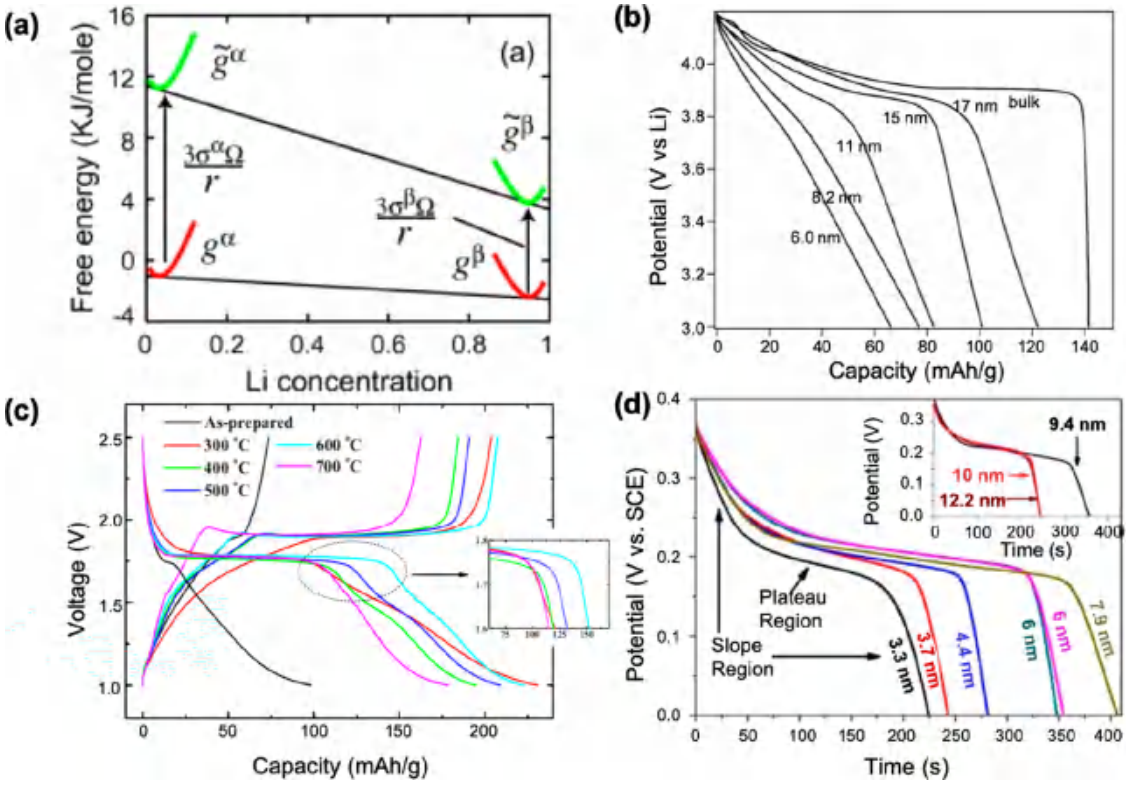

Figure 5. (a) Graphical illustration of particle size and surface free energy effects on Gibbs free energies and transformation chemical potential in α-to-β phase transformation.[5] Reproduced with permission of ref 5. Copyright 2009 Elsevier. (b) The second discharge curves for $LiCoO_2$ of various particle sizes.[40] Reproduced with permission of ref 40. Copyright 2007 American Chemical Society. (c) Third cycle charge−discharge profiles for TiO_2 samples.[78] Reproduced with permission of ref 78. Copyright 2010 The Electrochemical Society. (d) Size dependence of galvanostatic discharge curves of $Ni(OH)_2$ nanoparticles at 1 Ag^{1-}.[79] Reproduced with permission of ref 79. Copyright 2015 Springer Nature.

effect is clearly distinguished from the enhanced rate capability by the simple reduction of diffusion lengths by nanosizing. Another interesting example of mitigation of the influence of defects on the kinetic properties was found from the nanosizing of triplite $LiFeSO_4F$. Seo et al.[69] demonstrated that there exists intrinsic nanodomains in triplite $LiFeSO_4F$ that are composed of two distinct Fe orderings in the crystal. The boundary of the nanodomains contains mixed Fe ordering configuration, which significantly impedes the lithium transport at the domain boundary, resulting in the poor kinetics of $LiFeSO_4F$ (Figure 4c,d). It was demonstrated that the effect of these domain boundaries could be minimized upon reduction of the electrode particles because each electrode particle contains fewer nanodomains, thus reducing the fraction of the diffusion process across the boundary. The nanosized $LiFeSO_4F$ electrode could display both enhanced charge storage capacity and rate capability, whose origin is different from the simple reduction of diffusion lengths by nanosizing.

2.2. Altering the Thermodynamics of Li Storage

Reducing the particle size of the electrode to the nanoscale does not merely modify the reaction rate but can also change the thermodynamic properties of the electrode. It has been frequently reported that the electrochemical profiles of nanostructured electrodes are different from those of bulk systems. For electrode materials that exhibit a first-order phase transition, such as $LiFePO_4$[71] and TiO_2,[72] one of the noticeable effects of nanosizing is the reduction of the miscibility gap, which tends to systematically promote solid-solution-like voltage profiles. Another general phenomenon observed in nanostructured electrode materials is a change of the relative phase stabilities due to non-negligible surface energy contributions. This leads to changes in the apparent voltages exhibited by the electrode materials or in the reaction paths involving intermediate phases during lithiation and delithiation processes. These phenomena are driven by an increase in the surface-to-bulk ratio in nanostructured systems, highlighting the importance of the surface in determining the thermodynamic properties of the electrode. In this section, we will introduce some of the reported theoretical models of nanoscale electrode systems and discuss how the surfaces of electrodes in various morphologies affect the voltage, solubility limit, and overall reaction mechanism.

2.2.1. Tuning the Reaction Voltage. The voltage of a Li electrochemical cell can be described as the relative difference of the Li chemical potentials (μ_{Li}) of the cathode and anode based on the Nernst equation:

$$V = -\frac{\mu_{Li}^{cathode} - \mu_{Li}^{anode}}{e} \quad (2)$$

where e is the electron charge and $\mu_{Li}^{cathode}$ and μ_{Li}^{anode} are the Li chemical potentials of the cathode and anode, respectively. The chemical potential of Li can be defined as

$$\mu_{Li} = \frac{\partial G}{\partial N_{Li}}\bigg|_{T,P,n} = \frac{\partial g}{\partial x} \quad (3)$$

where g is the free energy G normalized by the number of formula units, Li_xM (M is the host material for Li ions). In nanostructured electrodes, the energy of the surface is not

DOI: 10.1021/acs.chemrev.9b00405
Chem. Rev. XXXX, XXX, XXX−XXX

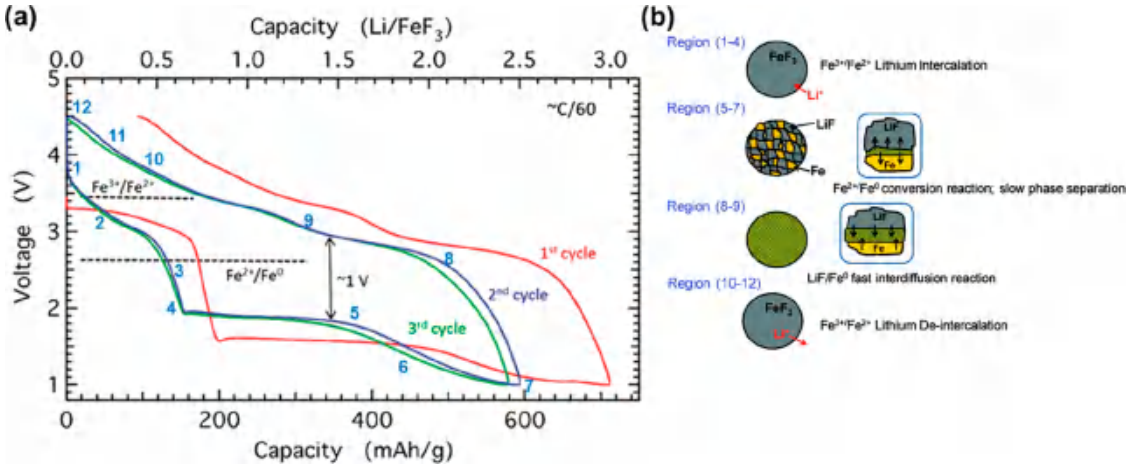

Figure 6. (a) The first three cycles of charge−discharge data of a Li/FeF_3 cell obtained at a rate of C/60. The thermodynamic potentials of the iron reduction from Fe^{3+} to Fe^{2+} and from Fe^{2+} to Fe^0 are shown as dotted lines. (b) Proposed reaction mechanism of the Li/FeF_3 reaction based on the electrochemical data.[83] Reproduced with permission of ref 83. Copyright 2012 American Chemical Society.

negligible in determining the Gibbs free energy, resulting from the increase in the surface-to-bulk ratio. In a theoretical study performed by Van der Ven et al.,[5] the effects of the particle size and surface free energy on the voltage profile were demonstrated upon first-order phase transformation. For spherical electrode crystallites, for instance, with isotropic surface free energy σ, the Gibbs free energy was determined as

$$\tilde{g}(x) = g(x) + \frac{3\Omega\sigma}{r} \quad (4)$$

where Ω is the volume per Li_xM unit and r is the radius of the electrode particle. When the crystallite size r is sufficiently large ($r \rightarrow \infty$), the excess energy from the surface approaches zero and becomes negligible. However, for a small crystallite size, the excess energy from the surface, $\frac{3\Omega\sigma}{r}$, shifts the free energies of the constituting phases (α and β phases in Figure 5a) by an amount depending on the surface properties of each phase.[5] This translates into a deviation of the voltage profile from that of the bulk. The surface energy of the nanoparticles can be quantified using various experimental techniques including contact angle approach, atomic force microscopy (AFM), and inverse gas chromatography. The contact angle approach is the most common method to measure the surface energy, which involves dropping various liquids onto the surface of the material.[73] Alternatively, the adhesion force can be calculated under a quantitative nanomechanical mapping mode using AFM.[74,75] Using the Derjaguin−Muller−Toporov (DMT) model, the surface energy can be extracted using the following relation: $F_{adh} = 2\pi R\Gamma P$, where R is the AFM tip radius, P is the factor with Tabor number, and $\Gamma = 2(\gamma_{tip}\gamma_{sample})^{1/2}$ is the interfacial energy between the tip and the sample (γ denotes the surface energy). Inverse gas chromatography (IGC) can also provide surface energy information.[76,77] In IGC, a column loaded with the sample powder is flowed with the single probe gas, and the surface energy of the sample is calculated based on the retention time of the probe gas molecule physically adsorbed on the solid surface.

Some examples of voltage changes observed for nanosized electrodes are illustrated in Figure 5b−d. Figure 5b presents discharge profiles of $LiCoO_2$ nanoparticles with systematically controlled sizes, indicating a clear correlation between the particle size and the redox potential.[40] Okubo et al. observed that, as the particle size of $LiCoO_2$ decreases from the typical micrometer sizes to 6 nm, the overall electrochemical profiles are significantly altered. Not only is the average voltage lowered, the profile also loses its plateau nature with the slope region increased. This is probably due to the greater fraction of Li storage in the subsurface region of the $LiCoO_2$ particles. A similar result was observed for anatase TiO_2 nanocrystals, as presented in Figure 5c.[78] While the change in the average voltage was not as significant as in the case of $LiCoO_2$, a reduced plateau voltage region is also commonly observed upon decreasing the size of TiO_2 electrode materials. A more precise control of the nanoparticle sizes was gained for $Ni(OH)_2$ nanoparticles from 3.3 to 7.9 nm in Figure 5d.[79] The potential plateau corresponds to the Ni^{2+}/Ni^{3+} redox reaction between $Ni(OH)_2$ and oxidized NiOOH phases, and the plateau region gets shorter with reduction of the particle sizes. Although it was not Li-ion storage in a conventional lithium cell, this study also demonstrated that the voltage displayed is significantly altered with the particle size.

Unlike the intercalation reaction, conversion-reaction electrode materials typically involve the formation of nanoparticle phases during the electrochemical reaction regardless of the initial size of the electrode materials. This is because, in most conversion reactions (e.g., Li + MX ↔ M + LiX), nanosized metallic phases (M) are produced within the matrix of LiX after the discharge. This results in experimental voltages that are often reported to deviate significantly from the equilibrium potential predicted from the Gibbs free energy of the bulk electrode material (by as much as ∼1.0 V).[80−84] Figure 6a presents the first three charge−discharge cycles of a Li/FeF_3 cell with the redox reactions based on Fe^{3+}/Fe^{2+} and Fe^{2+}/Fe^0. According to the proposed reaction mechanism illustrated in Figure 6b, the initial lithiation process occurs via the Li intercalation reaction into FeF_3, which exhibits a voltage that is close to the expected redox potential of Fe^{3+}/Fe^{2+}. However, when reducing Fe^{2+} to Fe^0, the discharge voltage becomes substantially lower than that expected from the bulk reaction. This can be attributed to the formation of nanosized Fe metal particles within a LiF matrix, as schematically shown in Figure 6b. The formation of the nanosized phase adds the excess energy from the large surface areas to the overall reaction, subsequently causing the equilibrium voltage to deviate from that of the bulk reaction.[85] As will be discussed

DOI: 10.1021/acs.chemrev.9b00405
Chem. Rev. XXXX, XXX, XXX−XXX

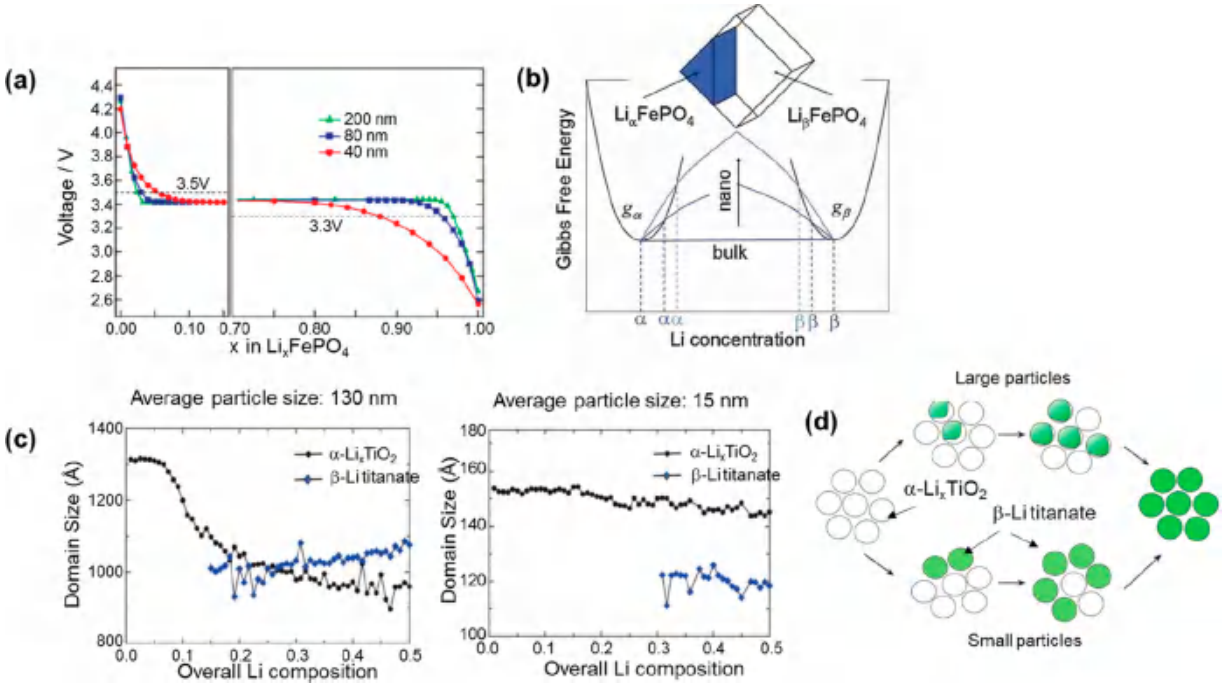

Figure 7. (a) Open-circuit voltage curves for Li_xFePO_4 for mean particle sizes of 200, 80, and 40 nm.[86] Reproduced with permission of ref 86. Copyright 2009 Wiley-VCH Verlag GmbH & Co. KGaA. (b) Schematic illustration of bulk Gibbs free energy resulting from the interfacial energy for the diamond shape, leading to a smaller miscibility gap.[90] Reproduced with permission of ref 90. Copyright 2009 Wiley-VCH Verlag GmbH & Co. KGaA. (c) Domain size evolution of α-Li_xTiO_2 and β-Li-titanate phases for two different particle sizes deduced from in situ XRD line broadening as a function of overall lithium composition. (d) Schematic illustration of the sequential nucleation mechanism for different particle sizes of the TiO_2 electrodes during discharge.[8] Reproduced with permission of ref 8. Copyright 2014 American Chemical Society.

further in section 2.2.3, this also ultimately leads to the kinetic deviation of the reaction pathways.

2.2.2. Changing the Solubility Limit in Intercalation Electrodes. As discussed regarding the change of the electrochemical profile, nanosized electrode materials generally display a shortened plateau voltage region in the two-phase reaction, partly due to the enhanced solubility limit of Li ions in the host. Olivine $LiFePO_4$ is a representative example that exhibits an apparent size-dependent solubility. A microsized $LiFePO_4$ electrode undergoes a two-phase reaction involving heterosite $FePO_4$ and triphylite $LiFePO_4$ during the electrochemical reaction. These two phases coexist in a range of $0.05 < x < 0.99$ for Li_xFePO_4, while either the pure heterosite Li_xFePO_4 ($x < 0.05$) or pure triphylite Li_xFePO_4 ($x > 0.99$) phase is present outside this range. Kobayashi et al. showed that, as the particle size of $LiFePO_4$ decreases below ~40 nm, the one-phase (e.g., heterosite Li_xFePO_4 or triphylite Li_xFePO_4) composition range is extended to $x < 0.12$ and $x > 0.83$, respectively (Figure 7a).[6,71,86] Using neutron and X-ray diffraction (XRD) analyses, it was also confirmed that the solubility limits in heterosite and triphylite phases strongly depend on the particle size.[87] Chen et al.[88] demonstrated that the phase separation leads to anisotropic strain at the interface due to the lattice mismatch between heterosite $FePO_4$ and triphylite $LiFePO_4$. The magnitude of the strain increases at the nanoscale and can potentially result in reduction of the miscibility gap.[89]

According to work by Wagemaker et al.,[90] for a crystallite composed of two-coexisting phases α and β, the free energy should consist not only of the surface energy of each phase α and β but also of the extra energy arising from the interface separating α and β, which can be expressed as

$$G = \frac{V}{\Omega}\varphi_\alpha g_\alpha(x_\alpha) + \frac{V}{\Omega}\varphi_\beta g_\beta(x_\beta) + \sum_i^{\alpha\text{surface}} S_\alpha^i \sigma_\alpha^i + \sum_j^{\beta\text{surface}} S_\beta^j \sigma_\beta^j + \sum_k^{\alpha\beta\text{interface}} A_{\alpha\beta}^k \gamma_{\alpha\beta}^k \quad (5)$$

where V and Ω correspond to the particle volume and volume per Li site, respectively. S^i and σ^i are the surface area and surface energy of the surface i of each phase, respectively. φ_α and φ_β are the fractions of the α and β phases, respectively, that satisfy $\varphi_\alpha + \varphi_\beta = 1$. $\gamma_{\alpha\beta}^k$ corresponds to the interfacial free energy between α and β for interface k having an area of $A_{\alpha\beta}^k$. The equilibrium composition was then determined from the following equilibrium criterion (eqs 6 and 7) for two-phase coexistence, which was derived from eq 5:

$$\mu_\alpha = \mu_\beta \quad (6)$$

$$(g_\alpha - x_\alpha\mu_\alpha) - (g_\beta - x_\beta\mu_\beta) + \frac{\Omega}{V}\left\{\sum_i^{\alpha\text{surface}} \frac{\partial S_\alpha^i}{\partial \varphi_\alpha}(\sigma_\alpha - \sigma_\beta) + \sum_k^{\alpha\beta\text{interface}} \frac{\partial A_{\alpha\beta}^k}{\partial \varphi_\alpha}\gamma_{\alpha\beta}^k\right\} = 0 \quad (7)$$

Accordingly, the effect of the interfacial energy on the miscibility gap and equilibrium composition was demonstrated using first-principles calculations, estimating $\gamma_{\alpha\beta}^k$ between $LiFePO_4$ and $FePO_4$ for a diamond-shaped crystallite, as shown in Figure 7b. For the bulk material, because $1/V$ approaches zero, the excess energy from the surface and

DOI: 10.1021/acs.chemrev.9b00405
Chem. Rev. XXXX, XXX, XXX−XXX

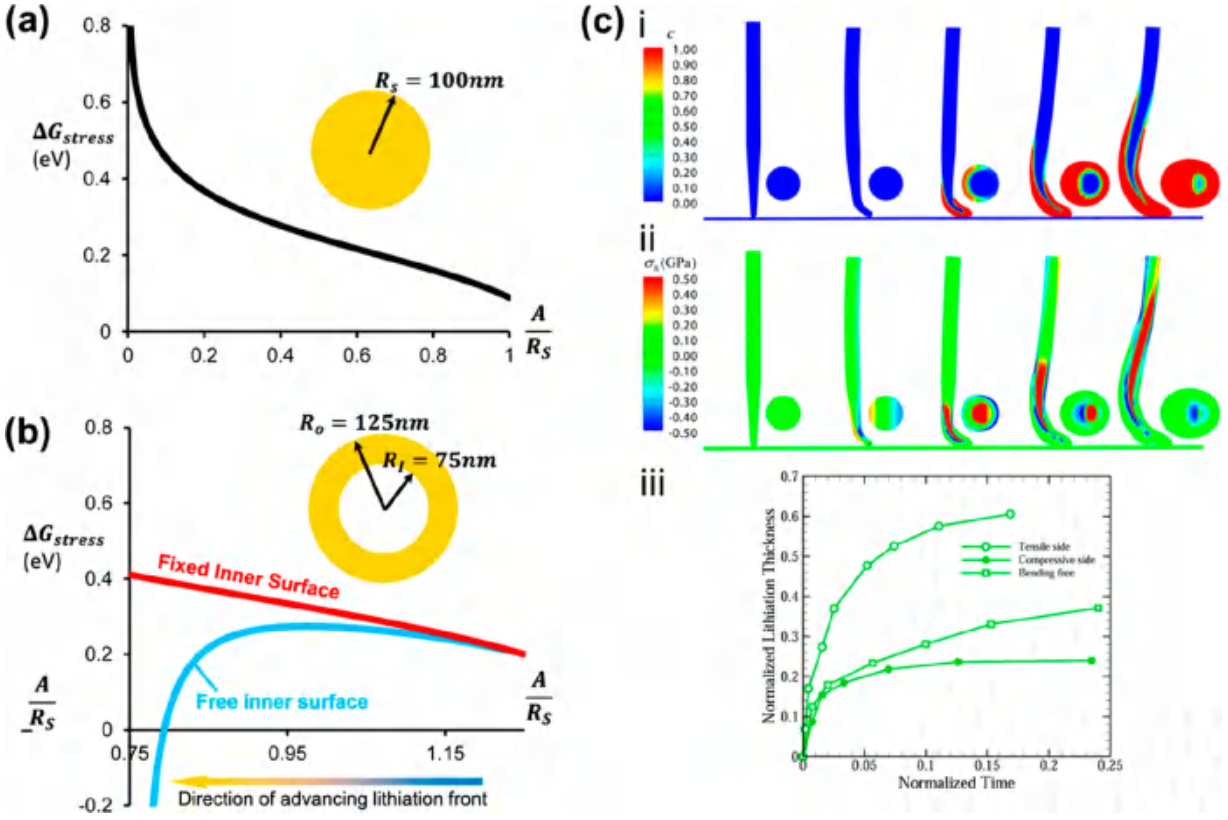

Figure 8. (a,b) Stress-modulated driving force for lithiation as a function of the lithiation front position A/R_S for (a) solid and (b) hollow silicon nanowires.[94] Reproduced with permission of ref 94. Copyright 2015 Elsevier. (c) (i,ii) Li concentration profiles and corresponding hydrostatic stress concentration profiles at different lithiation stages of a simulated Ge nanowire. (iii) Lithiation kinetics of simulated Ge nanowire. Both the lithiation thickness and time are normalized by the diameter and total time for full lithiation of the Ge nanowire.[96] Reproduced with permission of ref 96. Copyright 2014 American Chemical Society.

interface becomes negligible. For nanoscale crystallites, however, the composition of the phase boundary becomes sensitive to the size and shape of the crystallite, and the two-phase coexistence range is reduced because of the extra energy penalty at the interface, as illustrated in Figure 7b.

Similarly, it was found that the Li-ion solubility in anatase TiO_2 progressively increases with decreasing particle size. However, unlike in $LiFePO_4$, in anatase TiO_2, because of the large phase boundary energy penalty, the formation of single-phase particles is energetically more favorable.[8,72] For particle sizes below 40 nm, the separation into two phases becomes thermodynamically unstable within particles, and instead, a complete single-phase transformation occurs particle by particle. In this case, the dynamics of the Li-ion insertion are purely determined by the outer surface tension of the particle.[17] Figure 7c illustrates the domain size evolution of the Li-poor phase (α-phase) and Li-rich phase (β-phase) for two different particle sizes based on Rietveld refinement of XRD data. For relatively large particles (~130 nm), the domain size of the α-phase decreases upon lithiation with a gradual increase of the domain size of the β-phase. However, for the nanosized particles, the size of the newly formed β-phase during lithiation starts at a value close to the particle size and remains almost constant upon further lithiation. Therefore, as schematically represented in Figure 7d, for the large particle, the β-phase grows at the expense of the α-phase within a particle, whereas the nanosized particle does not allow phase coexistence within a single crystallite. The nanoparticles are transformed particle-by-particle upon lithiation.

2.2.3. Triggering Changes in the Reaction Pathway. The intrinsic lithiation/delithiation mechanism can be altered in nanosized electrode materials, depending on the strain-induced surface energy of reaction phases and the interfacial relationship between the phases. The size-dependent reaction mechanism influences the chemical and morphological evolution of the electrode materials and can be either beneficial or detrimental to the long-term cycle stability of the electrode. Marschilok et al. reported the particle size effects on the reaction mechanism by comparing the lithiation path of two Fe_3O_4 nanoparticles of different sizes. A large Fe_3O_4 crystal is more likely to undergo a nonhomogeneous lithiation by immediately triggering the conversion reaction to Fe metal from the surface of the crystal while lithium insertion is occurring. However, smaller Fe_3O_4 particles first allow lithium ions to intercalate into the Fe_3O_4 crystal structure, followed by the conversion reaction. At full lithiation, a small Fe_3O_4 particle forms a smaller Fe domain than that generated from a large Fe_3O_4 particle. In addition, the formation of smaller Fe domains produces a homogeneous FeO-like structure upon delithiation and thus improves the reversibility of the electrode.[91]

Some transition metal chalcogenide materials, such as $NbSe_3$, also exhibit size-dependent reaction mechanisms; ~45 nm $NbSe_3$ nanoribbons undergo a complete conversion reaction, while ~300 nm $NbSe_3$ nanoribbons undergo the intercalation reaction with limited conversion reaction occurring only at the surface. The surface-limited conversion reaction is due to the large mechanical confinement during the

DOI: 10.1021/acs.chemrev.9b00405
Chem. Rev. XXXX, XXX, XXX−XXX

intercalation-to-conversion transition. However, unlike the case of Fe_3O_4, nanosizing is detrimental to the electrochemical performance of $NbSe_3$ as it makes its reaction irreversible.[92]

2.3. Mechanical Coupling with Electrochemical Properties from Nanosizing

The mechanical stress in electrode materials can affect the thermodynamics and kinetics of the ionic transport, interfacial reactions, and phase changes. The effects become intensified and more adjustable upon nanosizing as nanostructures are openly exposed to electrochemical stimuli and prone to changes in their physicochemical properties with the application of mechanical stresses. In the previous section, it was shown how the surface energy of nanostructures becomes significant in determining the total Gibbs free energy of electrode systems from a thermodynamics viewpoint. Here, we elaborate on the intimate coupling of stress with electrochemical processes and discuss how it could be taken into account to achieve improved structural stability and electrochemistry for nanostructures.

2.3.1. The Role of Stress in Reaction Dynamics of Nanomaterials. Surface stress is a critical factor that influences the lithiation dynamics of nanomaterials by altering the chemical potential of Li. The mechanical stress can either be self-imposed on the system or applied by forming a heterointerface with the substrate. Self-induced stress can be present in nanostructured materials when the lithiation or delithiation of the electrode involves an appreciable volume change and mechanical deformation in the lattice during phase transformation. A geometrical change or mechanical bending of an electrode alters the lithiation-induced stress, changing either the direction or strength of its reaction driving force. Such an effect is most notable in alloying reaction systems such as Si.[93] Both slowing and halting of a reaction front have been observed microscopically in many alloying-reaction systems and were attributed to the limited lithiation driving force owing to the negative contribution of lithiation-induced stress. According to Li et al., the reaction driving force can be modulated with lithiation-induced stress in certain nanostructures, such as hollow Si nanostructures, by varying the ratio between its inner and outer radii.[94] The authors claimed that, unlike for solid nanostructures, where the reaction-induced stress always increases throughout the lithiation process, hollow nanostructures exhibit a distinct stress profile. The initially rising positive stress decreases gradually toward negative stress during the later stage of lithiation, promoting the advance of the reaction toward full lithiation (Figure 8a,b). This study also demonstrated that hollow nanostructures with larger inner radii resulted in less stress-induced resistance to lithiation and hence expedited the lithiation process.

Lithiation-induced stress can also alter the direction of the reaction driving force. Depending on the direction of the stress, the lithiation kinetics can either be promoted or impeded according to the following relation:[95]

$$D_{\text{eff}} = D_{\text{sf}}(c)\exp\frac{\sigma_h \Omega}{k_B T} \tag{8}$$

where D_{eff} is the Li diffusivity in the lithiated region, $D_{\text{sf}}(c)$ is the Li diffusivity under stress-free conditions as a function of the Li concentration, σ_h is the hydrostatic stress, Ω is the activation volume of Li diffusion, and $k_B T$ is the thermal energy. For an alloying system with large volume expansion, it was found that mechanical stress plays an important role in regulating the lithiation dynamics and directions. Wang et al. studied the effect of mechanical bending of a Ge nanowire and observed the symmetry breaking of the lithiation front (Figure 8c).[96] According to the study, a 2−3-fold difference in the lithiation thickness was possible between the tensile and compressive sides of the nanowire. Similarly, Gao et al. found that the lithiation thickness difference can vary with the degree of bending of Si nanowires.[97] It was demonstrated that increasing the bending angle of a Si nanowire results in a larger difference in its lithiation thickness, while the maximum difference of a Si nanowire is smaller than that of a Ge nanowire.

Stress can be also applied by having the active material forming heteroepitaxy with a structurally similar conductive matrix, which sometimes results in a notable change in the intrinsic properties of the active material. Kim et al. reported an epitaxial synthesis of a rutile-VO_2 system that is known to exhibit low lithium activity on a conductive Sb:SnO_2 current collector.[98] The authors observed that the epitaxial stress between the two materials induced preferential growth of VO_2 along the c-axis with high exposure of the reactive (002) surfaces, leading to both high reversible capacity and rate capability. Similar work was performed on a V_2O_5 anode by Pint et al. by depositing it on a NiTi alloy current collector.[99] Regulating both the c and $a-b$ strains induced reversible transformation among phases and altered both the interaction energy and diffusion coefficient of Li ions.

2.3.2. Structural Accommodation of Volume Change by Nanosizing. Insertion of lithium ions into an electrode often involves phase transformation, which is sometimes accompanied by a large volume change. Electrode materials that transform into phases with low elastic moduli upon ion insertion are prone to fracture. In this context, strain accommodation is important, especially for battery anodes undergoing conversion and alloying reactions because their transformed phases easily undergo volume expansion of more than 150%, leading to cycle instability. For example, amorphous Li_xSi with an elastic modulus of 12 GPa has a fracture toughness that is an order of magnitude lower than that of crystalline Si with an elastic modulus of 185 GPa,[100,101] accompanying a volume expansion greater than 300%.

One of the approaches that can enhance the intrinsic tolerance to fracture of an electrode upon lithium insertion is to reduce its size and regulate the shape at the nanoscale. In particular, the size reduction enables a facile strain relaxation along with fast lithium transport. Upon reducing the size to a critical value (L_C), the increase in the surface energy that is accompanied by the potential fracture of a particle exceeds the energy gain of the strain release from the fracture, thus can effectively prevent the fracture:[102]

$$L_C = \frac{\gamma}{Z_{\max} E \varepsilon_m^2} \tag{9}$$

Here, L_C is the critical particle size upon fracture, γ is the fracture energy of the particle, $Z_{\max}$ is the maximum energy release rate, E is the Young's modulus, and ε_m is the mismatch strain. Huang et al. investigated surface cracking and fracture of large Si particles upon electrochemical lithiation and observed that the critical size of Si nanoparticles for lithiation fracture is ∼150 nm from transmission electron microscopy (TEM) studies.[103] They found that the electrochemical lithiation of small nanoparticles near the critical size do not show fracturing from sequential TEM images (Figure 9a−e). On the other

DOI: 10.1021/acs.chemrev.9b00405
Chem. Rev. XXXX, XXX, XXX−XXX

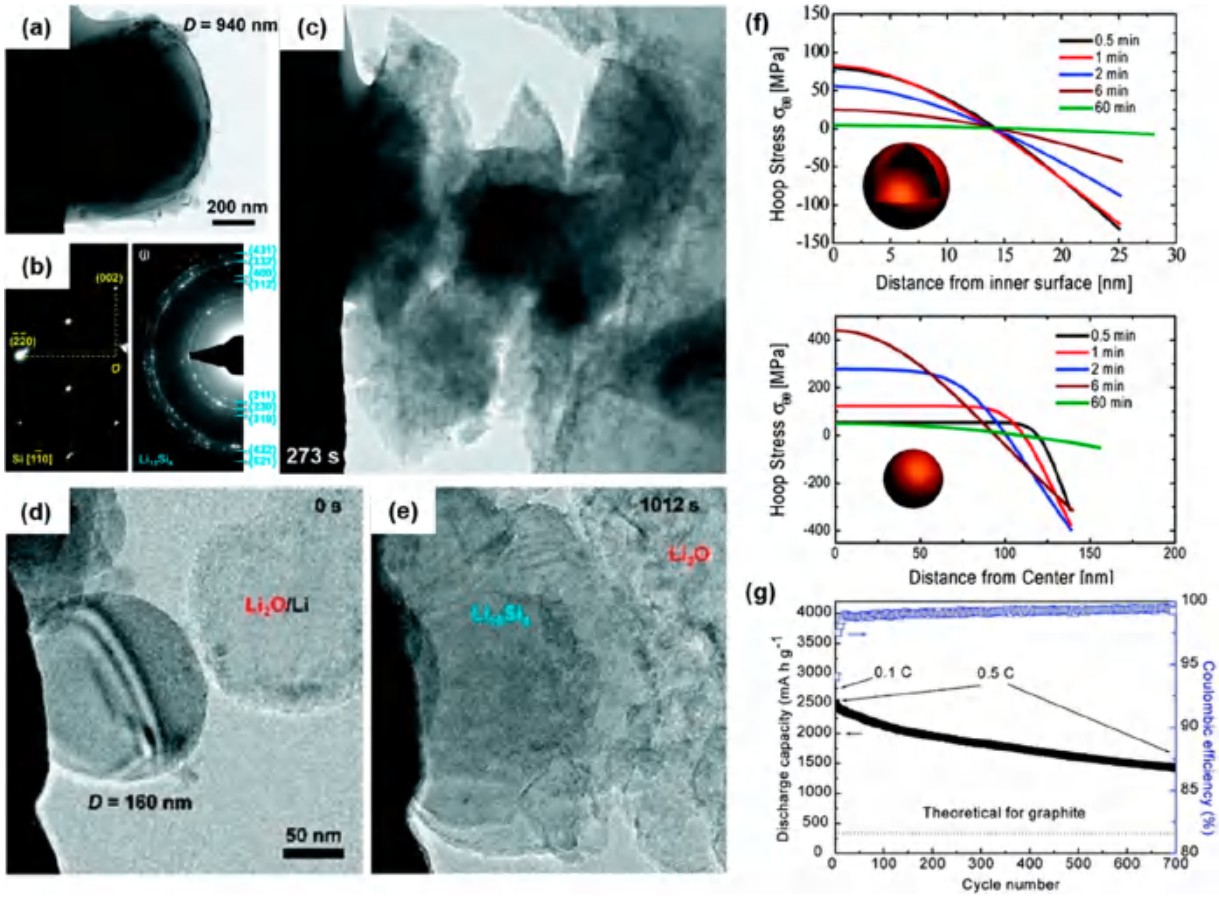

Figure 9. (a,c) Sequential TEM images showing surface cracking and fracture of a large Si nanoparticle upon electrochemical lithiation and (b) corresponding SAED pattern showing the phase transformation from single-crystalline Si to polycrystalline $Li_{15}Si_4$. (d,e) Sequential TEM images of electrochemical lithiation of a small nanoparticle near the critical size showing no fracture.[103] Reproduced with permission of ref 103. Copyright 2012 American Chemical Society. (f) Theoretical calculation showing hoop stress evolution of a hollow and solid Si nanoparticle at a lithiation rate of C/10 for different durations of lithiation, with positive and negative stresses representing tensile and compressive stresses, respectively. (g) Cycle retention characteristics of a hollow Si nanoparticle.[106] Reproduced with permission of ref 106. Copyright 2011 American Chemical Society.

hand, Nix et al. investigated the critical size of Si nanowires by TEM in conjunction with numerical calculations using the continuous phase model and reported that the critical size is ~300 nm for Si nanowires.[104] Some intercalation electrodes also showed size-dependent fracture behavior even though they are not as sensitive as those of alloying- or conversion-reaction electrodes. Zhao et al. applied the numerical model on a $LiCoO_2$ particle and reported that its critical size is slightly less than 300 nm.[102] This conclusion is consistent with the results obtained from electrochemical cycling by Chiang et al., which showed the presence of microcracks in 300−500 nm $LiCoO_2$ nanoparticles cycled 50 times.[105] It was shown that $LiCoO_2$ particles smaller than the critical size were much more robust toward fracture than larger particles.

The shape of the electrode particle has been also revealed to influence its tolerance toward structural fracturing. According to a study performed by Cui et al., hollow Si nanospheres exhibited better fracture endurance than solid spheres with similar sizes because the maximum tensile stress of a hollow nanosphere is ~5 times lower than that of a solid sphere with an equal volume of Si.[106] From theoretical calculations on hoop stress evolution, it was shown that a hollow Si nanoparticle was more effective in tolerating the stress of lithiation than that of a solid nanoparticle (Figure 9f). This improved fracture endurance contributed to the good cyclability of Si electrode, which could deliver a discharge capacity of close to 1500 $mAhg^{-1}$ even after 700 cycles with a Coulombic efficiency close to 99.5% (Figure 9g). Similar results have been reported for other hollow systems, including RuO_2,[107] SnO_2,[108] and Zn_2GeO_4[109] nanoparticles and SiO_2 nanocubes.[110] Sastry et al. analyzed the fracture condition of a $LiMn_2O_4$ particle in relation to its aspect ratio and discharge rate. The authors observed that a particle with an aspect ratio of 1.5 had the highest maximum principal stress of all the particles with different ratios and thus required the lowest discharge rate for crack propagation to occur.[111] The fracture endurance of hollow structures often results in morphological reconstruction of an active anode. Lian et al. reported that hollow Co_3O_4 nanospheres accompany a morphology change to more open mesoporous structures, triggering their electrochemical reactivation after a capacity degradation as their capacity recovers to a higher level than the theoretical value.[112]

In dealing with the mechanical stress and failure of the nanosized electrodes, an additional interesting approach is to modify the surface nature of the nanosized electrode by coating the surface with materials of different lithium diffusivities/reactivities, thus regulating the directions of the volume change in the nanostructure. When the lithium diffusivity of the surface coated material is considerably faster than the core, lithium ions tend to migrate more rapidly along

DOI: 10.1021/acs.chemrev.9b00405
Chem. Rev. XXXX, XXX, XXX−XXX

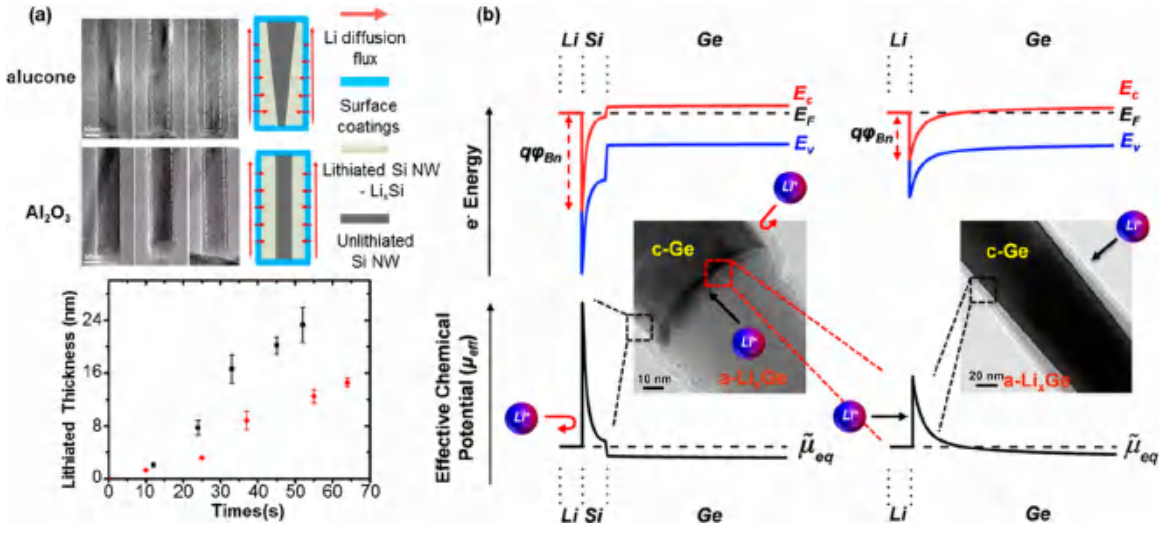

Figure 10. (a) Sequential TEM images showing the different lithiation behaviors of Si nanowires with two different coatings, aluconem, and Al_2O_3 and corresponding plot showing average lithiation thickness vs time for an alucone-coated Si nanowire (black) and an Al_2O_3-coated Si nanowire (red).[113] Reproduced with permission of ref 113. Copyright 2015 American Chemical Society. (b) Band-edge profile and effective Li-ion chemical potential for Si-coated Ge and bare Ge nanowires, showing a negative Schottky barrier height that is larger for the Si-coated Ge than for the Ge-only nanowire. The difference in the chemical potential barrier at the nanowire surface induces a difference in the lithiation dynamics for the two nanowires.[114] Reproduced with permission of ref 114. Copyright 2013 American Chemical Society.

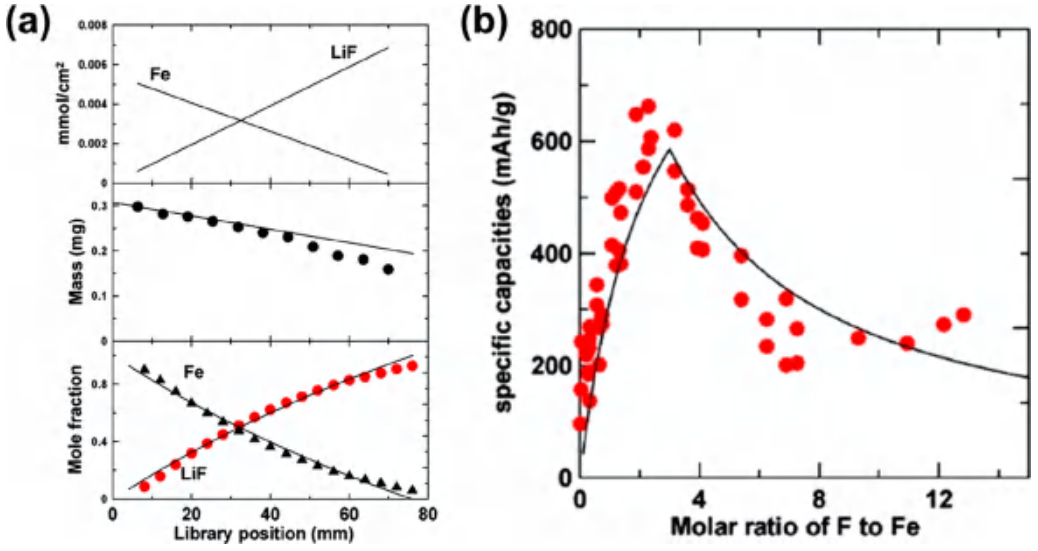

Figure 11. (a) (top) Theoretically predicted composition of LiF and Fe as libraries. Experimentally measured (middle) total mass and (bottom) mole fraction of each component. (b) Theoretical (black line) and experimental (red dots) capacities of $LiF_{1-x}Fe_x$ nanocomposites.[126] Reproduced with permission of ref 126. Copyright 2008 American Chemical Society. .

the surface than through the bulk in the nanostructures, engendering volume expansion along certain directions. Wang et al. compared the uses of alucone and Al_2O_3 for Si nanowire coating, respectively, and demonstrated a difference in the bulk lithiation kinetics of Si for the two cases.[113] The faster surface diffusion of lithium relative to that of the bulk for alucone-coated Si, in comparison to Al_2O_3-coated Si, resulted in a "V-shaped" reaction front rather than an "H-shaped" reaction front (Figure 10a). Another example is a Ge nanowire electrode coated with Si. Dayeh et al. proposed that the use of Si as a coating layer for Ge may allow only axial expansion and volume expansion of Ge (Figure 10b).[114] It was elucidated that as the chemical potential barrier for lithium ion diffusion is higher at the Si/Ge interface than at a bare surface of Ge, lithium ion migration along the surface of a Ge/Si core−shell nanowire is prevented.

3. PART 2: NEW CHEMISTRIES AT THE NANOSCALE: ELECTRODE MATERIAL DESIGN

3.1. Nanocomposite Electrodes

The development of nanomixture electrodes has traditionally focused on enhancing the kinetics of active materials by making composites with conductive agents.[115−117] However, some types of nanocomposite electrodes have provided a way to explore novel electrode chemistries that could not be exploited in the bulk-scale materials. Early research focused on materials that undergo the conversion reaction with lithium, where nanosizing of the materials could significantly improve

DOI: 10.1021/acs.chemrev.9b00405
Chem. Rev. XXXX, XXX, XXX−XXX

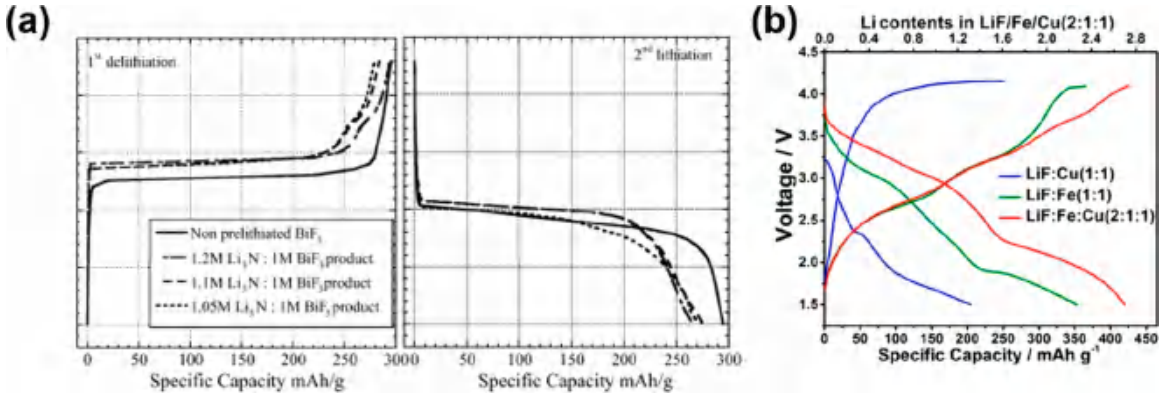

Figure 12. (a) The first charge and discharge profile of non prelithiated BiF_3 and BiF_3 prelithiated with Li_3N.[134] Reproduced with permission of ref 134. Copyright 2011 Elsevier. (b) The charge and discharge profile of LiF/Cu, LiF/Fe, and LiF/Fe/Cu nanocomposites.[135] Reproduced with permission of ref 135. Copyright 2019 American Chemical Society.

the kinetics and reversibility.[118−120] While they could be successfully employed as anode materials, their use in cathodes for lithium ion batteries, especially for those with high redox potentials, required prelithiation by a lithium supplier. In this regard, nanocomposite electrodes comprising lithium compounds and zerovalent metal have been extensively investigated, mimicking the discharged states of the conversion electrodes, so that the electrodes become ready to charge. In recent years, studies on nanocomposite electrodes have been extended to nanocomposites composed of lithium compounds and transition metal compounds with oxidation states higher than 2+. The newly reported nanocomposites showed novel reaction mechanisms distinct from the conventional conversion reaction and could offer higher redox potentials suitable for the cathode, benefiting from the use of oxidized transition metal ions with high redox potentials. In this section, progress in nanocomposite cathodes is summarized with a focus on newly reported nanocomposites.

3.1.1. Nanocomposite Electrodes Mimicking the Discharged States of the Conversion Reaction. For conversion-based electrode materials that exhibit high redox potential and specific capacity but do not contain lithium in their structure,[118,120,121] the prelithiation strategy has been extensively applied for their use as cathodes, physically mimicking the discharged state of conversion materials. This approach has been particularly popular for metal fluorides that have generally shown redox potentials close to ∼3 V (vs. Li/Li^+), and the nanocomposites were generally composed of zerovalent metal and LiF. Among conversion-type materials, iron fluorides (FeF_2 and FeF_3) have received significant attention because of their low cost, high capacity, and high voltage.[80,82,122−124] When lithiated, FeF_2 undergoes a conversion reaction, resulting in the formation of a LiF/Fe composite. Likewise, FeF_3 undergoes an insertion reaction followed by a conversion reaction similar to that for FeF_2. In both cases, the discharge product is a LiF/Fe nanocomposite in which Fe nanoparticles 2−5 nm in size are embedded in a LiF matrix.[80,125] In 2008, Liao et al. prepared $(LiF)_{1-x}/Fe_x$ nanocomposites with x varying from 0 to 1 by cosputtering of LiF and Fe[126] (Figure 11a). The authors tested the electrochemical activity of each composition after the initial charge, and the highest discharge capacity (620 mAh g^{-1} at 70 °C) was attained for a LiF:Fe ratio of 3.16, close to the ratio of F to Fe in FeF_3 (Figure 11b) as follows.

$$3LiF + Fe \leftrightarrow FeF_3 + 3Li^+ + 3e^- \quad (10)$$

The low capacity in the LiF-deficient region was attributed to the incomplete reconversion from the LiF/Fe nanocomposite to FeF_3, while the low capacity in the LiF-rich region was ascribed to a highly insulating nature of LiF remaining after FeF_3 formation. Hori et al. also studied the reconversion reaction of a LiF/Fe (LiF:Fe = 1:1) composite thin film prepared using the codeposition method.[127] After charging, the LiF/Fe composite film delivered a capacity of 300 mAh g^{-1} at 25 °C. Even at 25 °C, the discharge capacity almost reached the theoretical capacity. However, for LiF:Fe ratios of 2:1 and 3:1, the cyclability was inferior to that of the 1:1 electrode. The poor cyclability at high LiF:Fe ratios was attributed to the insulating nature of LiF and lack of conductive Fe.

Nanocomposites for this purpose have been also prepared using ball milling.[128] LiF/Fe nanocomposites with a LiF-to-Fe ratio of 3:1 were found to deliver a capacity of 568 mAh g^{-1} at 20 mA/g, which is close to the theoretical capacity of the nanocomposites (600 mAh g^{-1}). Fichtner et al. claimed that the low conductivity issue associated with LiF in the LiF/Fe nanocomposite can be partly overcome by adding V_2O_5 into the composite[129,130] due to the electron and Li-ion conducting nature of V_2O_5. It was found that, with the addition of V_2O_5 to the LiF/Fe (3:1) nanocomposite, the capacity and reversibility of the electrode could be enhanced. In addition, the cyclability was further improved after heat treatment of the $LiF/Fe/V_2O_5$ nanocomposite. The authors accredited the increased cyclability to the release of the strain induced by ball milling during the heat treatment. Nevertheless, $Li_xVO_{2-x}F_x$ and $V[FeV]O_4$ phases were also shown to be formed after ball milling of $LiF/Fe/V_2O_5$, implying that the observed electrochemical activity could have been partly a consequence of the presence of these species.[129]

Various synthetic routes other than ball milling have been employed to improve electrical conductivity while maintaining the LiF/Fe composite. Prakash et al. synthesized a LiF/Fe/C nanocomposite by pyrolysis of a ferrocene/LiF mixture (LiF:Fe = 2.2:1) at 700 °C under Ar flow.[131] A homogeneous LiF/Fe/C mixture was obtained from the formation of Fe and C resulting from the decomposition of ferrocene. The LiF/Fe/C mixture delivered a relatively low capacity of 230 mAh g^{-1} at 20.8 mA/g because of the low LiF content. Zhang et al. applied similar strategies to fabricate LiF/Fe/C nanofibers by heat

DOI: 10.1021/acs.chemrev.9b00405
Chem. Rev. XXXX, XXX, XXX−XXX

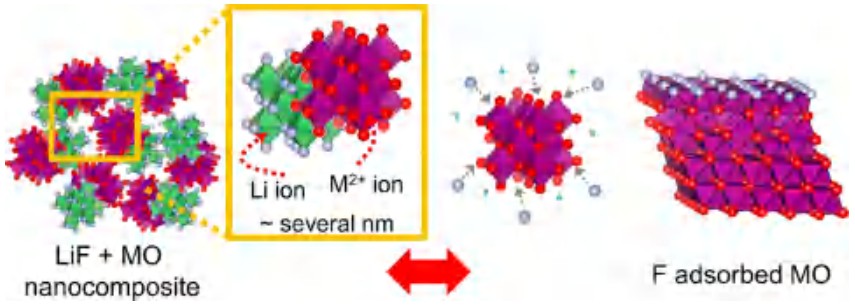

Figure 13. Schematic illustration of the surface conversion reaction.

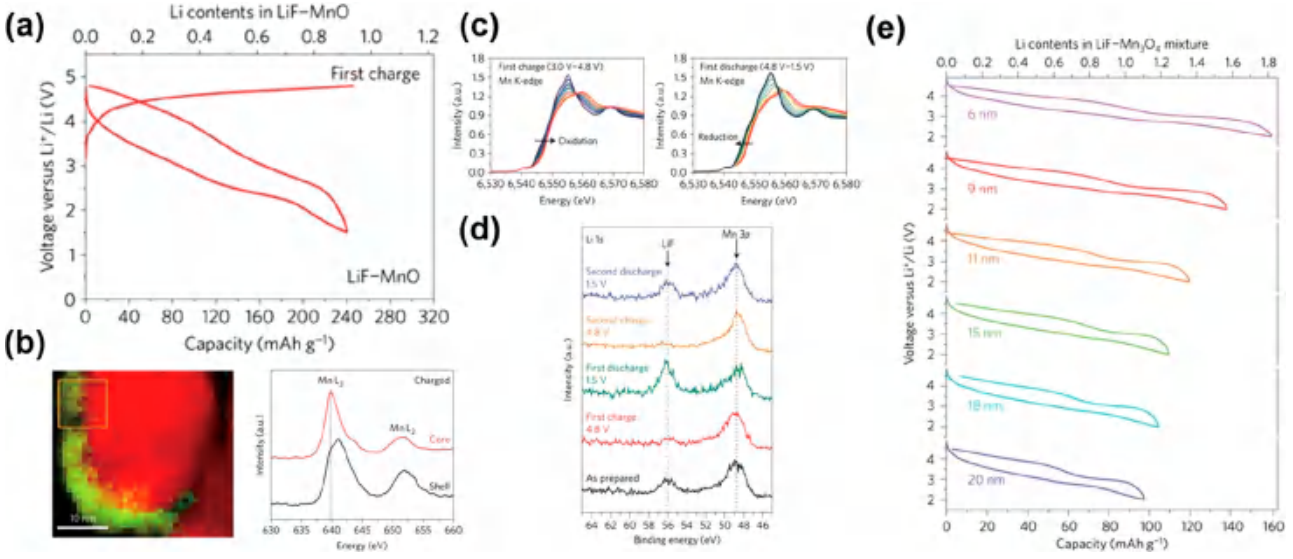

Figure 14. (a) Charge/discharge curves of a LiF-MnO nanocomposite. (b) (left) EELS 2D mapping on fluorine (green) and Mn (red) of a charged particle. (right) Mn L-edge spectra at core (red) and surface (black) region of charged particle. (c) In-situ XANES spectra of the Mn K-edge for the first cycle. (d) Ex-situ XPS spectra of Li 1s region. (e) Electrochemical properties of a LiF-Mn_3O_4 nanocomposite with various Mn_3O_4 particle sizes.[10] Reproduced with permission of ref 10. Copyright 2017 Springer Nature.

treatment of electrospun LiF/ferrocene/polyacrylonitrile (PAN) precursors.[132] Carbon nanofibers were prepared by the decomposition of ferrocene and PAN, and the morphology of the nanofiber was controlled by varying the precursor concentration. The nanofibers prepared from a 21 wt % precursor solution exhibited the best cyclability because of their uniform structure. Ma et al. fabricated LiF/Fe/graphene nanocomposites using a two-step synthesis method.[133] The uniform distribution of LiF and Fe nanoparticles on graphene resulted in a stable cycle life of over 180 cycles. Reports on the varying electrochemical activities of the LiF/Fe/C electrodes imply that not only the composition but also the morphological state of the nanocomposites is critical in determining the performance.

Other transition metal systems, such as those containing Bi and Cu, have also been studied. Amatucci et al. investigated the electrochemical behavior of a Bi/LiF nanocomposite.[134] The Bi/LiF nanocomposite was synthesized by high-energy ball milling of Li_3N and BiF_3. The formation of a metal/LiF nanocomposite through ball milling with Li_3N was also verified with FeF_2, producing a Fe/LiF nanocomposite. The Bi/LiF nanocomposite delivered a discharge capacity of 270 mAh g^{-1} with an average voltage of 3 V vs. Li^+/Li, which is similar to that of BiF_3 (Figure 12a). Zhao et al. studied the dual-metal effect using a Fe/Cu/LiF nanocomposite.[135] The copresence of Fe and Cu in the composite resulted in a high reversible capacity of 400 mAh g^{-1} with an energy efficiency of 76% (Figure 12b). The good reversibility and high energy efficiency of the Fe/Cu/LiF nanocomposite resemble the performance of $Cu_xFe_{1-x}F_2$ ($0 < x < 1$).[136]

Even for electrodes of the same composition, different electrochemical behaviors were observed depending on the morphologies of the electrodes, such as the mixing homogeneity and electron conduction network, which depend on their respective synthesis methods. Unlike electrode materials that undergo an intercalation reaction, where Li-ion and electron transport occur in the same material, the Li-ion and electron transport are separated in nanocomposite electrodes (e.g., Li^+ in LiF and e^- in Fe in a LiF/Fe nanocomposite). Thus, the lithium conductive material can interfere with the flow of electrons and vice versa. Therefore, creating a well-connected electron conduction pathway can have a significant effect on the electrochemical behavior of nanocomposite materials.

3.1.2. Surface Conversion Reactions. A recent discovery of nanocomposite electrochemistry revealed that it can be extended from mimicking the discharged state of the conversion reaction using zerovalent transition metals to new reaction mechanisms exploiting high-valent transition metals in the composites. Recently reported nanocomposite electrodes have exhibited high voltages because of the use of high-valent transition metal compounds and have the potential advantage

DOI: 10.1021/acs.chemrev.9b00405
Chem. Rev. XXXX, XXX, XXX−XXX

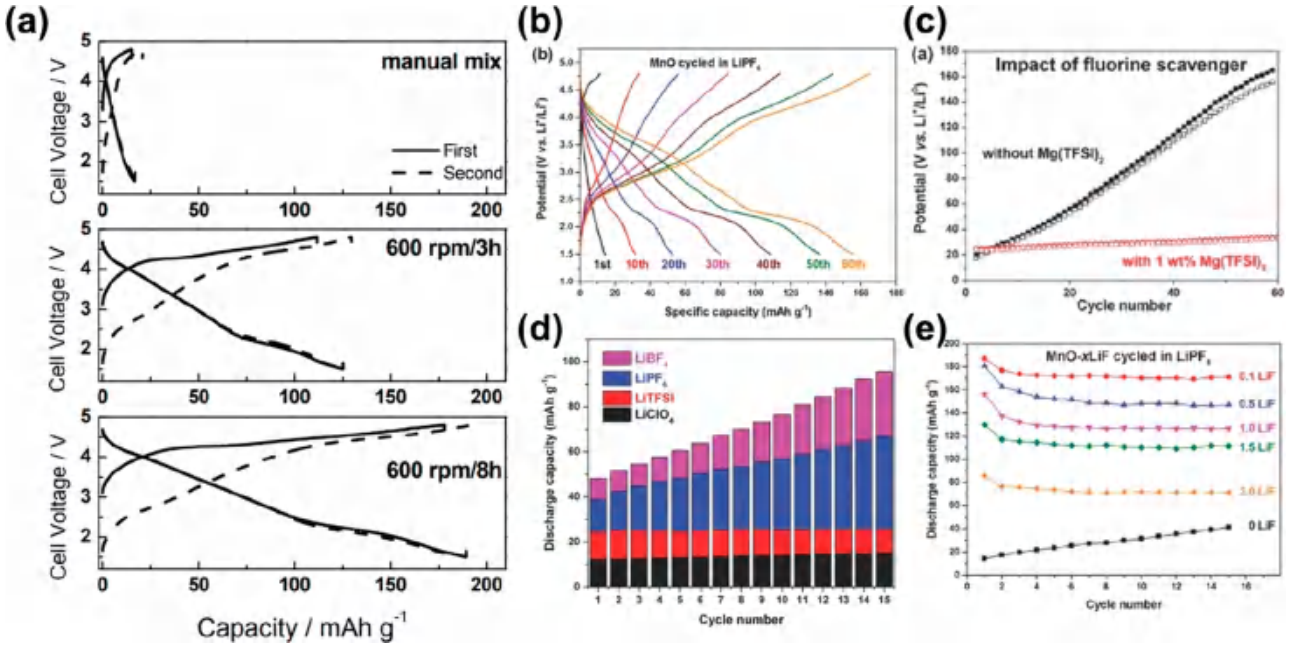

Figure 15. (a) Electrochemical profile of 1.5 LiF−MnO nanocomposites mixed by various methods.[140] Reproduced with permission of ref 140. Copyright 2014 The Electrochemical Society. (b) Electrochemical profile of LiF-free MnO nanocomposite and (c) effect of fluorine scavenger in LiF-free MnO nanocomposite electrodes. (d) LiF-free MnO cycled in various electrolytes. (e) Cyclability of xLiF−MnO (x = 0, 0.1, 0.5, 1.0, 1.5, 2.0) nanocomposite electrodes.[141] Reproduced with permission of ref 141. Copyright 2017 Wiley-VCH Verbg GmbH & Co. KGaA.

of extension to various combinations of lithium and transition-metal compounds beyond their zerovalent states. The "surface-conversion" reaction is one of the recently discovered energy storage mechanisms observed in nanocomposite electrodes (Figure 13).

The surface conversion is a reaction accompanying reversible structural change at the surface of transition-metal compounds that is triggered by anion incorporation, whereas the bulk of the transition-metal compound remains in its pristine state. Jung et al. reported the surface-conversion mechanism in a LiF−MnO nanocomposite.[10] A LiF-MnO nanocomposite with an average particle size of approximately 10 nm was synthesized by high-energy ball milling of LiF and MnO powders as precursors. Although MnO itself does not generally exhibit electrochemical activity in the cathode region (1.5−4.8 V vs Li^+/Li),[137,138] after mixing with LiF, significant electrochemical activity was observed. After charging to 4.8 V vs Li^+/Li, the LiF−MnO nanocomposite delivered a reversible discharge capacity of 240 mAh g^{-1} (0.9 e^-/Mn) with an average voltage of 3.1 V (Figure 14a). X-ray absorption spectroscopy (XAS) and X-ray photoelectron spectroscopy (XPS) analyses revealed that the LiF decomposition and Mn oxidation in MnO occur simultaneously during charging, which is mediated by reversible fluorine absorption/desorption at the MnO surface, as observed in TEM and extended X-ray absorption fine structure (EXAFS) analysis during charge and discharge (Figure 14b−d). In addition, a reversible structural change at the MnO surface during charge/discharge was observed, whereas the bulk region remained as MnO. Because the dominant reaction occurs on the surface, it was expected that the electrochemical activity would depend on the exposed surface area of MnO. Indeed, the discharge capacity increased linearly upon decreasing the size from 20 to 6 nm (Figure 14e). A representative surface-conversion reaction mechanism is described by eq 11.

$$LiF + Mn^{2+}O \leftrightarrow Li^+ + e^- + Mn^{3+}O - F \quad (11)$$

Zhang et al. studied the fluorination process in MnO using various analytical tools, including pair distribution function (PDF) analysis, scanning transmission electron microscopy (STEM), and nuclear magnetic resonance (NMR) spectroscopy.[139] They also observed the formation of Mn−O−F compounds composed of an O-rich core and an F-rich surface after charging. The ^7Li NMR and PDF analyses suggested the presence of a lithiated phase in addition to LiF and MnO on the discharged electrode. Dimov et al. studied the electrochemical properties of LiF−MnO_x (x = 1, 1.33, 1.5, and 2) nanocomposite electrodes, focusing on the effect of changing the milling time of the nanocomposites.[140] Although the LiF−MnO nanocomposite mixed using a mortar exhibited negligible activity, the LiF−MnO nanocomposite obtained using high-energy ball milling delivered a reversible capacity of 190 mAh g^{-1}, which increased with increasing milling time (Figure 15a). This result implies that the uniform mixing of the nanocomposite and the reduction of the particle size are necessary for the electrochemical activity. Electrochemical tests of LiF−MnO_x (x = 1, 1.33, 1.5, and 2) revealed that all four manganese oxides could be activated by LiF decomposition and that better activation by F^- was achieved for a lower oxidation state of Mn. Nevertheless, the LiF−MnF_2 nanocomposite exhibited a negligible capacity. The low charge capacity delivered by the LiF−MnF_2 nanocomposite indicates that the MnF_2 does not promote the decomposition of LiF. The role of LiF was further analyzed in a full cell test with a graphite anode. The Li content in the graphite anode was tracked using ex situ XRD at various states of charge (SoC). The Li content in graphite linearly increased upon increasing the charged amount. These results confirmed that the electrochemical activity in the LiF−MnO_x (x = 1, 1.33, 1.5, and 2) nanocomposite results from the decomposition of LiF during the charging process and that the F^- generated during

DOI: 10.1021/acs.chemrev.9b00405
Chem. Rev. XXXX, XXX, XXX−XXX

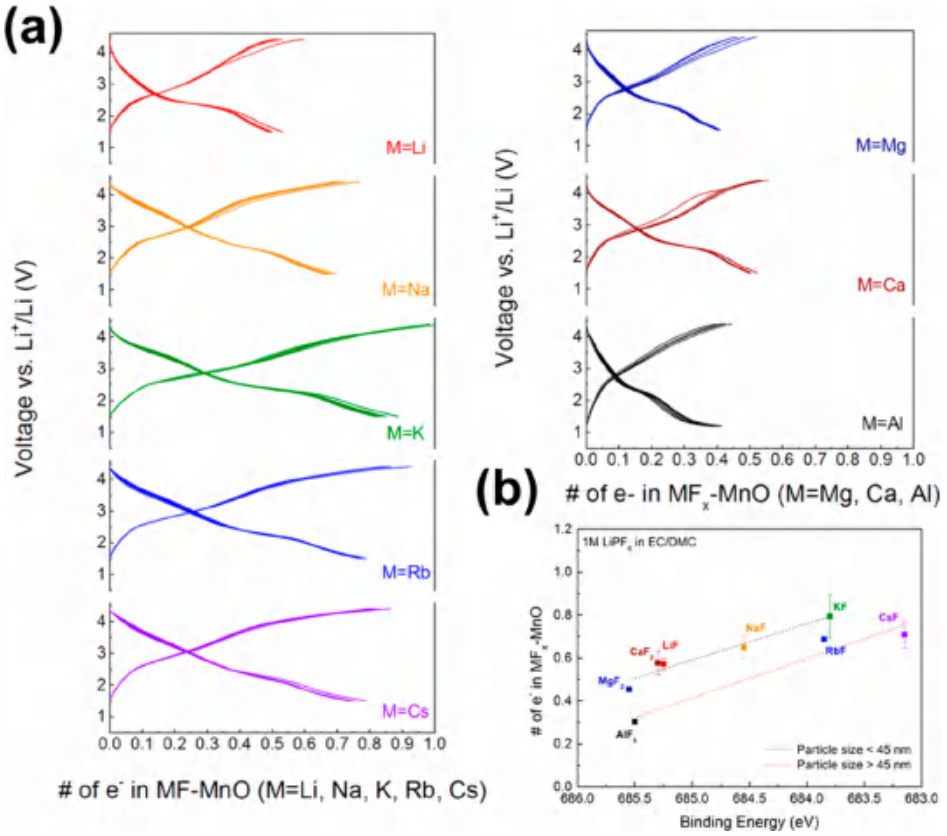

Figure 16. (a) Charge/discharge curves for the first five cycles of eight MFx−MnO (MFx = LiF, NaF, KF, RbF, CsF, CaF_2, MgF_2, AlF_3; F:Mn = 1:1) nanocomposite electrodes tested in a Li hybrid cell. (b) Relationship between the F 1s binding energy and the electrochemical activities of the eight MFx−MnO nanocomposites.[144] Reproduced with permission of ref 144. Copyright 2019 Wiley-VCH Verbg GmbH & Co. KGaA.

LiF decomposition activates the electrodes on the cathode. In addition, the Li^+ from LiF moves to the anode during charging, which supports the notion that LiF−MnO_x (x = 1, 1.33, 1.5, and 2) nanocomposites can act as Li sources.

Zhang et al. reported that not only the LiF but also PF_6^- in the electrolyte could partly supply F^- to MnO in the activation process.[141] The authors showed that LiF-free MnO was activated upon cycling, resulting in a discharge capacity of 14 mAh g^{-1} in the initial cycle and 156 mAh g^{-1} after 60 cycles (Figure 15b). The authors further noted that not only the F^- from LiF decomposition but also the F^- from PF_6 decomposition could activate the MnO during charging. Upon adding 1 wt % $Mg(TFSI)_2$ into the electrolyte as a fluorine scavenger, the activation behavior was not observed (Figure 15c), which suggests that the PF_6^- can activate MnO via F^- donation. The authors also tested the activation behavior by varying the salt component in the electrolyte (Figure 15d). $LiPF_6$ and $LiBF_4$ salts, which are known to release LiF under water-containing or high-temperature conditions,[142] exhibited activation behavior during the cycle, whereas the F-free $LiClO_4$ and relatively stable LiTFSI salts did not exhibit activation behavior during the cycle. The addition of 0.1 LiF to MnO significantly increased the capacity to 175 mAh g^{-1} because of the F^- donation from both LiF and the PF_6^- in the electrolyte (Figure 15e). However, further increasing the LiF content led to a reduction of the capacity, which was attributed to the increase in the total mass and the decrease in the electronic conductivity.

Unlike conventional intercalation materials, for which the charge storage capacities are affected by the alkali ion species, surface-conversion materials are less sensitive to alkali ion species because the reaction relies on the shuttling of F^- near the surface of the transition metal compounds, whereas alkali ions are not inserted into the structure. Zhang et al. studied the Na storage behavior in a MnO-based nanocomposite electrode.[143] Similar to the case of Li, the NaF-free MnO electrode tested in a $NaPF_6$ electrolyte could be activated during successive cycling with the aid of F^- donation from PF_6^- decomposition. When fully activated, the electrode delivered a reversible capacity of 140 mAh g^{-1}. The addition of 0.1 NaF to MnO significantly increased the initial discharge capacity from 12 to 157 mAh g^{-1}, resulting from F^- donation from both NaF and PF_6^- decomposition. The results were similar to those reported in the authors' previous work on xLiF−MnO (0 < x < 2) nanocomposite electrodes.[141] The similar electrochemical results imply that the reaction mechanism of the NaF−MnO nanocomposite resembles that of the LiF−MnO nanocomposite, which is mediated by the F^- reacting at the surface of transition metal compounds, which in turn is independent of the alkali ion.

Jung et al. studied the factors affecting the activity of the nanocomposite electrodes and evaluated the feasibility of exploiting the surface-conversion reaction beyond Li, Na, and K battery systems.[144] They synthesized eight representative nanocomposites ((LiF, NaF, KF, RbF, CsF, 0.5CaF_2, 0.5MgF_2, 0.33AlF_3)−MnO) and tested the electrochemical activity of each in a Li cell (Li metal and 1 M $LiPF_6$ in ethylene carbonate/dimethyl carbonate (EC/DMC) electrolyte). All eight fluoride compounds decomposed to donate F^- to MnO during charging; however, the degree of decomposition varied

DOI: 10.1021/acs.chemrev.9b00405
Chem. Rev. XXXX, XXX, XXX−XXX

(Figure 16a). The series of electrochemical tests revealed that the lattice energy of the fluoride compounds, which was feasibly indicated by the F 1s binding energy, is the key parameter determining the activity of the nanocomposite. Low lattice energies, with F^- weakly bound in fluoride compounds, resulted in easier decomposition; in turn, more fluorine is provided during the charging process, leading to higher capacity (Figure 16b). In addition, the authors successfully tuned the electrochemical activity by adjusting the binding energy through the formation of a solid solution between LiF and CsF. This work not only revealed the thermodynamic origins of the electrochemical activity in the nanocomposite but also suggested that this concept can be expanded to other battery systems such as MgF_2−MnO as a Mg battery cathode material.

Studies on nanocomposites using transition metal compounds other than MnO have also been conducted. One example is the LiF−NiO nanocomposite reported by Tomita et al.[145] A larger first discharge capacity was obtained upon increasing the milling time (116 mAh g^{-1} for the 12 h milled sample and 216 mAh g^{-1} for the 144 h milled sample). However, the authors claimed that the LiF and NiO formed a solid solution when the mixture was ball-milled more than 72 h. Therefore, it is not yet clear whether the electrochemical activity originated from the nanocomposite or intercalation/deintercalation of Li^+ ions into/from the host structure. The same group also reported the electrochemical properties of a $4LiF-NiMn_2O_4$ nanocomposite cathode.[146] Similar to the results of their previous study, the discharge capacity increased from 205 to 256 mAh g^{-1} upon increasing the ball-milling time from 36 to 144 h. However, the composite that was ball-milled for 192 h exhibited a decreased capacity of 213 mAh g^{-1}. Further research is needed to better understand the behavior of LiF−NiO based nanocomposites.

3.1.3. Host Formation Reactions. Another unconventional electrochemical mechanism found in nanocomposite electrodes is the "host-formation" reaction. The initial state of the composite and the charging process are similar to those of the surface conversion reaction, where alkali compounds and transition-metal compounds are mixed on the nanoscale and the charging process involves the dissociation of the alkali compounds. However, it differs in that the transition metal compounds gradually transform into a new intercalation host for the alkali ions, as a result of the chemical reaction between the transition metal compound and the liberated anions from the alkali compounds (Figure 17).

Further reaction occurs via reversible intercalation/deintercalation of the alkali ions into/from the host structure. Kim et al. first reported host-formation behavior in a LiF−FeF_2 nanocomposite.[9] After the first charge, the composite delivered a reversible capacity of 190 mAh g^{-1} (Figure 18a). The composite was also compatible with a graphite anode, which showed that LiF not only activates the FeF_2 via fluorine donation but also acts as a Li source in the cell. It was revealed that the Fe^{2+}/Fe^{3+} redox couple is responsible for the reversible reaction from Fe K-edge XAS analysis. Local structural analysis presented that the FeF_2 transforms into a FeF_3-like structure during charging, which resembles the defective FeF_3. The formation of defective FeF_3 in the LiF−FeF_2 nanocomposite was attributed to the nature of in situ electrochemical synthesis, occurring at room temperature with kinetically slow F^- incorporation into bulk FeF_2. Once the FeF_3-like phase was formed during the charge, further reaction occurred

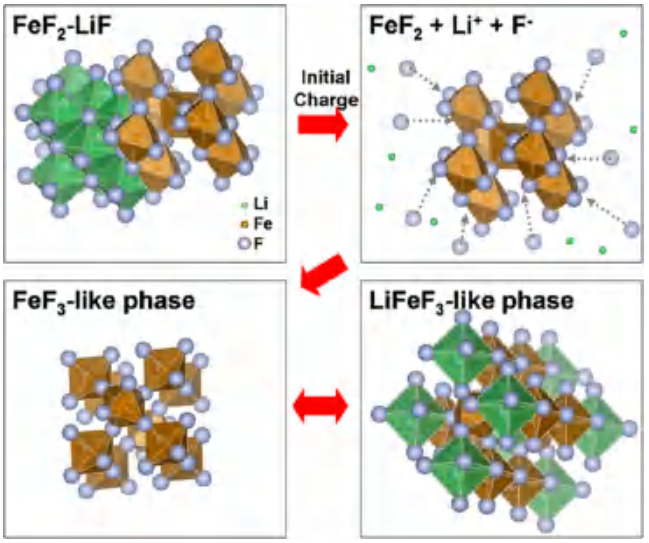

Figure 17. Reaction mechanism of LiF−FeF_2 nanocomposite that undergoes a "host-formation" reaction.[9] Reproduced with permission of ref 9. Copyright 2012 Elsevier.

via Li insertion into the FeF_3-like phase to form a trirutile Li_xFeF_3 phase. The host-formation reaction for the LiF−FeF_2 nanocomposite is described in eq 12.

$$LiF + Fe^{2+}F_2 \rightarrow Li^+ + e^- + Fe^{3+}F_3 \leftrightarrow LiFeF_3 \quad (12)$$

The detailed reaction mechanism of LiF−FeF_2 was recently reported by Tawa et al.[147] The authors synthesized the LiF−FeF_2 nanocomposite using the sol−gel method in an ethanol solution to overcome the shortcomings of the high-energy ball-milling method and to demonstrate the possibility of mass production. EXAFS analysis revealed that the charged phase was defective FeF_3, which is consistent with the report of Kim et al. During discharge, a small polarization was observed in the plateau region, while a relatively large polarization was observed at the end of the discharge, which implied that the reaction mechanism may change at the end of discharge (Figure 18b). The trace of FeF_2 was observed using XRD in the fully discharged state, and the authors concluded that after a certain proportion of Li is inserted into FeF_3 to form Li_xFeF_3, additional lithiation leads to a surface conversion reaction to form the LiF−FeF_2 nanocomposite. The reformation of LiF−FeF_2 at the end of discharge also resulted in a large voltage hysteresis in the second charge, which is similar to the first charge profile (Figure 18b).

The formation of a FeF_3-like phase during cell operation was also reported by Hwang et al. for a NaF−FeF_2 nanocomposite cathode for a Na-ion battery.[148] During the charge, NaF was decomposed, and the liberated F^- was incorporated into FeF_2, which triggered the transformation into FeF_3. It was demonstrated that the Fe K-edge was reversibly shifted during charge and discharge, indicating that the Fe^{2+}/Fe^{3+} redox couple is active in this system. The detailed mechanism of host formation involving Na was analyzed by applying two different cutoff voltages (4.5 and 4.8 V vs Na^+/Na). Upon increasing the charge cutoff voltage from 4.5 to 4.8 V, the discharge capacity increased with a greater fraction of the host structure being formed. The EXAFS fitting for the charged phase also indicated that the portion of FeF_3 increased with increasing cutoff voltage. It was found that the transformation from FeF_2 to FeF_3 did not occur homogeneously throughout the particle

DOI: 10.1021/acs.chemrev.9b00405
Chem. Rev. XXXX, XXX, XXX−XXX

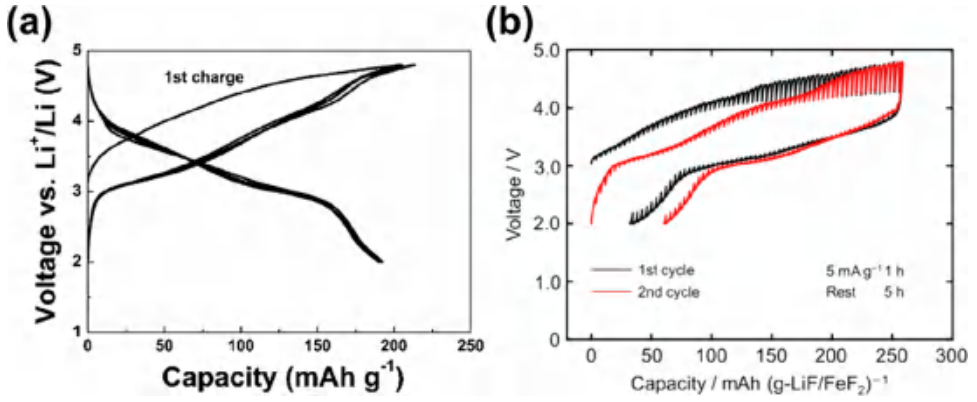

Figure 18. (a) Charge/discharge curve of LiF−FeF_2 nanocomposite.[9] Reproduced with permission of ref 9. Copyright 2012 Elsevier. (b) GITT measurements for the first two cycles.[147] Reproduced with permission of ref 147. Copyright 2019 Elsevier.

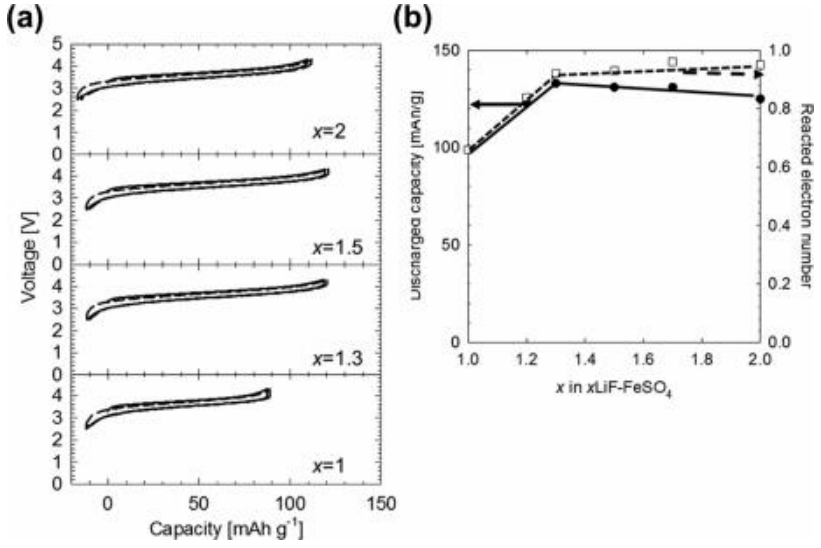

Figure 19. (a) Charge/discharge curves of xLiF−$FeSO_4$ nanocomposites and (b) discharge capacity as a function of LiF content.[149] Reproduced with permission of ref 149. Copyright 2018 Elsevier.

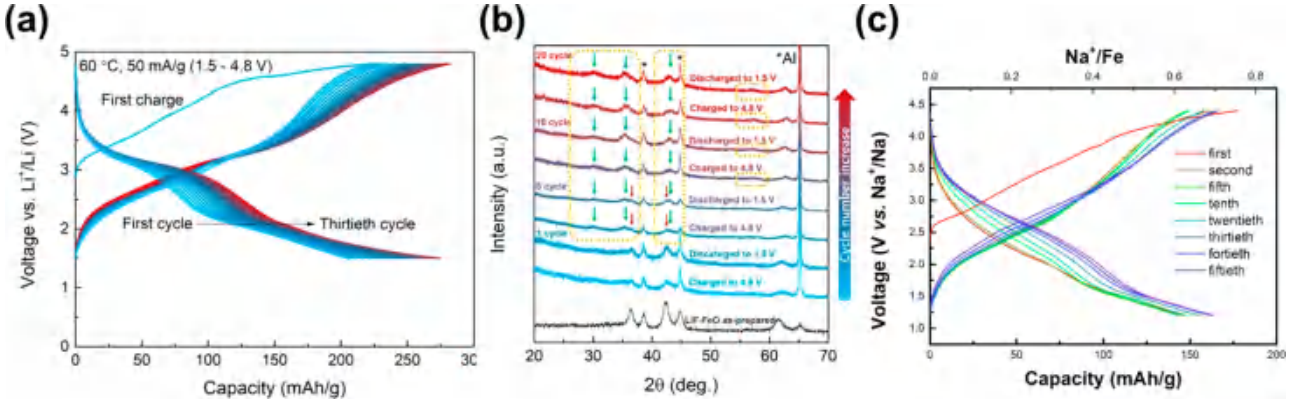

Figure 20. (a) Charge/discharge curves of LiF−FeO nanocomposites and (b) ex situ XRD results for various cycles.[12] Reproduced with permission of ref 12. Copyright 2018 American Chemical Society. (c) Charge/discharge curves of NaF−FeO nanocomposites.[154] Reproduced with permission of ref 154. Copyright 2019 Elsevier.

but instead propagated from the particle surface to the interior of the bulk.

A xLiF−$FeSO_4$ ($1 < x < 2$) nanocomposite was studied by Kitajou et al.[149] The xLiF−$FeSO_4$ nanocomposite was prepared using high-energy ball milling by varying the LiF content between 1 and 2 equiv. Although a sufficient analysis of the charged phase was not provided in the report, xLiF−$FeSO_4$ is suspected to have followed the host-formation reaction given the presence of the $LiFeSO_4F$ host structure[150,151] and the well-defined plateau of the electrochemical profile. The capacity increased to 131 mAh g^{-1} upon increasing x from 1 to 1.3 but decreased upon further

DOI: 10.1021/acs.chemrev.9b00405
Chem. Rev. XXXX, XXX, XXX−XXX

increasing x from 1.3 to 2 (Figure 19). The results indicate that a slight excess of LiF helps to form the host structure; however, too much LiF does not contribute to the host structure and acts as an inactive component.

Host formation behavior was also reported for LiF−FeO nanocomposites by Jung et al.[12] In the LiF−FeO nanocomposite, unlike the LiF−FeF_2 and LiF−$FeSO_4$ nanocomposites, an increase in the capacity (200 mAh g^{-1} in the initial cycle and 272 mAh g^{-1} in the thirtieth cycle) were observed as cycling progressed, along with the change in the charge/discharge curves (Figure 20a). Ex situ XRD analysis revealed that the FeO peak was observed in the initial cycle but was gradually replaced by a new set of peaks corresponding to FeOF with a cubic symmetry with increasing numbers of cycles (Figure 20b). The authors concluded that the charged phase was FeOF, analogous to the cubic Fe_2O_3 structure and, moreover, that the discharge reaction occurs via Li intercalation into the cubic FeOF. These findings are interesting because rutile iron oxyfluoride is already a well-known host structure for Li^+ and Na^+ ions, but the host-formation reaction instead yielded a cubic iron oxyfluoride polymorph.[152,153] The new polymorphic cubic FeOF reported by Jung et al. exhibited higher redox potential, lower voltage hysteresis, and extended structural stability compared with those of rutile FeOF. The gradual formation of the cubic FeOF host structure was confirmed by CV and rate capability tests at the first and twentieth cycles. Both tests showed the characteristics of a surface reaction in the initial cycle and a bulk diffusion reaction in the later cycle, clearly supporting the gradual formation of the cubic FeOF host structure upon cycling.

The formation of cubic FeOF was further reported in a Na battery system by Hwang et al. for NaF−FeO nanocomposites.[154] Similar to the LiF−FeO system, the charge/discharge curve changed as cycling progressed and the capacity increased, reaching a maximum capacity of 165 mAh g^{-1} at later cycles (Figure 20c). Ex situ XRD and HAADF-STEM analyses revealed that cubic FeOF was formed after cycling, similar to the LiF−FeO case. Through a series of F K-edge XAS analyses in both the surface-sensitive total electron yield (TEY) mode and the bulk-sensitive total fluorescence yield (TFY) mode, after various number of cycles, it was observed that the host structure was not entirely formed after the initial charge. Instead, as the capacity increased with cycling, a larger amount of the host structure was formed, with a dominant Na intercalation reaction in the new host structure. Hwang et al. also synthesized a KF−FeO nanocomposite and tested it in a potassium battery system.[154] In contrast to the LiF−FeO and NaF−FeO nanocomposites, the discharge capacity of the KF−FeO nanocomposite did not increase as cycling progressed. This finding implies that the host structure may not be formed in the KF−FeO nanocomposite. Ex situ XRD analysis of the cycled electrode only revealed a trace of cubic FeOF, with most of the peak remaining as FeO, implying a specific dependency on the alkali ion species in determining the formation of the intercalation host.

Beyond fluoride-based alkali compounds, the host-formation reaction has also been reported recently for oxide-based alkali compounds. Kataoka et al. reported the synthesis of a sodium-ion battery cathode material after the initial charge process using Na_2O_2−Mn_3O_4 nanocomposites.[155] After the composite was charged, XRD analysis revealed that a structure resembling λ-MnO_2 was formed, indicating that, during charging, the O species generated by decomposition of Na_2O_2 triggered the transformation of Mn_3O_4 into λ-MnO_2. Once the host structure was formed, it delivered a discharge capacity of 194 mAh g^{-1} with Na intercalation/deintercalation into/from the host structure. The highest capacity in the half-cell configuration was achieved at Na:Mn = 1:1, and the best cyclability in the full-cell configuration with a carbon-based anode was achieved at Na:Mn = 1.5:1.

The nanocomposites formed between alkali-ion compounds and transition-metal compounds can either follow surface-conversion or host-formation reactions upon proper electrochemical activation. In both reactions, the transition-metal redox reactions are triggered by incorporation of anions (F and O) generated by the decomposition of the alkali-ion compounds during the charge process. The surface-conversion reaction is characterized by fast reaction kinetics; however, the particle size should be sufficiently small to ensure high capacity. The host-formation reaction revealed the possibility of in situ formation of the host structure during cell operation. However, the kinetics of host formation may differ for each transition-metal compound, which is attributed to the F^- diffusivity in a specific structure as well as the thermodynamic stability of the host structure. In addition, the results for the KF−FeO nanocomposite indicate that, unlike the surface conversion reaction, the host formation reaction cannot be universally expanded to other MF_x compounds (M = Li, Na, K, etc.) because it involves cation insertion into the host structure; thus, the host structure must be capable of storing cations for it to exhibit electrochemical activity. Nevertheless, this may result in a new polymorphic intercalation host with distinct electrochemical properties, as demonstrated by the discovery of a new cubic FeOF intercalation host. Research on nanocomposites remains in its infancy, and there is great potential for further development in the future.

3.2. Charge Storage at Interfaces

Size reduction of electrode materials gives rise to a significant increase in the surface area or interface in a mixture. Recent studies have shown that charge storage on the surface or at the interface becomes non-negligible in nanoscale electrodes and can significantly contribute to increasing the overall capacity. In this section, we will briefly introduce some recently proposed energy storage mechanisms taking place in the interface region: the job-sharing mechanism, where cation and anion charge storage occur in two different compounds at interfaces, and the pseudocapacitor mechanism, where cation intercalation occurs at the surface of the active material with characteristics of both a capacitor and a battery.

3.2.1. Job-Sharing Mechanism. In conventional intercalation electrodes, lithium ions and electrons are simultaneously stored within a single intercalation host. In layered lithium-transition metal oxides such as $LiCoO_2$, for example, lithium de/intercalates from/into the interstitial sites offered by the crystal, accompanied by electron extraction/insertion at the redox center, which is primarily the transition metal, such as $Co^{3+/4+}$ ions in the crystal. However, some materials can store lithium ions and electrons in two different and separated media and can function as electrodes. Balaya et al. reported that in the mixture Li_2O/Ru, lithium ions are stored in the Li_2O phase, while electrons can be inserted into the Ru phase via the so-called "job-sharing" mechanism.[156] In this mechanism, one substance stores ions and the other substance stores electrons at their shared interface. When an ionic

DOI: 10.1021/acs.chemrev.9b00405
Chem. Rev. XXXX, XXX, XXX−XXX

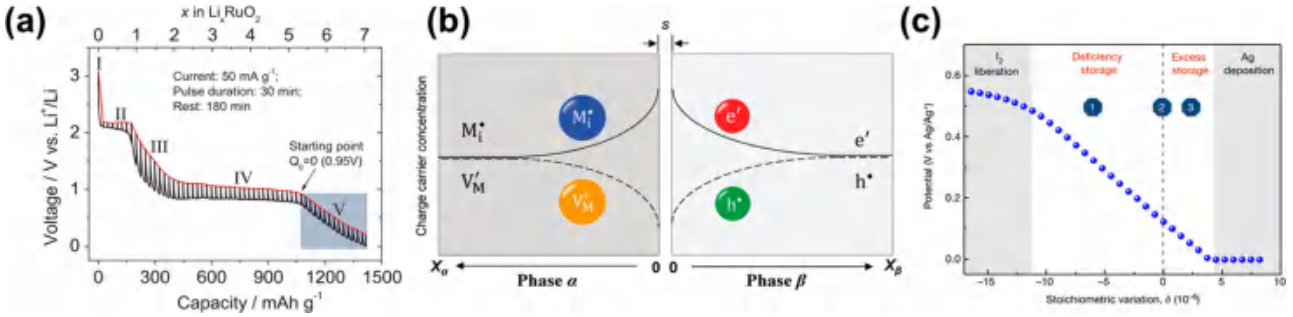

Figure 21. (a) Discharge curve of RuO_2, which consists of five regions.[159] Reproduced with permission of ref 159. Copyright 2013 American Physical Society. (b) Schematic illustrations of a weakly disordered ionic conductor (phase α) and a weakly disordered semiconductor (phase β).[158] Reproduced with permission of ref 158. Copyright 2017 The Royal Society of Chemistry. (c) Variation of silver content in a $RbAg_4I_5$:graphite (90:10) composite, achieved by coulometric titration.[157] Reproduced with permission of ref 157. Copyright 2016 Springer Nature.

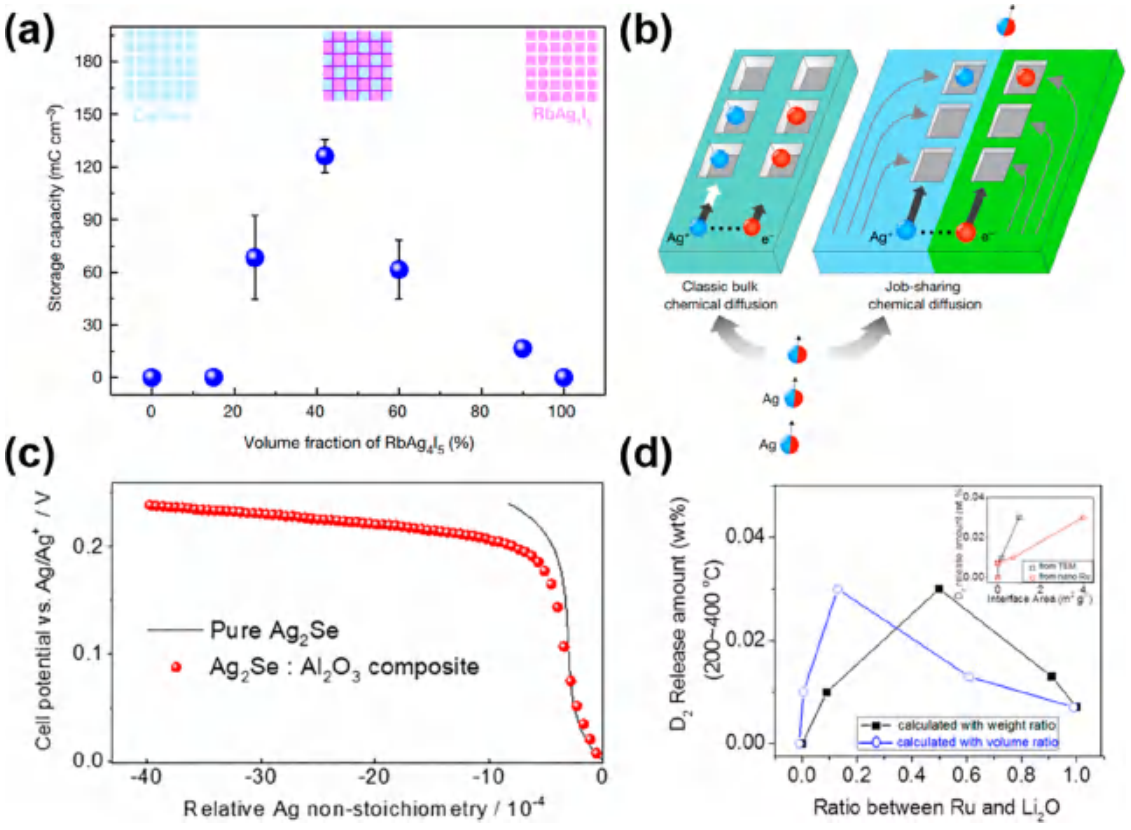

Figure 22. (a) Storage capacity of $RbAg_4I_5$:graphite composite as a function of volume fraction of $RbAg_4I_5$. (b) Schematic of the different chemical diffusion mechanisms (bulk and job sharing).[157] Reproduced with permission of ref 157. Copyright 2016 Springer Nature. (c) Relative Ag nonstoichiometry of pure Ag_2Se and Ag_2Se:Al_2O_3 composite.[162] Reproduced with permission of ref 162. Copyright 2015 American Chemical Society. (d) D_2 desorption amount of Ru, Li_2O and Ru−Li_2O in different ratios (in the temperature range of 200−400 °C).[161] Reproduced with permission of ref 161. Copyright 2018 American Chemical Society.

conductor α phase (e.g., conductor for Li^+ ions) and an electronic conductor β phase are properly mixed to produce heterojunctions at the interface, the interface can serve as a mixed ionic and electronic conductor. In this case, Li^+ can migrate through the space-charge zone of the α phase, whereas e^- can transport through the β phase.[157,158] If these artificial mixed conductors can also allow stoichiometric variations of Li, they can serve as electrochemical hosts of Li^+ ions and thus as electrodes.

For the electrochemical reaction of RuO_2 in a lithium cell in Figure 21a, Balaya et al. proposed that the reaction in region V occurs via the "job-sharing" mechanism and contributes to the additional capacity beyond the theoretical value.[156] According to the authors, the reactions in regions I, II, and III were attributed to lithium intercalation into the RuO_2 host, while the region IV represents the conversion reaction of the host to form a Li_2O/Ru composite. It was proposed that the additional capacity beyond the intercalation and conversion reaction was possible due to the large interface area and the heterojunction between Li_2O and Ru through the job-sharing mechanism.[156] At the heterojunction, the electrons and Li ions were presumed to be stored at Ru and Li_2O, respectively. Fu et al. analytically investigated the relationship between the capacity and the voltage for this mechanism. As illustrated in Figure 21b, two

DOI: 10.1021/acs.chemrev.9b00405
Chem. Rev. XXXX, XXX, XXX−XXX

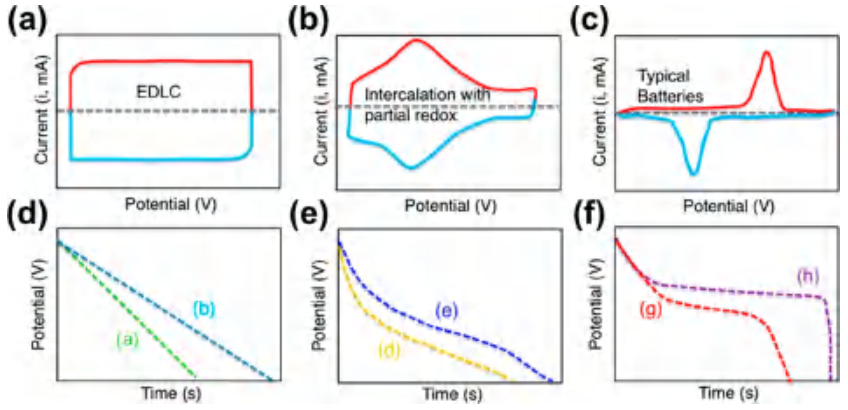

Figure 23. Typical CV profiles of (a) electric double-layer capacitors, (b) intercalation pseudocapacitors, and (c) batteries. Typical discharge profile as a function of time of (d) electric double-layer capacitors, (e) intercalation pseudocapacitors, and (f) batteries.[173] Reproduced with permission of ref 173. Copyright 2018 American Chemical Society.

weakly disordered ionic conductors (α phase) and semiconductors (β phase) were considered. Thereby, it was shown that, when a certain atom M (= $M^+ + e^-$) is stored in the heterojunction, the storage capacity Q and voltage E at each point have the following relationship:[159]

$$\exp\left(-\frac{eE}{k_B T}\right) \propto a_{Li} \propto Q^n \exp(\gamma Q) \tag{13}$$

Here, E is the voltage, k_B is the Boltzmann constant, T is the absolute temperature, e is the electric charge of the electron, a_{Li} is the lithium activity, Q is the electric charge, n is 3 or 4 depending on the assumption, and γ is a constant ($\gamma = \frac{Fs}{\epsilon_{\alpha\beta}\epsilon_0 RT}$), where R is the ideal gas constant, F is the Faradaic constant, $\epsilon_{\alpha\beta}$is the relative permittivity in the charge-free zone, and s is the length of the charge-free zone. In addition to the Li_2O/Ru composite, Li et al. suggested this could be extended to various metal fluorides (TiF_3, VF_3, MnF_2, FeF_2, ...), metal oxides (TiO_2, TiO_2, VO_2, V_2O_3, ...), and TiS_2 and TiN by deep discharging, exploiting the job-sharing mechanism.[160]

The job-sharing mechanism was further applied to the design of conductors transferring other ions such as H and Ag. Chen et al. reported that a $RbAg_4I_5$/graphite nanoscale composite can function as a fast silver-ion conductor.[157] Whereas $RbAg_4I_5$ and graphite are electronically and ionically insulating, respectively, when they are mixed on the nanoscale, the resulting material could function as a mixed conductor. Moreover, with stoichiometric variation of the amount of silver, the materials exhibited the properties of electrode materials. Figure 21c presents an electrochemical profile of a coulometric cell configured as Ag|$RbAg_4I_5$|$RbAg_4I_5$/graphite|Pt. When the Ag was depleted by passing a current through the cell, Ag vacancies and holes were formed in $RbAg_4I_5$ and graphite, respectively. Conversely, when excess Ag was introduced, silver ions were added to the interstitial site of $RbAg_4I_5$, and excess electrons were generated in the graphite. Because this stoichiometric variation is caused by the heterojunction between $RbAg_4I_5$ and graphite, more stoichiometric variation was possible in a larger sample with a higher heterojunction proportion.

As observed in Figure 22a, the $RbAg_4I_5$/graphite composite exhibited maximum capacity at 40 vol % $RbAg_4I_5$ in the composite. Chen et al. observed that stoichiometric variations in this system have fast kinetics and reported a chemical diffusivities 10 times (or more) faster than that of NaCl in water at room temperature i.e.,

$$D^{\delta}_{\text{NaCl-water}} = 1.6 \times 10^{-5}\ \text{cm}^2\ \text{s}^{-1},\ D^{\delta}_{\text{RbAg}_4\text{I}_5} = (50 \pm 20) \times 10^{-5}\ \text{cm}^2\ \text{s}^{-1}$$

These rapid kinetics were explained by the fact that the ions move through the ion path of $RbAg_4I_5$ and the electrons travel through the electron path of graphite, as shown in Figure 22b. For Ag_2Se, which has stoichiometry variation of Ag as a mixed conductor, it has been reported that a greater amount of stoichiometric variation is possible in the presence of Al_2O_3 dispersion than in the pure state,[161] as shown in Figure 22c. The dispersion of Al_2O_3 forms a larger heterojunction than the pure state. There are some possible scenarios regarding how Ag atoms are stored; however, the best fit with theory was that the excess electrons are stored at the surface of Ag_2Se and the silver ions are stored at the surface of Al_2O_3.[161] Fu et al. reported that a Li_2O/Ru nanoscale composite can also store H_2 through the job-sharing mechanism.[162] Similar to lithium storage, H^+ is stored on the surface of Li_2O and e^- is stored on the surface of Ru. As observed in Figure 22d, more heterojunctions could store more H_2, similar to Li storage in the Li_2O/Ru composite. In contrast to conventional mixed conductors that store energy relying on their bulk properties, the job-sharing scheme introduced in this section allows for the discovery of artificial mixed conductors through the generation of heterojunctions between two phases when two or more materials form a composite at the nanoscale.

3.2.2. Pseudocapacitors. Unlike a classical electric double-layer capacitor, which stores charge via a non-Faradaic reaction, a pseudocapacitor undergoes a Faradaic reaction in the energy storage process at the surface or near surface regions. The pseudocapacitor has electrochemical properties that lie between those of electric double-layer capacitors and batteries involving a bulk diffusion reaction. Although pseudocapacitors rely on near-surface reaction and thus generally exhibit lower energy densities (Wh/kg) than conventional batteries, they have received substantial attention because of their high power densities (W/kg). Pseudocapacitors can be roughly classified into intercalation pseudocapacitors and redox pseudocapacitors according to their charge storage mechanism,[163,164] while intercalation pseudocapacitors have been more extensively studied in lithium electrochemical

DOI: 10.1021/acs.chemrev.9b00405
Chem. Rev. XXXX, XXX, XXX−XXX

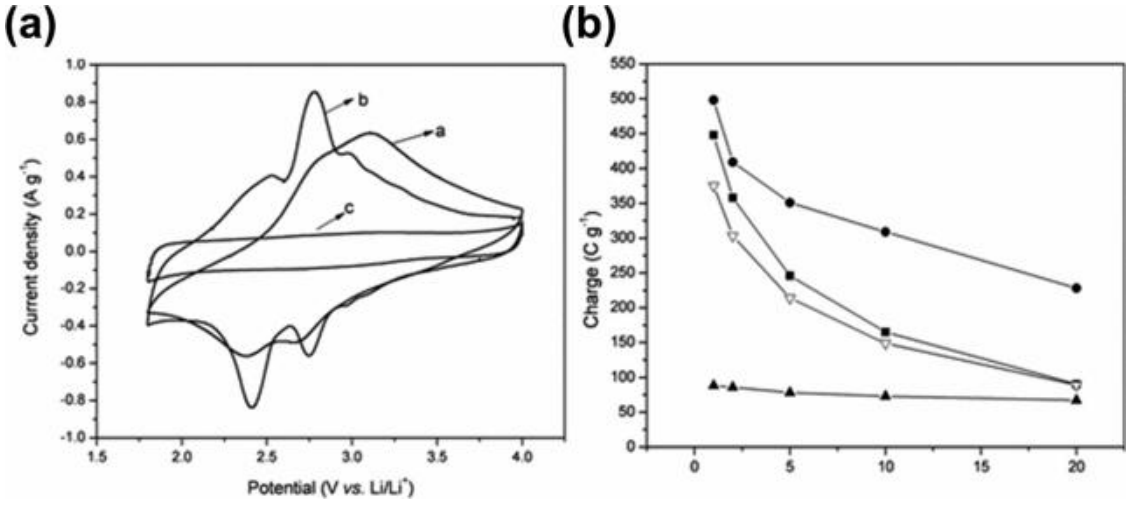

Figure 24. (a) CV profile of V_2O_5 nanowire (a), CNT/V_2O_5 nanocomposite (b), and CNT (c). (b) Rate capability of V_2O_5 nanowires (■), CNT/V_2O_5 nanocomposite (●), CNT (▲), and linear summation of capacity contribution from CNT and V_2O_5 (▽).[169] Reproduced with permission of ref 169. Copyright 2011 Wiley-VCH Verbg GmbH & Co. KGaA.

cells. In redox pseudocapacitors, upon application of an electrical bias, cations (H^+, Li^+, Na^+, ...) are adsorbed on the surface of the transition metal compounds, triggering the redox reaction of the redox centers in the electrode materials. This is often observed in aqueous electrolyte systems involving nanosized transition metal compounds such as RuO_2[165,166] and MnO_2.[167,168] On the other hand, intercalation pseudocapacitors are similar to battery electrodes in that the guest ion is inserted into the structure and the oxidation state of the transition metal is altered (V_2O_5, TiO_2, Nb_2O_5, ...)[26,28,169−172] but differ in that charge is stored only on the electrode surface or near the surface, which results in fast kinetics, thus resembling a capacitor. These surface-driven pseudocapacitors have shown remarkable improvements in energy and power densities with the design and incorporation of various nanomaterials.

Figure 23 illustrates the typical electrochemical profiles presented by intercalation pseudocapacitors in comparison with electric double-layer capacitors and intercalation electrodes.[173] In intercalation electrode materials, a sharp current response at the redox potential in CV curves and a flat voltage response in capacity vs voltage plots are typically observed because of the intercalation process that involves generally similar local structures around the alkali ions (Li^+, Na^+, ...). However, in electric double-layer capacitors, the redox potential is altered in a linear fashion with the concentrations of adsorbed alkali ions, which results in the observed rectangular shape of the CV. On the other hand, intercalation pseudocapacitors exhibit a mixture of these two behaviors, where the alkali ions are inserted into the structure, but they exhibit capacitor-like rectangular CV curves. In nanosized pseudocapacitors, the surface structure can be distorted, and the local structure around the alkali ions may become nonuniform, resulting in a wider distribution of the site energies for alkali ions. The difference in the redox mechanism can also be probed by examining the redox response to varying the CV scan rates. In battery electrode materials that undergo semi-infinite diffusion in the host structure, the peak potential shifts when the scan rate changes. In contrast, because of the fast kinetics of the surface reaction in a capacitor, the peak potential does not notably change with scan rate.[174] A pseudocapacitor exhibits mixed characteristics. The relationship between the current (i, mA) and scan rate (v, mV/s) follows $i = av^{1/2}$ for battery materials[170,175] and $i = bv$ for capacitive materials,[171,176] where a and b are constants. The behavior of a pseudocapacitor can be thus expressed by the combination of the two as given in eq 14.

$$i(V) = k_1 v + k_2 v^{1/2} \tag{14}$$

Here, k_1v and $k_2v^{1/2}$ represent contributions of the surface reaction (capacitor-like) and bulk diffusion (battery-like) reaction, respectively. By determining the k_1 and k_2 values at a specific voltage, each contribution can be quantified.[171,176,177]

Much of the early research on pseudocapacitors was performed in aqueous systems that can exhibit fast kinetic characteristics. However, because to the inherent limitation of the energy density because of water decomposition, more recent works have focused on identifying electrode materials in nonaqueous electrolytes. V_2O_5 is one of the most widely studied pseudocapacitors and is capable of storing not only monovalent ions such as Li^+[178,179] and Na^+[180,181] but also multivalent ions such as Mg^{2+}, Ca^{2+}, Zn^{2+}, Al^{3+}, and Y^{3+}[182−184] through intercalation reactions. Two research groups reported separately that V_2O_5 can store cations through a reaction involving ion diffusion into the bulk structure, but it exhibits capacitor-like properties at the nanoscale.[169,170] The authors introduced carbon nanotubes (CNTs) to address the low electrical conductivity of V_2O_5. Chen et al. fabricated an intertwined CNT/V_2O_5 nanowire using a one-pot hydrothermal process.[169] Using this process, a nanowire containing V_2O_5 particles 20−30 nm in size was formed around the CNT, and the electric conductivity was found to increase approximately 2 orders of magnitude relative to that of a normal V_2O_5 nanowire. In CV experiments at various scan rates (Figure 24), the CNT/V_2O_5 nanocomposite (●) exhibited a higher capacity than the sum of the contributions from the pure CNT and V_2O_5 (▽) at all the evaluated scan rates. Sathiya et al. also studied the electrochemical behavior of a V_2O_5-anchored CNT.[170] From the systematic CV analyses performed at various scan rates, it was demonstrated that the surface reaction contribution increased as the scan rate increased, whereas a larger V_2O_5 loading level resulted in a

DOI: 10.1021/acs.chemrev.9b00405
Chem. Rev. XXXX, XXX, XXX−XXX

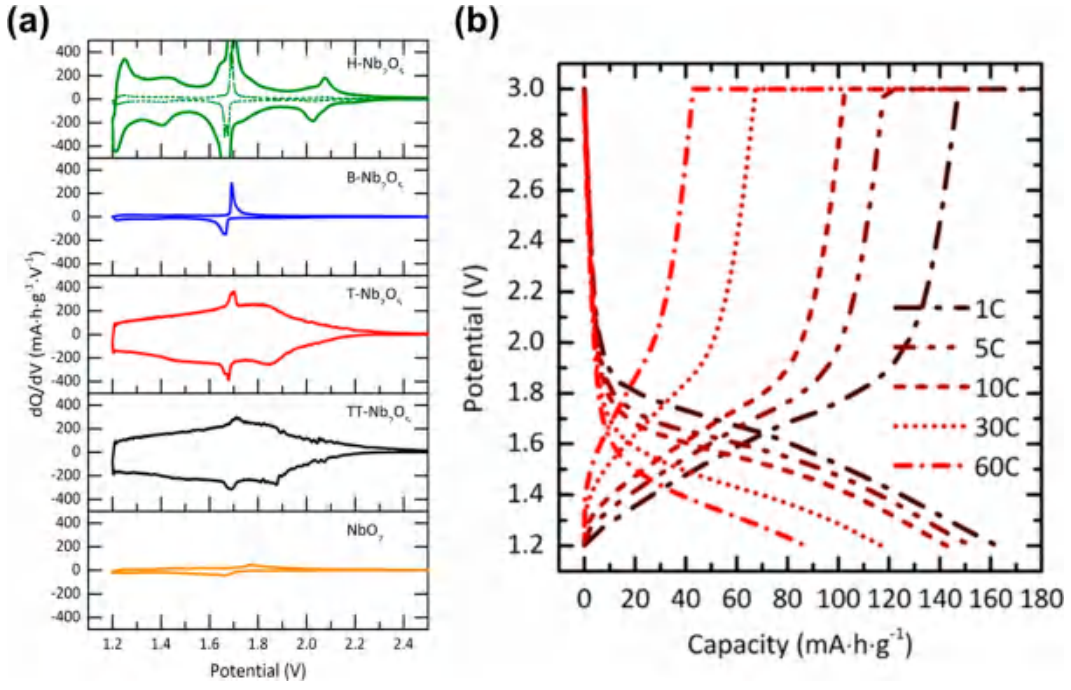

Figure 25. (a) dQ/dV analysis of Nb_2O_5 with various structures. (b) Charge/discharge profiles of T-Nb_2O_5.[172] Reproduced with permission of ref 172. Copyright 2016 American Chemical Society.

smaller total capacity and larger bulk diffusion contribution. These results indicate that the pseudocapacitive characteristic is dominant when the thickness is sufficiently thin (large surface area). According to the XPS analysis, 85% of the V^{5+} was reduced to V^{4+} after discharging to 1.5 V, which is consistent with the determined intercalation capacity. The authors explained that the large capacity resulting from the nondiffusion-controlled reaction originated from vanadium vacancies present at the surface, which trap the Li^+ near vacancies via a non-Faradaic reaction.

Nb_2O_5 is another important example of a material that exhibits battery-like characteristics in the bulk state and capacitor-like characteristics at the nanoscale. Nb_2O_5 forms several metastable phases at room temperature, and the orthorhombic, hexagonal, and monoclinic phases exhibit electrochemical activity based on the intercalation reaction of Li^+ ions at 1.5 V vs Li^+/Li.[185,186] It was shown that the pseudocapacitive properties of mesoporous Nb_2O_5 are based on Li^+ intercalation into the structure by comparatively examining electrolytes based on tetrabutylammonium (TBA^+).[26] A further study on the pseudocapacitive characteristics of Nb_2O_5 revealed that the bulk diffusion is the rate-determining step at high scan rates and that the capacitive term still contributed to the overall capacities, which are typical characteristics of pseudocapacitive materials.[28] In situ XANES analysis at the Nb K-edge also indicated a continuous edge shift during the lithiation process, which confirmed the redox reaction of Nb. Griffith et al. studied the relationship between the crystal structure of Nb_2O_5 and its electrochemical behavior. They synthesized four different polymorphs of Nb_2O_5 by varying the synthesis temperature.[172] The four Nb_2O_5 phases exhibited notably different electrochemical behaviors with regard to capacity, cycle life, and CV curves, as presented in Figure 25a. It was demonstrated that Nb_2O_5 with Pbam symmetry could deliver high rate capability even with micrometer-sized particles, retaining 50% of the low-rate capacity at 60 C (discharge in 1 min) (Figure 25b). The high rate capability was attributed to the low activation energy barrier for Li^+ diffusion (60−100 meV), which was much lower than that of battery electrode materials within the 300−500 meV range.[187,188] It was also speculated that the relatively small structural change accompanying the alkali ion insertion contributes to the fast intercalation pseudocapacitor behavior.

The pseudocapacitive behaviors are only dominant when the electrode materials have a substantially large surface area, thus nanoscale fabrication of the electrode is generally a prerequisite. Benefiting from the intercalation and surface reaction behavior, intercalation pseudocapacitors exhibit higher capacity than other pseudocapacitors and faster reaction kinetics than batteries because they utilize both bulk and surface reactions. However, the gravimetric capacity of intercalation pseudocapacitors remains lower than that of typical battery electrode materials, and an appropriate trade-off between capacity and power is required.

3.3. Metastable Phases in Nanomaterials

As a particle size decreases to the nanoscale, its surface energy simultaneously increases and becomes non-negligible in the overall energy, often stabilizing metastable phases which can potentially lead to unexpected electrochemical properties and performances. According to the Laplace−Young equation, nanosized particles should experience additional, size-induced pressure. Therefore, when the metastable nuclei begin to form, the actual pressure exerted on each nucleus would have an added contribution from the size effect, stabilizing the metastable phases. Recently, the group of Ceder reported on the metastability and synthesizability of crystalline inorganics using the Materials Project Database[189] and argued that metastable phases with low surface energies can be stabilized over the thermodynamically most stable phase with the help of nanosizing during crystal growth. According to the report, a metastable phase that was at one point the lowest free-energy phase during the growth can remain stable even after the

DOI: 10.1021/acs.chemrev.9b00405
Chem. Rev. XXXX, XXX, XXX−XXX

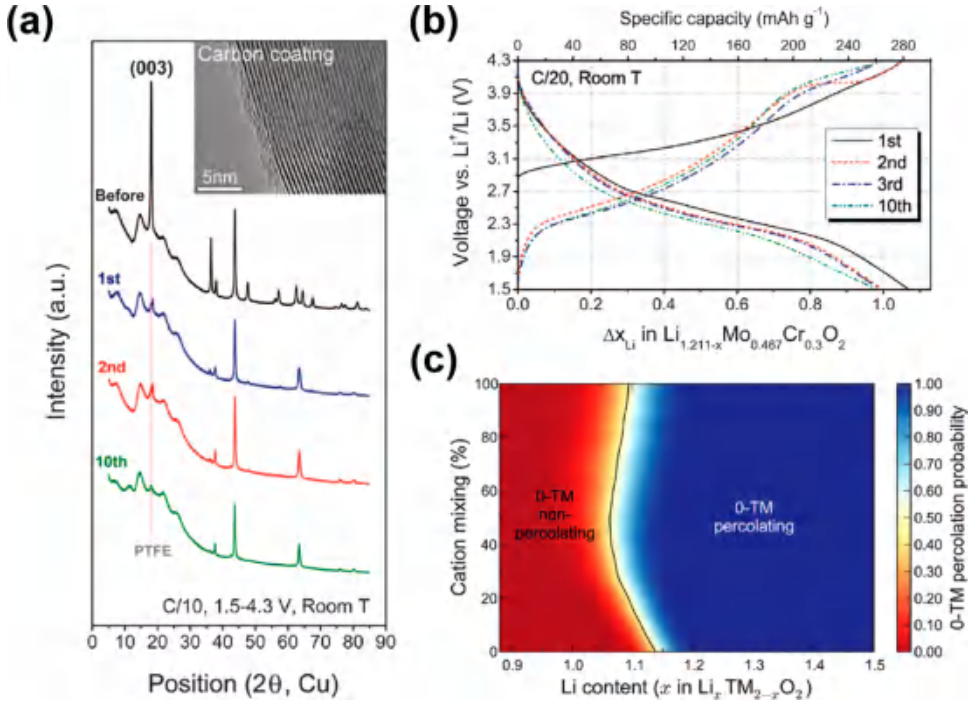

Figure 26. Realization of the metastable disordered rock-salt concept at the nanoscale. (a) XRD patterns of $Li_{1.211}Mo_{0.467}Cr_{0.3}O_2$ before and after 1, 2, and 10 cycles. (b) Electrochemical profiles of $Li_{1.211}Mo_{0.467}Cr_{0.3}O_2$. (c) Computed probability for the percolating network of 0-transition metal channels as a function of lithium content and cation mixing.[13] Reproduced with permission of ref 13. Copyright 2014 American Association for the Advancement of Science.

synthesis. Nonequilibrium thermodynamic reactions can be also exploited in facilitating the design of metastable electrode materials. Although the relationship between the synthetic process and phase diagram has not been completely elucidated, the combined effects of local heating and shear-induced reactions during nonequilibrium reactions (such as high-energy ball-milling) are thought to induce the formation of nanoscale metastable phases.[190−193]

Mechanochemistry has been one of the most frequently adopted methods for the synthesis of metastable phases using the nanosizing strategy.[194] In these methods, a chemical reaction is induced using mechanical energy from a mechanical action such as ball-milling. Mechanochemical synthesis usually offers better contact between the precursors as well as decreased size of the products. Although the fundamentals of mechanochemical reactions remain unclear, they have been used in several fields of materials science to obtain various polymorphs and metastable phases.[195,196] For a Ti−O alloy, mechanical milling enabled the production of three different metastable phases, α-Ti solid solution containing 33 at% O, γ-TiO containing 40−55 at% O, and β-Ti_2O_3 containing 60 at% O, none of which are stable at room temperature according to the phase diagram.[197] This was attributed to the fact that the local pressure and temperature during mechanical ball milling, as well as defects, affect the stability of the various polymorphic phases at room temperature. Recently, as will be discussed in detail below, new battery active materials prepared using mechanochemistry have been reported such as disordered rock-salt phase. For example, a temperature of 1750 °C is theoretically needed to synthesize the $Li_2Mn_{2/3}Nb_{1/3}O_2F$ disordered rock-salt phase, whereas mechanochemical synthesis via high-energy ball milling enables its synthesis at room temperature.[190]

In the context of nonequilibrium thermodynamic synthetic routes and principles, various nanosized metastable phases have been studied as novel chemistries of lithium storage. In particular, the use of disordered rock-salt phases as nanosized materials has been extensively revisited, as the nonequilibrium thermodynamic synthetic routes involving mechanical milling often induce isotropic strain in the powder, thereby producing disordered rock-salt phases easily. The disordered rock-salt phase provides numerous advantages, such as flexibility in the design of electrode materials, as it allows structural incorporation of various multivalent transition metals as redox reservoirs in the rock-salt structures, making them suitable for use as high-energy-density electrode materials. In addition, the isotropic environment of the disordered rock-salt phase results in relatively small lattice parameter changes during cycling.[13] Nevertheless, disordered rock-salt materials have traditionally been considered inappropriate for intercalation-based electrode candidates because of the randomly distributed cations in the structure, which blocks the lithium diffusion channel. However, Lee et al. reported that $Li_{1.211}Mo_{0.467}Cr_{0.3}O_2$ is capable of delivering high capacity and stability even though the material transforms from the layered to the disordered rock-salt structure after several cycles (Figure 26a,b).[13] According to their work, the disordered materials could offer sufficiently fast lithium diffusion when 0-transition metal percolation channels (Figure 26c) are formed by the lithium-excess environment. Since then, there have been several attempts to synthesize the disordered rock-salt phase via a nonequilibrium thermodynamic reaction as a nano phenomenon.[14−16,198,199] Because of the unique characteristics of nanosized disordered rock-salt phases, many groups have conducted research aimed at elucidating the underlying mechanism and developing a definitive process for the synthesis of nanoscale metastable phases for electrodes. In

DOI: 10.1021/acs.chemrev.9b00405
Chem. Rev. XXXX, XXX, XXX−XXX

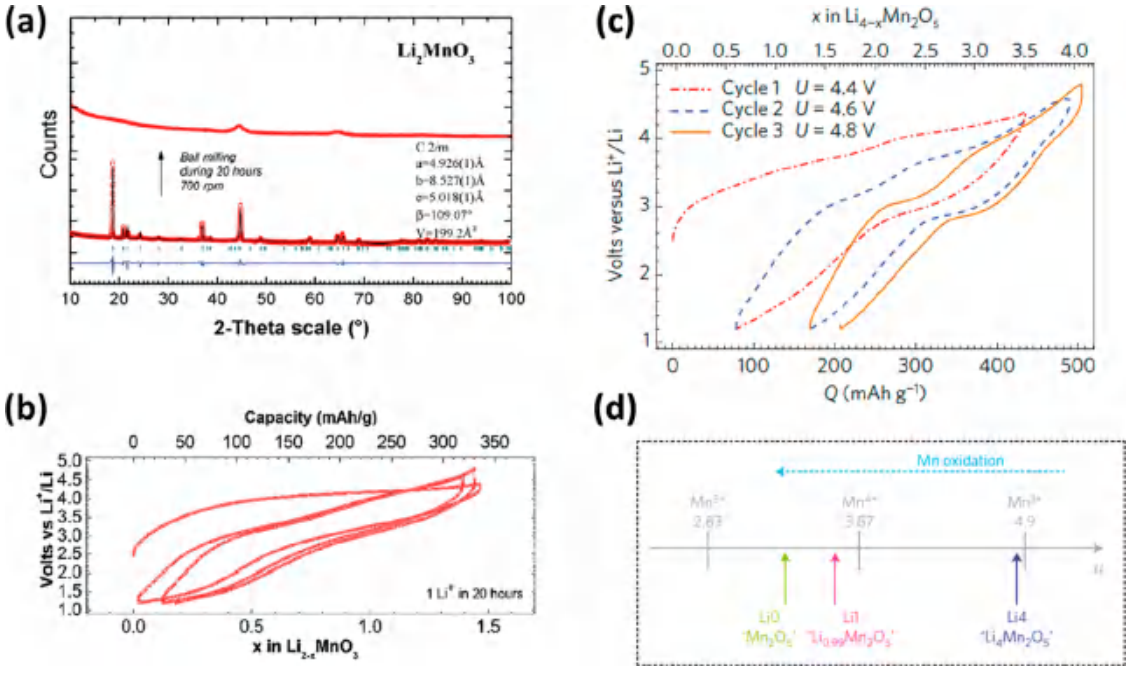

Figure 27. (a) XRD patterns of Li_2MnO_3 before and after a 20 h mechanochemical ball-milling process. (b) Electrochemical profile of a ball-milled nano Li_2MnO_3 material.[198] Reproduced with permission of ref 198. Copyright 2017 The Royal Society of Chemistry. (c) Electrochemical profile of $Li_4Mn_2O_5$ over three cycles with a gradual increase in the cutoff voltage. (d) Comparison of Mn oxidation states by their paramagnetic effective moments for as-prepared and partially and fully oxidized $Li_4Mn_2O_5$ materials.[14] Reproduced with permission of ref 14. Copyright 2015 Springer Nature.

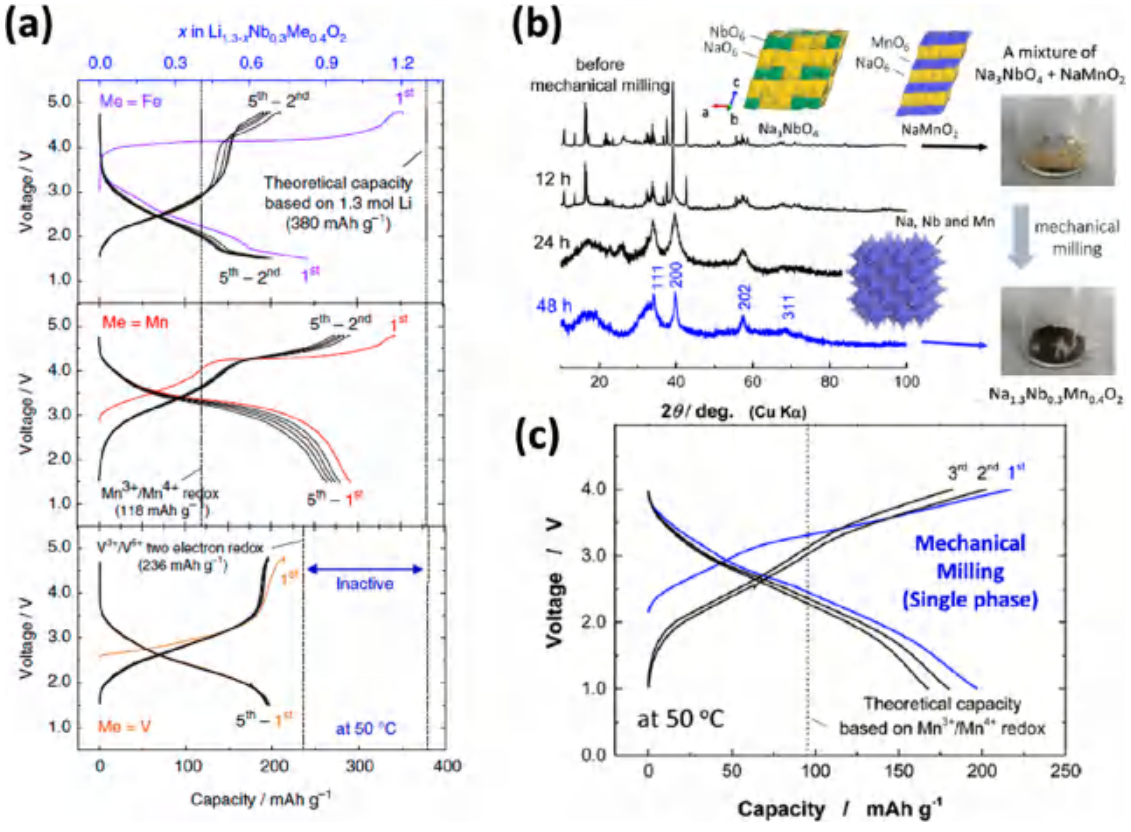

Figure 28. (a) Electrochemical curves of $Li_{1.3}Nb_{0.3}Me_{0.4}O_2$ (Me = Fe^{3+}, Mn^{3+}, and V^{3+}). (b) XRD patterns of $Na_{1.3}Nb_{0.3}Mn_{0.4}O_2$ before and after mechanical milling.[207] (c) Electrochemical properties of $Na_{1.3}Nb_{0.3}Mn_{0.4}O_2$ prepared by mechanical milling.[199] Reproduced with permission of ref 199. Copyright 2017 American Chemical Society.

DOI: 10.1021/acs.chemrev.9b00405
Chem. Rev. XXXX, XXX, XXX−XXX

this section, the current status of research on disordered rock-salt phases is described using two representative material groups, transition metal oxides and transition metal oxyfluorides.

Among the potential candidates, manganese-based rock-salt-type nanostructured materials have been spotlighted because of their low cost, nontoxicity, and the high potential of the Mn^{3+}/Mn^{4+} redox couple. Freire et al. recently showed that a disordered rock-salt Li_2MnO_3 metastable phase could exhibit electrochemical properties distinct from the ordered Li_2MnO_3 phase[198] (Figure 27a,b), simply by transforming an ordered phase to a disordered nanostructure with high-energy grinding. Unlike the ordered structure of Li_2MnO_3, which suffers from a large irreversible capacity originating from cation migration and oxygen gas evolution,[200] the nanoscale metastable Li_2MnO_3 displayed an exceptionally reversible capacity of approximately 290 mAh g^{-1}. In addition, the nanostructured phase could accommodate the strain during the (de)-intercalation process, which is needed for long cyclability of the cathode material. Freire et al. reported a new Li−Mn−O-based metastable nanomaterial, $Li_4Mn_2O_5$, which delivered an impressively high discharge capacity (~355 mAh g^{-1}) as a cathode.[14,201] Mechanochemically synthesized $Li_4Mn_2O_5$ exhibited similar redox active centers (Mn^{3+}/Mn^{4+} and O^{2-}/O^{-}) to other lithium-excess manganese oxides. However, unexpectedly, the disordered $Li_4Mn_2O_5$ nanomaterial displayed a certain proportion of Mn^{4+}/Mn^{5+} redox reactions (Figure 27c,d) in the final stage of the charging process, which was confirmed by performing magnetic susceptibility measurements. This finding was unforeseen because it is known that it is difficult to oxidize Mn^{4+} to Mn^{5+} in octahedral sites. According to density functional theory (DFT) calculations, it was speculated that the oxidation of Mn^{4+} to Mn^{5+} should accompany Mn ion migration from octahedral sites to the adjacent tetrahedral sites.[202] Because of the reversal of the crystal field effects of tetrahedrally coordinated Mn^{4+} d orbitals, the energy to extract electrons from the t_{2g} level was predicted to be reduced. In addition, the migration of lithium ions was claimed to be assisted by oxygen vacancies produced during high-energy ball milling.[203] The anion vacancies cause lithium ions to be predominantly clustered in a pentacoordinate distorted square pyramidal geometry. These unique structural effects allow lithium-ion migration to occur between two square-based pyramidal sites with an intermediate trigonal planar site whose diffusion path differs from the conventional octahedral−tetrahedral−octahedral path.[204] In addition, the three-dimensional lithium-ion diffusion with percolated channels was identified in the distorted oxygen vacant structure by bond valence site energy analysis, which could be implemented in metastable nanoscale phases.

Transition-metal ions that do not have d electrons, such as Ti^{4+}, Nb^{5+}, and Mo^{6+}, promote the formation of the disordered rock-salt phase.[205−210] On the other hand, materials containing d^0 transition metals are generally electrochemically inactive because of their lack of further oxidation and insulating characteristics. Yabuuchi et al. studied d^0-containing lithium-excess disordered materials by substituting several non-d^0 elements (Figure 28a).[205,207] According to their work, the presence of non-d^0 transition metals increases the electrical conductivity and triggers the electrochemical activity of these materials. In addition, specific d electron donor elements such as manganese were found to act as stabilizers of solid-state oxygen redox reactions so that excellent reversibility could be realized for $Li_{1.3}Nb_{0.3}Mn_{0.4}O_2$, undergoing an anionic redox reaction. They also synthesized a composite of these materials with a carbon source using a mechanochemical synthetic process.[199,211] The nanoscale $Na_{1.3}Nb_{0.3}Mn_{0.4}O_2$ materials exhibited a large capacity involving the oxygen redox reaction, whereas the conventionally calcinated $Na_{1.3}Nb_{0.3}Mn_{0.4}O_2$ delivered only cationic redox behavior (Figure 28b,c).

Fluorine incorporation into metastable nanomaterials has received considerable attention as an effective strategy to increase the practical capacity of lithium-excess cathode materials. Lithium-excess materials targeting a high theoretical capacity have been reported to exploit the redox activity of high-valent cations for charge compensation of excess lithium and the additional redox activity of oxygen anions.[212,213] However, the redox capacity of high-valent cations is limited because of their redox inactivity in useful voltage ranges,[205,214−216] and the oxygen redox is known to involve oxygen loss with structural degradation.[212,217,218] Fluorination of lithium-excess materials enables these limitations to be circumvented by modifying the required valence of the metals. The substitution of the lower-valence fluorine for oxygen lowers the corresponding valence of the metal cations,[214,219] thus the redox of low-valent metals can be utilized even in lithium-excess oxyfluoride materials. Early works on fluorination attempted to introduce fluorine into well-ordered lithium metal oxides that are thermodynamically stable. However, because of the extremely small fluorine solubility in these stable phases, the majority of the incorporated fluorine ions were found to reside near the surface, forming a lithium-fluoride coating layer,[220−224] or only a small amount of fluorine was doped into the structure.[225−230] In contrast, work on Li_2VO_2F and Li_2CrO_2F has demonstrated that a substantially high fluorination level can be accommodated in the metastable-disordered rock-salt phase in a solid-solution form.[219,231] The significantly higher fluorine solubility in the disordered phase originates from the presence of metal-poor, lithium-rich local environments in the structure, as evidenced in the theoretical investigation of Richards et al.[214] In their study, both ordered and disordered lithium metal oxides were predicted to preferentially incorporate fluoride ions at sites where less high-energy metal−fluorine bonds were formed. Disordering provided much more diverse anion coordination forms, consequently leading to higher fluorine solubility.

In the pursuit of maximizing the redox capacity of cations, disordered rock-salt oxyfluorides were investigated with particular attention paid to multielectron redox couples such as V^{3+}/V^{5+},[219,232,233] Cr^{3+}/Cr^{5+},[231,234] and Mo^{3+}/Mo^{6+}.[235] Chen et al. fabricated nanosized disordered Li_2VO_2F using a simple ball-milling method with Li_2O, LiF, and V_2O_3 as precursors.[219] The obtained Li_2VO_2F electrode delivered a capacity of 420 mAh g^{-1} during the first discharge at 40 °C and 1.3−4.1 V, which is close to the theoretical capacity of 462 mAh g^{-1}, assuming the two-electron V^{3+}/V^{5+} redox process. A reversible structural change involving a volume change of only 3.3% was confirmed, validating the practicality of using disordered oxyfluorides as cathode materials. To clarify the role of fluorine in the electrochemical performance in detail, a comparative study of isostructural disordered Li_2VO_3 and Li_2VO_2F was conducted in a subsequent work.[232] Salient differences were observed in terms of the discharge capacity, voltage, and Li^+ transport among the examined properties during the first and second cycling. While the disordered Li_2VO_3 delivered a discharge capacity of 295 mAh g^{-1},

DOI: 10.1021/acs.chemrev.9b00405
Chem. Rev. XXXX, XXX, XXX−XXX

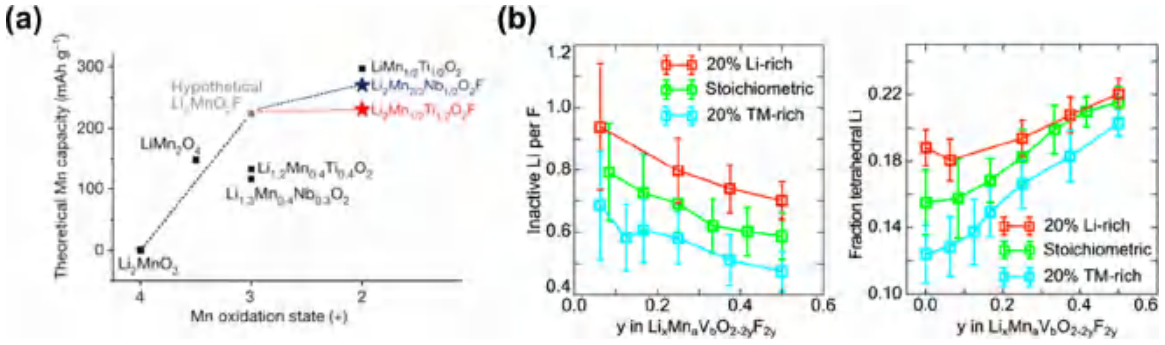

Figure 29. (a) Design of oxyfluorides with high theoretical Mn capacity. (b) (left) Electrochemical accessibility of Li in Li−Mn−V oxyfluoride cathode materials as a function of fluorination level. (right) Expected population of tetrahedral Li sites during charge.[15] Reproduced with permission of ref 15. Copyright 2018 Springer Nature.

corresponding to one Li^+ intercalation involving V^{5+}/V^{4+} reduction, the disordered Li_2VO_2F provided a substantially higher capacity of 330 mAh g^{-1}, corresponding to a 1.4 Li^+ intercalation compensated mainly by a $V^{4.4+}/V^{3+}$ reduction. Moreover, Li_2VO_2F exhibited a 0.3-V higher average discharge voltage compared with that of Li_2VO_3, which was attributed to the inductive effect of the highly electronegative fluoride ligand. Electrochemical impedance spectroscopy (EIS) measurements verified the higher Li^+ diffusivity in Li_2VO_2F ($D_{Li^+} \approx 10^{-9}$ cm s^{-1}) than in Li_2VO_3 ($D_{Li^+} \approx 10^{-11}$ cm s^{-1}). The authors attributed the improved Li^+ kinetics in Li_2VO_2F to the lower electrostatic repulsion between Li^+ and neighboring V^{3+} during Li^+ hopping relative to the repulsion between Li^+ and V^{4+} in Li_2VO_3. Other approaches have been employed to produce disordered Li_2VO_2F through the deep lithiation of rhombohedral VO_2F, which is synthetically accessible using both a solid-state reaction and ball milling.[233,236] Deep lithiation of VO_2F irreversibly converted the phase from rhombohedral to disordered cubic phases,[215,237] and resulted in analogous electrochemical properties to those of the mechanochemically synthesized Li_2VO_2F. In a related study, Takeda et al. reported on disordered $Li_{1+x}MoO_2F_x$ ($0 \le x \le 2$) prepared by mechanical milling.[235] High theoretical capacities of more than 300 mAh g^{-1} were estimated for the series of compounds, for example, by assuming a three-electron Mo^{3+}/Mo^{6+} redox for $x = 2$ ($Li_3MoO_2F_2$) or a two-electron Mo^{3+}/Mo^{5+} redox for $x = 1$ (Li_2MoO_2F). Among the considered compositions, Li_2MoO_2F exhibited the largest reversible capacity of over 300 mAh g^{-1} at room temperature. Although Li_2MoO_2F delivered a capacity that was comparable to the theoretical value involving the reversible Mo^{3+}/Mo^{5+} redox, other fluorinated samples delivered much smaller capacities relative to their theoretical values. The authors attributed this disparity to the loss of electrical conductivity resulting from the enrichment of insulating F^- ions and the reduction of conductive Mo^{3+} ion content.

Despite the advantages of vanadium- and molybdenum-based oxyfluorides in terms of capacity, their low average voltage remains an issue. To this end, Chen et al. noted the higher redox potential of the Cr^{3+}/Cr^{4+} couple than the V^{3+}/V^{4+} couple and replaced vanadium in disordered Li_2VO_2F with chromium, producing a series of materials of formula $Li_2V_xCr_{1-x}O_2F$ ($x = 0, 0.2, 0.5, 0.8$).[231] With increasing chromium content, the main redox peaks in the CV analysis shifted from 2.5 to 3.5 V, indicating a larger contribution of the Cr^{3+}/Cr^{4+} couple. Benefitting from the increased discharge voltage and the relatively constant capacity over the range of $0.2 \le x \le 0.8$, the highest specific energy was achieved for $x = 0.2$, i.e., $Li_2V_{0.2}Cr_{0.8}O_2F$. Furthermore, the mixing of chromium and vanadium enhanced the cycling stability compared with that of their V- or Cr-only counterparts, with the best capacity retention achieved at $x = 0.5$. XANES analysis in a subsequent work verified that the local structure around the V and Cr ions is well preserved after cycling of $Li_2V_{0.2}Cr_{0.8}O_2F$ in contrast to the irreversible variations observed in Li_2VO_2F and Li_2VO_2F.[234] Oxyfluorides with high voltage can also been obtained by utilizing high-voltage trivalent redox couples such as Mn^{3+}/Mn^{4+}, Fe^{3+}/Fe^{4+}, and Co^{3+}/Co^{4+}.[190] However, the use of these trivalent couples can severely limit the capacity in the absence of other redox reservoirs because reaching metal oxidation states above 4+ requires a prohibitively high voltage. House et al. overcame this limitation by inducing the redox of both manganese and oxygen species.[16] In their study, disordered $Li_{1.9}Mn_{0.95}O_{2.05}F_{0.95}$, which was prepared by a ball-milling process targeting the Li_2MnO_2F composition, yielded an initial discharge capacity of 283 mAh g^{-1} with an average potential of 3.4 V. The Mn^{3+}/Mn^{4+} redox was demonstrated to be responsible for at most ~230 mAh g^{-1} of this capacity, with oxygen redox providing the extra capacity. Unexpectedly, $Li_{1.9}Mn_{0.95}O_{2.05}F_{0.95}$ did not suffer from oxygen loss from the lattice unlike other lithium-excess materials that exploit the oxygen redox; however, the underlying mechanism by which the oxygen redox is stabilized is not yet clear.

Considering the compromise between the redox capacity and voltage of transition metals, a critical issue to achieve the highest energy density from metal redox processes was to circumvent the negative correlation between these two properties. Some of the most recent studies have succeeded in simultaneously achieving both high capacity and high average voltage by inducing Mn double redox.[15,190,238] To this end, high-valent d^0 species (Ti^{4+}, Zr^{4+}, Nb^{5+}, Sb^{5+}, Mo^{6+}, etc.) and low-valent fluorine anions were combined in the disordered phases (Figure 29a). Lee et al. devised disordered $Li_2Mn_{2/3}Nb_{1/3}O_2F$ and $Li_2Mn_{1/2}Ti_{1/2}O_2F$ compositions that are synthesizable using mechanochemical ball milling.[15] The presence of Nb^{5+} (or Ti^{4+}) and F^- produced Mn^{2+} in the discharged state so that theoretical Mn^{2+}/Mn^{4+} redox capacities of 270 and 230 mAh g^{-1} were expected for $Li_2Mn_{2/3}Nb_{1/3}O_2F$ and $Li_2Mn_{1/2}Ti_{1/2}O_2F$, respectively. Cycling of $Li_2Mn_{2/3}Nb_{1/3}O_2F$ resulted in a high discharge capacity comparable to or higher than the theoretical Mn^{2+}/Mn^{4+} capacity depending on the cutoff voltages, along with a relatively high average discharge voltage over 3.0 V; $Li_2Mn_{1/2}Ti_{1/2}O_2F$ also delivered similar electrochemical

DOI: 10.1021/acs.chemrev.9b00405
Chem. Rev. XXXX, XXX, XXX−XXX

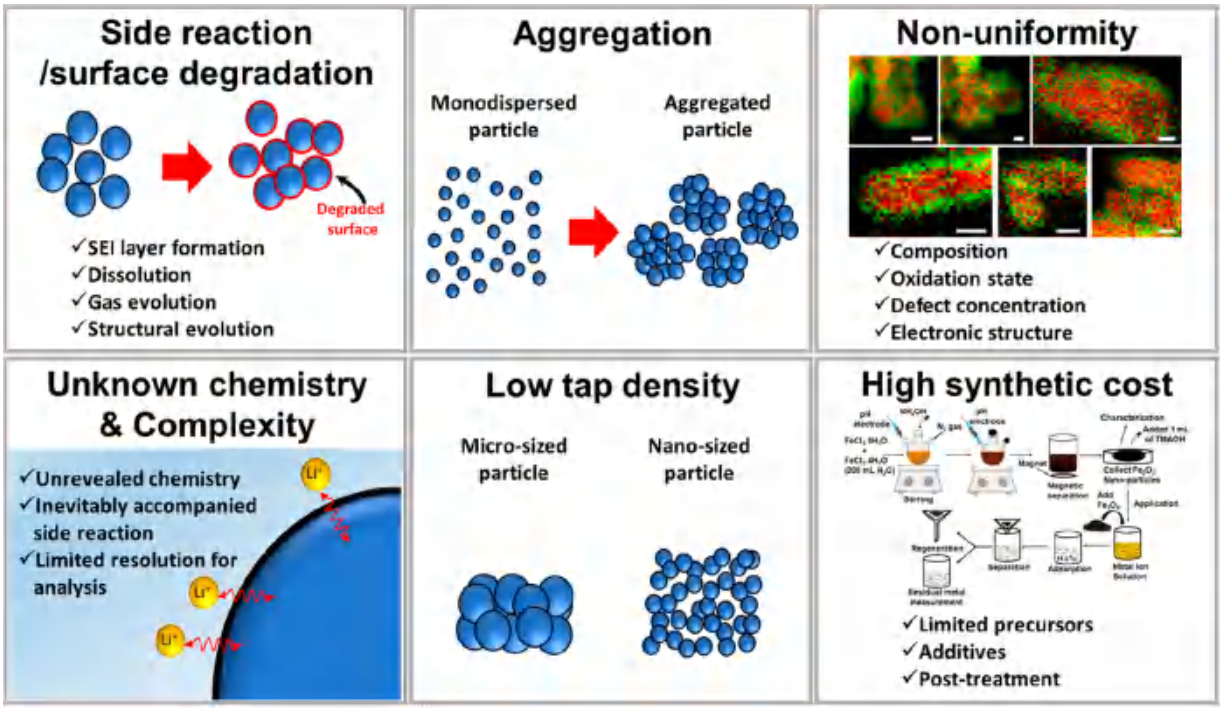

Figure 30. Schematic illustration and brief description of chronic issues associated with nanomaterials that must be overcome.[239,240] Reproduced with permission of ref 239. Copyright 2015 American Chemical Society. Reproduced with permission of ref 240. Copyright 2016 Wiley-VCH Verbg GmbH & Co. KGaA.

properties. The XANES measurements elucidated the predominant Mn^{2+}/Mn^{4+} redox and the small fraction of oxygen redox beyond the Mn redox. Notably, $Li_2Mn_{2/3}Nb_{1/3}O_2F$ exhibited negligible O_2 evolution even after charging to 5.0 V, benefitting from the limited utilization of the oxygen redox. As a result, the voltage and capacity fading typical for materials with excessive use of oxygen redox were dramatically mitigated, suggesting the use of Mn double redox couples as a promising strategy to achieve cycling stability of lithium-excess materials. While maintaining the Mn double redox, Kitchaev et al. substituted redox-inactive d^0 elements with a redox-active high-valent element to additionally employ the redox of high-valent cations.[190] Disordered $Li_{1.143}Mn_{0.286}V_{0.572}O_2$, $Li_{1.171}Mn_{0.343}V_{0.486}O_{1.8}F_{0.2}$, $Li_{1.133}Mn_{0.400}V_{0.467}O_{1.8}F_{0.2}$ (metal-rich variant), and $Li_{1.23}Mn_{0.255}V_{0.515}O_{1.8}F_{0.2}$ (lithium-rich variant) were synthesized as representative compounds targeting the combination of Mn^{2+}/Mn^{4+} and V^{4+}/V^{5+} couples. Although all four compounds provided high reversible capacity and energy density with observations of Mn^{2+}/Mn^{4+} and V^{4+}/V^{5+} redox, their practical capacities were much lower than the theoretical value assuming Mn^{2+}/Mn^{4+} and V^{4+}/V^{5+} couples. On the basis of a precise comparison of the four compounds, the authors identified that the distribution of lithium site energies in the disordered structure, rather than the accessibility of transition-metal redox couples, determined the observed subtheoretical capacity. Specifically, the existence of strong lithium−fluorine bonds and the formation of high-voltage tetrahedral lithium sites restricted the accessibility of lithium extraction in the high-voltage region (Figure 29b), leaving the task of finely tuning the chemistry of oxyfluorides to achieve desired energy densities to future work.

4. PART 3: LIMITATIONS OF NANOMATERIALS AND STRATEGIES TO OVERCOME THESE LIMITATIONS

4.1. Limitations of Nanomaterials in Battery Systems

The strategy of nanosizing electrode materials not only provides an opportunity to find new battery chemistries but also results in a remarkable improvement in their electrochemical properties. Nevertheless, the application of nanomaterials to practical battery systems is also met by inherent limitations, as graphically summarized in Figure 30. The high synthetic cost and low tap density makes the utilization of nanomaterials in various energy storage platforms difficult. Moreover, although the large surface area of nanomaterials significantly increases their electrochemical activity in terms of the kinetics, it is also inevitably accompanied by side reactions or oxidized surfaces, which lead to degradation of the active materials. The positive and negative effects of nanomaterials are in constant competition in electrochemical systems, and sometimes the drawbacks outweigh the merits, leading to inferior battery performance.

A comprehensive understanding of the correlation between nanomaterials and their electrochemical properties is necessary because of the inherent nonuniform characteristics in the intraparticle space, such as the composition, oxidation state, and defect concentration, which are commonly observed in nanomaterials. In addition, attaining a deep understanding of the surface reactivity of nanomaterials remains challenging because many factors are simultaneously involved, such as the crystal facet, aggregation, and complex interactions with electrolytes. In this section, we categorize and describe the challenges facing nanomaterials that need to be addressed for their practical application. We also introduce the underlying origins of “nano” characteristics, including advanced strategies to overcome these challenges.

DOI: 10.1021/acs.chemrev.9b00405
Chem. Rev. XXXX, XXX, XXX−XXX

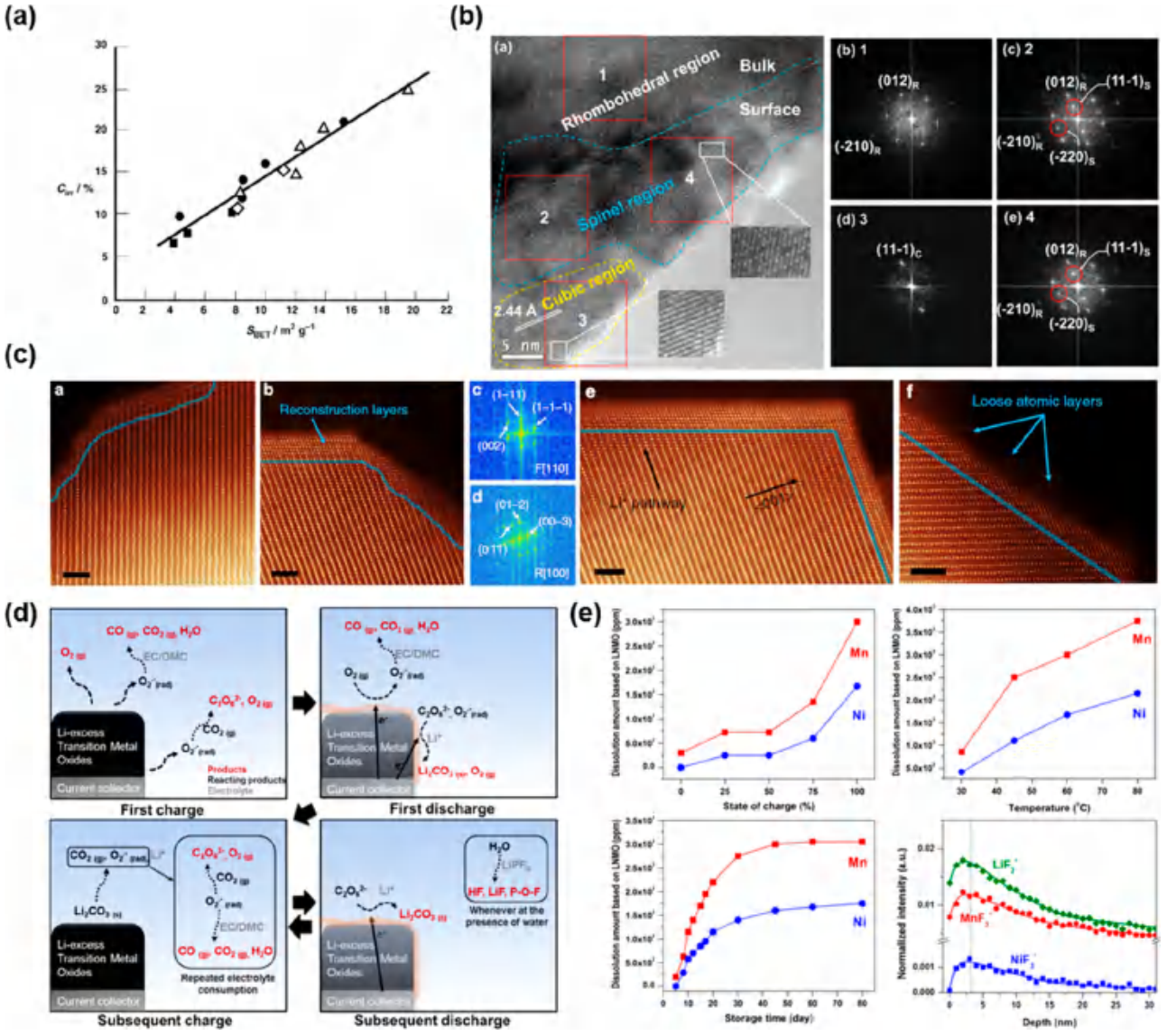

Figure 31. Side reactions and surface degradation of electrode materials at the nanoscale. (a) Irreversible capacity loss during the first cycle of a graphite anode due to SEI layer formation.[241] Reproduced with permission of ref 241. Copyright 2005 Wiley-VCH Verlag GmbH & Co. KGaA. (b,c) Surface crystal structure evolution of NCM cathode materials in the range of a few nanometers.[244,245] Reproduced with permission of ref 244. Copyright 2013 Wiley-VCH Verlag GmbH & Co. KGaA, Reproduced with permission of ref 245. Copyright 2014 Springer Nature. (d) Gas evolution process at the interface between the electrolyte and Li-rich cathode materials.[217] Reproduced with permission of ref 217. Copyright 2012 American Chemical Society. (e) Transition metal dissolution of NCM cathode materials as a function of SoC, temperature, and aging time.[254] Reproduced with permission of ref 254. Copyright 2013 American Chemical Society.

4.1.1. Surface Reactivity (Side Reactions, Surface Degradation/Aggregation). Deterioration of the electrochemical performance of battery systems occasionally results from side reactions or material degradation occurring at the electrode surface on both the anode and cathode side. It is often attributable to the vulnerability of the surface in contact with the electrolyte or external conditions, which can trigger serious degradation of a battery. Here, we briefly introduce the side reactions and surface degradation generally observed in battery systems without focusing solely on nanomaterials. Nevertheless, it needs to be pointed out that these issues are more critical to nanomaterials than to microsized materials because the large surface area of nanomaterials will promote these side reactions and accelerate the degradation of materials.

4.1.1.1. Side Reactions and Surface Degradation. The formation of a SEI layer on anode materials, which is a well-known and essential side reaction for stable cycling, leads to consumption of Li ions supplied from the cathode side, resulting in an irreversible capacity and a low Coulombic efficiency.[241,242] In particular, because nanomaterials have a significantly larger surface area, much higher irreversible capacity is often observed in nanomaterials than in bulk materials. As a representative example, Figure 31a shows that the irreversible capacity increases proportionally to the BET surface area of the graphite anode material.[241] The relationship between the active surface area and irreversible capacity shows a clear dependence on the particle size of graphite, with a 7 mAh/m^2 increase in the irreversible capacity increase observed per BET square meter.[242] On the cathode side, preferred surface-driven side reactions, such as surface structure change, gas evolution, and transition metal dissolution in the electrolyte, mostly contribute to the reduction of the

DOI: 10.1021/acs.chemrev.9b00405
Chem. Rev. XXXX, XXX, XXX−XXX

electrochemical performance of the cells. Surface structural evolution is usually observed in layered- and spinel-type oxide materials after electrochemical cycling with a high voltage cutoff of more than 4 V (vs Li). The structural evolution from layered to spinel-like or rock-salt phase can yield a degraded region with a thickness of a few tens of nanometers in a 300−600 nm particle,[243−246] as shown in Figure 31b,c. This structural evolution increases the charge-transfer resistance and kinetically hinders the Li-ion diffusion from the surface to the bulk region, leading to cycle degradation.[244] These findings indicate that a decrease of the particle size can result in more severe and faster structural evolution, leading to a rapid increase of the charge-transfer resistance of active materials. This undesirable effect competes with the effect of the short diffusion length in terms of kinetics.

Evolution of gases such as O_2 and CO_2 at the electrode surface can be fatal to the safety of Li-ion batteries as this can lead to swelling of the battery package or explosion in extreme cases. Gas phases can evolve from the interfacial reaction between the electrode and electrolyte as well as from the electrode material itself, as shown in Figure 31d.[217] Oxygen radicals generated from the electrode surface can repeatedly induce electrolyte consumption and decomposition. For example, in lithium-excess Ni−Co−Mn (NCM)-based cathode materials, O_2 and CO_2 gas evolution have been observed during charge.[247−249] The oxygen gas was detected at the end of the charge and originated from the lattice, whereas the majority of the CO_2 gas evolved from the electrolyte and resulted from side reactions involving the oxygen.[247,248] In another case, Renfrew et al. claimed that residual lithium precursors, such as Li_2CO_3, remaining on the material surface after synthesis more dominantly promote CO_2 or CO gas evolution.[250] These results regarding gas evolution indicate that the reactivity properties of the surface of electrode materials should be carefully considered for nanosized materials with large surface areas.

Transition metal dissolution is another major issue occurring at electrode material surfaces and has representatively been studied in NCM-based layered and Mn-based spinel cathode materials. The dissolution occurs mainly at the surface and results from the interaction with the electrolyte and HF attack. The dissolution is regarded as one of the origins of cycle degradation because of the deteriorating effect of the dissolved transition metal ions on the SEI layer of the anode.[251−253] For Mn-based spinel cathode materials, Mn or Ni ions easily dissolve in the electrolyte depending on the SoC, temperature, and storage time, as shown in Figure 31e.[254] The dissolved Mn ions form inactive surface layers consisting of MnF_2 on the cathode when an electrolyte containing a fluorine-containing lithium salt (e.g., $LiPF_6$) is used, which increases the cell impedance. In addition, the migration of dissolved Mn^{2+} ions to the anode can induce unnecessary electron consumption as the reduction of Mn ions promotes the decomposition of the electrolyte and Li consumption, resulting in the formation of a undesirable SEI layer.[251,252] For $Li(Ni,Co,Mn)O_2$-based layered materials, Gallus et al. demonstrated that the amount of dissolved transition metal ions in the electrolyte can be reduced by using $LiBF_4$ or $LiPF_6$ salts rather than $LiClO_4$,[253] as the oxidized perchlorate ion easily reacts with the electrolyte and transforms into perchloric acid.[255] Recently, Fan et al. suggested that HF can be formed by proton transfer from the surface of the active material to the electrolyte, which suggests that nanomaterials with large surface areas capable of absorbing protons may be critical to electrolyte stability and emphasizes the need for surface engineering.[256] These dissolution problems have been a chronic problem in battery systems and should be resolved not only for ceramic-based electrode materials but also for organic electrode materials.[257]

4.1.1.2. Aggregation. Aggregation of nanoparticles not only inhibits the large-scale synthesis of nanomaterials but also leads to deterioration of electrode performance. The kinetics of electrochemical reactions governed by the active surface area can be significantly depreciated when nanoparticle aggregation gradually reduces the practical surface area. Moreover, aggregation makes it difficult to retain the original particle size and morphology, which could have been optimized for the optimal performance of the electrode. Aggregation by electrochemical reactions can be typically observed in the conversion and alloying reactions owing to the recombination reactions of sub-Angstrøm-level clusters. In general, the metal nanoclusters, which are the main redox sources, are easily aggregated into a larger size, and the lumpy particle loses its electrochemical activity because of reduction of its active surface area.[80,258,259] Thus, the mobility of transition metals was regarded as one of the critical factors determining the cyclability of conversion electrodes. For example, a FeF_2 electrode based on $FeF_2 + 2Li \rightarrow 2LiF + \text{nano-Fe}$[260] exhibits a respectable cycle stability, whereas the similar chemistry of CuF_2 shows far inferior performance. This was attributed to the higher mobility of Cu ions than Fe ions, which leads to the formation of largely aggregated Cu nanoparticles, inducing irreversibility of the reconversion reaction from Cu to CuF_2 (Figure 32a).[80] This phenomenon results in poor cyclability and a drastic reduction of the electrochemical activity during the conversion/reconversion reaction of CuF_2. Similarly, in the alloying reaction, a large volume expansion can cause aggregation or pulverization of particles. Intraparticle cracks that induce pulverization can be formed from the accumulated energy of strain resulting from volume expansion for large particle sizes; however, nanoparticles usually aggregate with other nanoparticles via compressive stress on the grain boundary resulting from volume expansion. For example, to prevent the aggregation of Sn nanoparticles in an alloying reaction, a carbon matrix was adopted to prepare a Sn/C nanocomposite. The use of the carbon matrix effectively prevented the aggregation of Sn nanoparticles even after 200 cycles, as shown in Figure 32b.[261]

The driving force of aggregation is usually known as the destabilized free energy from the high surface-area-to-volume ratio of nanoparticles. Detailed parameters affecting the driving force of aggregation have been studied in the field of colloid science using the Derjaguin−Landau−Verwey−Overbeak (DLVO) theory.[262−264] DLVO theory thermodynamically considers the competition of attractive and repulsive forces between two nanoparticles when they collide together by Brownian motion. The attractive van der Waals force induced by the interaction of electrons in two particles competes with the electrostatic double-layer repulsive force induced by charged surfaces. As illustrated in Figure 32c, the net force is determined by a function of the separation distance between the particles, and an attractive force is dominant in a primary and secondary well region. In the primary well region, particles irreversibly aggregate together, forming a large cluster, whereas particles reversibly aggregate in the secondary well region and can maintain a dispersed state when appropriate forces are applied.[265] The nanoparticle aggregation behavior can include

DOI: 10.1021/acs.chemrev.9b00405
Chem. Rev. XXXX, XXX, XXX−XXX

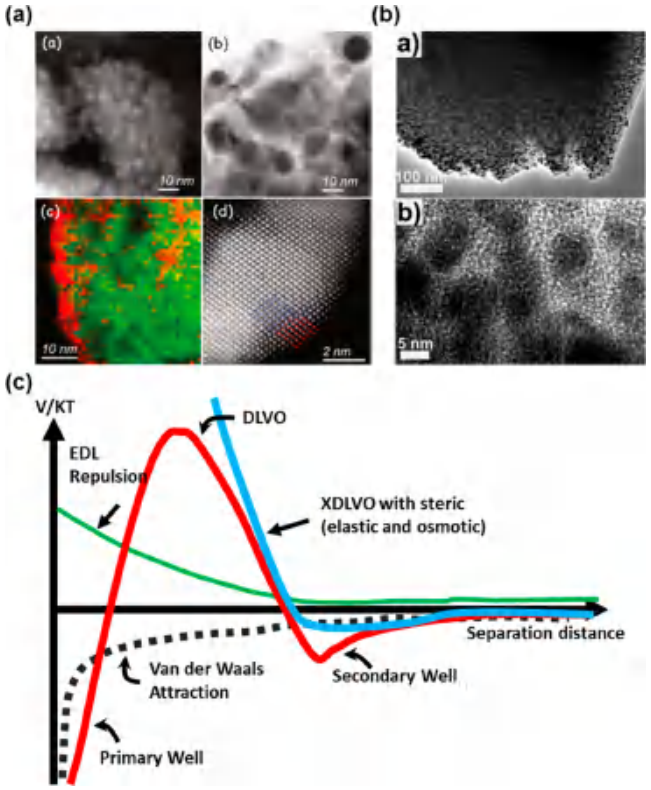

Figure 32. Aggregation of nanoparticles during battery operation and the fundamental origins thereof. (a) TEM images of CuF_2−C electrodes at initial and lithiated states. The red and green colors represent LiF and the Cu metal phase, respectively.[80] Reproduced with permission of ref 80. Copyright 2011 American Chemical Society. (b) TEM and HR-TEM image of a Sn−C composite after 200 cycles.[261] Reproduced with permission of ref 261. Copyright 2014 American Chemical Society. (c) Driving force of aggregation of nanoparticles as a function of distance between nanoparticles (DLVO theory). The net force is determined by the competition between the electrostatic double layer (EDL) repulsion force and the attractive van der Waals force. Compared with DLVO, XDLVO additionally considers magnetic attraction, osmotic repulsion, and steric repulsion.[262] Reproduced with permission of ref 262. Copyright 2010 American Society of Agronomy.

other parameters, such as magnetic attraction, osmotic repulsion, and steric repulsion (XDLVO, extended DLVO theory). Although DVLO and XDLVO theory describe the nanoparticle aggregation behavior, many challenges remain to explain the behavior in the electrochemical systems because of the particle size, morphology, composition, and inseparable correlation among electrochemical forces. While these theoretical inputs can serve as a reference to understand the aggregation phenomenon, better strategies need to be developed for the practical application of nanomaterials in electrochemical systems.

4.1.2. Physical and Chemical Nonuniformity of Nanomaterials. The high surface-area-to-volume ratio of nanomaterials often leads to physical/chemical nonuniformity of surface states compared with the bulk region. The electronic structure and chemical composition of the surface also tend to be different from those of the bulk in order to minimize the overall surface free energy. While these different physical or chemical states of surfaces may offer the novel properties described above, the loss of uniformity poses a new challenge in controlling the electrode chemistry.

Qian et al. showed that the average electronic spin state of $LiCoO_2$ can be altered with particle size,[7] where the Co ions in the bulk region have low spin states; on the other hand, for the particles below 10 nm, the low-spin state portion of the Co^{3+} ion falls to 92.9%. The mid- or high-spin state of the Co^{3+} ion increases from 1.2% to 7.1% upon decreasing the particle size from 30 to 10 nm (Figure 33a). The spin transition occurs to minimize the surface energy of the (104) and (110) planes, which have an oxygen coordination number lower than six. This stabilization of the surface free energy affects the de/intercalation potential of lithium ions in the surface region of the $LiCoO_2$ electrode, which differs from the value expected for the bulk $LiCoO_2$. It implies that, without precise information on the surface-to-bulk ratio or the particle-size distribution, prediction of the electrode potential, which is important for the practical assembly of the battery, may not be trivial. Chung et al. also demonstrated that Li/Fe disordering defects in $LiFePO_4$ are mainly distributed on the surface of the nanocrystal because of its stabilized defect formation at the surface.[266] The defect formation energy was found to be anisotropic with respect to the crystallographic orientation (Figure 33b), indicating that the morphology control of $LiFePO_4$ can be more complicated, not only considering the typical lithium diffusion channel in the bulk crystal but also perceiving the nature of preferred defect formations in specific surface directions.

A high surface energy can also induce inhomogeneity of anions in the synthesis of nanoparticles. For iron oxyfluoride cathode materials, the elemental separation of oxygen and fluorine in a single nanoparticle was observed by EELS, as shown in Figure 33c.[239] A FeOF nanoparticle was separated into an O-rich shell and an F-rich core region, where the reversible oxidation and reduction occurred. The O-rich shell region remained in the O-rich rock-salt phase during subsequent cycling, and only the F-rich core region underwent a phase transition between bcc-Fe metal and the F-rich rutile phase via a conversion/reconversion reaction. The inhomogeneity of the anionic fluorine and oxygen species may have resulted from the limited diffusion distance of oxygen when fluorine was replaced by oxygen or the thermodynamic stability of the oxygen-substituted phase itself. Li et al. discussed that compositional inhomogeneity can induce a large voltage hysteresis during conversion and reconversion reactions for the nanosized FeF_3 electrode.[125] Spatial inhomogeneity of the composition results from the difference in the reaction kinetics between the bulk and surface regions. As a result, the distinctive phase evolution of the surface compared with that of the bulk induces voltage hysteresis during charge/discharge, as shown in Figure 33d. Park et al. reported that the inhomogeneity of the nanomaterials is inherent from the synthesis and can vary depending on the average sizes of the particles.[267,268] In the synthesis of magnetite (Fe_3O_4) nanoparticles, the portion of the more-oxidized maghemite (Fe_2O_3) increased as the particle size decreased from 13 to 4 nm. The average oxidation state increased as the particle size decreased because of the large contribution of Fe^{3+} ions compared with that of Fe^{2+} ions, as shown in Figure 33e. Therefore, Fe_2O_3 became the main phase in the 4 nm iron oxide nanoparticles, indicating the difficulty in securing the phase purity and homogeneity in the preparation of nanosized electrode materials.

4.1.3. Low Tap Density. Decreasing the particle size to the nanometer scale creates a substantial amount of interparticle

DOI: 10.1021/acs.chemrev.9b00405
Chem. Rev. XXXX, XXX, XXX−XXX

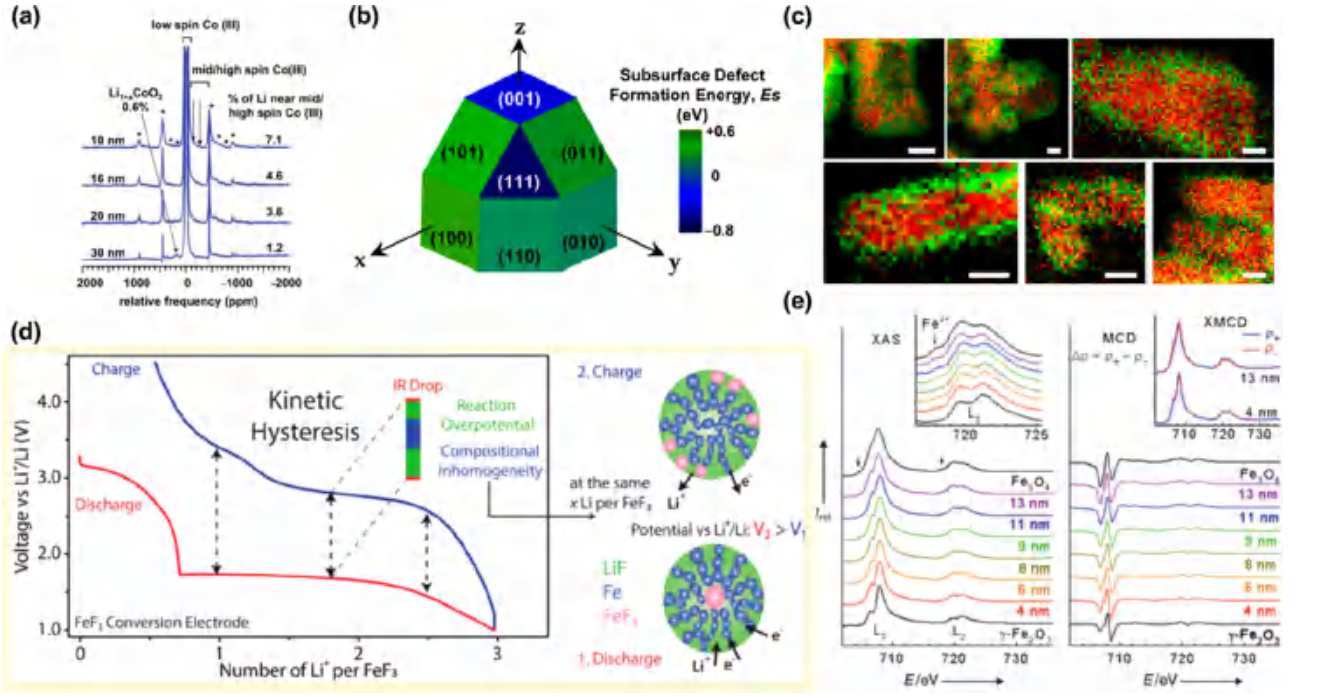

Figure 33. Nonuniform properties of nanoparticles. (a) ^{7}Li MAS NMR spectra of nano $LiCoO_2$ as a function of particle size. The percentage of high-spin Co^{3+} increases with decreasing particle size.[7] Reproduced with permission of ref 7. Copyright 2012 American Chemical Society. (b) Highly anisotropic characteristics of antisite defect formation energy of $LiFePO_4$ at each surface.[266] Reproduced with permission of ref 266. Copyright 2015 American Chemical Society. (c) Chemical nonuniformity in FeOF by separation of oxygen-rich shell and fluorine-rich core.[239] Reproduced with permission of ref 239. Copyright 2015 American Chemical Society. (d) Kinetic hysteresis in FeF_3 resulting from compositional inhomogeneity at the nanoscale and schematic figure of chemical distribution.[125] Reproduced with permission of ref 125. Copyright 2016 American Chemical Society. (e) XAS and X-ray magnetic circular dichroism (XMCD) of Fe_3O_4 nanoparticles as a function of particle size. The Fe_2O_3 character gradually stands out as the particle size decreases from 13 to 4 nm.[267] Reproduced with permission of ref 267. Copyright 2005 Wiley-VCH Verbg GmbH & Co. KGaA.

space, resulting in a low tap density of electrode materials. The low tap density inevitably leads to not only a low volumetric capacity but also necessitates a thick electrode to achieve a comparable packing level as a conventional electrode.[244,269−273] For example, the tap density of nano-Si particles with a 150 nm diameter is approximately 0.15 g cm^{-3}, whereas the theoretical bulk density of Si is almost 2.33 g cm^{-3}, which results in approximately 15 times less volumetric energy density and requires a much greater thickness than that of bulk powders.[274,275] The use of the low tap density materials followed by the thick electrode results in several disadvantages in terms of the electrochemical performance. The lithium-ion diffusion distance from the counter electrode to and from an active surface through the electrode pores significantly increases with increasing thickness of the electrode. As a result, the increased diffusion distance causes a large cell polarization and makes it difficult for the electrode to achieve a high rate capability despite the expected fast kinetics in the individual nanoparticles. Moreover, poor cycle life can result from the severe current concentration, which is attributed to unbalanced traveling paths between electrons and guest ions.[276,277] While applying a manufacturing process, such as calendaring, may lead to a dense electrode that has a shortened overall lithium-ion diffusion length and well-connected electrical pathway.[278] the rolling process generates mechanical cracks or fractures on the particles due to its high stress and sometimes cuts the electric or ionic path off, in addition to leading to a nonuniform particle distribution. To overcome these problems, the development of advanced electrode processes and the reduction of the internal volume of nanomaterials are critical to maximizing the benefits of nanoparticles.

4.1.4. High Synthetic Cost and Alternatives. According to the cost structure of battery components, the electrode materials generally account for more than half of the total cost of the battery components.[279] The additional nanosizing of the active materials inevitably results in an increase of the electrode cost; thus, it is essential to consider and minimize the cost of nanosizing to achieve economic viability. Lithium-containing nanoparticles are often highly air-sensitive due to their large exposed surface area and are thus synthesized and stored more carefully in low-H_2O and -O_2 environments, resulting in a further increase of the material cost. Many studies have used hydrothermal reactions,[40,280] the sol−gel method,[281−283] and aerosol-spray pyrolysis[284] to synthesize nanocrystalline materials. These methods can be manipulated for upscaling; however, costs may rise because they generally require the control of subtle reaction conditions (such as the reaction temperature, pressure, solvent selectivity, and reactant ratio) to synthesize a product with size monodispersity. The use of additives for down-sizing also increases costs and requires additional post-treatment processes to eliminate the additives. Planetary ball milling has been used to reduce particle sizes simply by controlling the rotation speed and time, without the need for complex synthesis schemes or reaction conditions. The planetary ball milling method may compete with the synthesis of nanocrystalline materials in a simple batch, however, the control of the homogeneity of materials, the uneven particle-

DOI: 10.1021/acs.chemrev.9b00405
Chem. Rev. XXXX, XXX, XXX−XXX

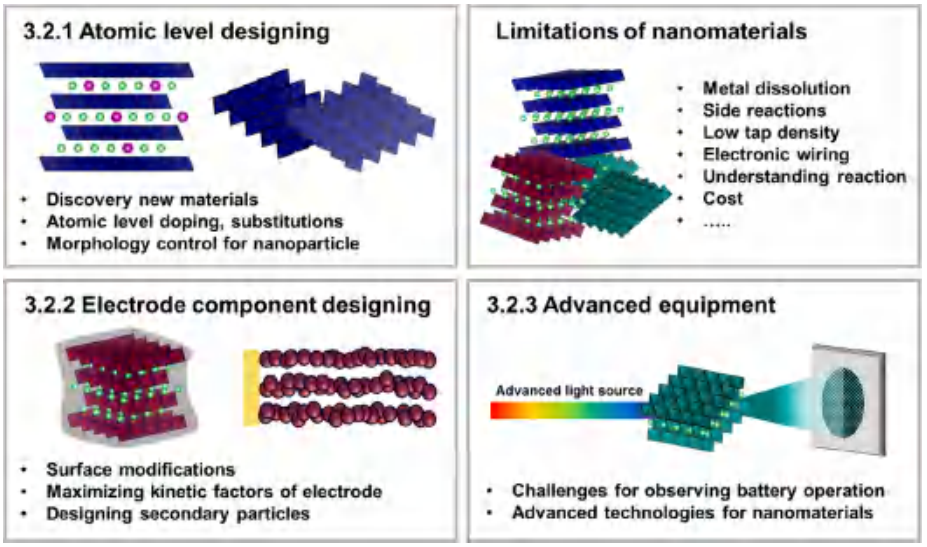

Figure 34. Schematic illustration of the three main categories described in section 3.2. Approaches to overcoming and understanding nanomaterials in terms of atomic-scale redesign, electrode design engineering, and new advanced techniques. Each block illustrates the representative nanostrategy for each length scale for battery systems.

size distribution, defects generated by the strong physical collisions, and suitability for mass production remain challenges. As further material developments have been made with multiatomic compositions[285] such as mixed nickel, cobalt, and manganese for cathodes or various alloy types for anodes, uniformity has remained one of the most important issues and is critical in the quality control of battery systems employing nanomaterials.

4.2. Strategies to Overcome the Limitations of Nanomaterials

The current limitations of employing nanomaterials in electrochemical systems have delayed the successful utilization of the interesting new properties uncovered by nanoelectrochemistry and have prohibited their commercial feasibility. However, intensive recent efforts have identified a few important strategies that may overcome these limitations. In this section, we introduce these attempts with respect to (i) atomic-scale redesign of nanomorphologies, (ii) electrode design engineering, and (iii) new, advanced techniques for the observation of nanomaterial-dependent electrochemical phenomena as illustrated in Figure 34. The main principle of each strategy will be discussed with some examples provided.

4.2.1. Atomic-Scale Redesign of Nanomorphologies. 4.2.1.1. Dimensional Classification of Nanostructures. Nanomaterials are generally classified by their structural dimensionalities; 0D (clusters and small particles), 1D (nanotubes and nanowires), 2D (nanoplates and layers), and 3D (hierarchical nanostructures) nanostructured materials (NSMs).[286] As NSMs with different dimensionalities will experience different Li^+ ion diffusion modes, active surface ratios and Li-ion storage properties controlling their nanoarchitectures is a potentially useful method for improving the electrochemical performances of active materials.[287,288]

0D NSMs, such as clusters, which can shorten Li^+ ion diffusion paths in all directions, have been studied to resolve the generally poor Li^+ ion and electron conduction within the materials. Many researchers have synthesized a range of 0D NSMs with high crystallinity, demonstrating significantly enhanced rate performances.[289] In addition, nanoparticles with large surface energies could trigger reaction paths through nonequilibrium phase transitions. For example, $LiFePO_4$ nanoparticles deliver better rate performance by suppressing phase separation, which proceeds by deviating from its thermodynamically equilibrium state.[290] Nevertheless, 0D NSMs generally have large surface areas in contact with the electrolyte, which often deteriorates their stabilities and triggers side reactions (see section 4.1).

1D nanostructures are attractive morphologies for Li-ion batteries due to the short Li-ion diffusion along the radial direction, fast electron conduction along the 1D direction, and their structural variety, such as nanotubes or nanowires.[291,292] For example, single crystalline nanotubes of spinel $LiMn_2O_4$ with a 200 nm wall thickness showed an excellent rate performance along with high structural stability.[293] It was demonstrated that 70% of the initial capacity was maintained over 1500 cycles at a current density of 5 C. Moreover, core−shell type Si nanowires exhibited about 90% of their initial capacity after 100 cycles as the nanowire architecture could relax the internal strain and prevent pulverization over repeated cycles.[292]

2D NSMs can provide more well-defined Li-storage sites compared with 0 or 1D NSMs, generally showing the highest energy density among the various nanostructures.[294] Nanoplates or nanosheet-like structures facilitate the charge transfer of Li-ions from an electrolyte, significantly increasing both energy and power densities.[295,296] However, the large surface area of 2D materials can also cause electrochemical irreversibility during cycles due to the consumption of electrolytes or structural deformation.[137]

3D NSMs are usually assembled from 0D, 1D, or 2D NSMs in an effort to circumvent the major problems of each nanostructure such as material instability or low tap-density.[297,298] For instance, hollow microsphere 3D NSMs composed of V_2O_5 nanorods exhibited much improved energy densities, capacity retention, and rate capability because their mesoporosity provides a greater number of active sites and helps to alleviate the volume expansion during cycling, while the single-crystalline nature of the V_2O_5 nanorods facilitates fast kinetics with the merits of 1D nanoarchitectures.[299]

DOI: 10.1021/acs.chemrev.9b00405
Chem. Rev. XXXX, XXX, XXX−XXX

However, 3D architectures sometimes require the additional process(es) of reassembling individual 0, 1, and 2D NSMs, making them less cost-effective.[287]

4.2.1.2. Surface Dependence of Nanostructures. Despite the potential advantages of nanosized materials, intrinsic obstacles including their surface reactivity, agglomerations, and nonuniformity limit their use and delay their practical application in battery systems. These properties are determined by the nature of the surface, including the preferred crystal facets, surface atomic structure, and reconstruction. Therefore, redesigning the morphologies of nanosized materials can effectively suppress the limitations when adapting nanomaterials for battery systems. A few studies have demonstrated that a careful redesign of the morphologies of nanomaterials can efficiently mitigate the side reactions involved with the surface reactivity. Growth of particular surfaces in the controlled nanomorphologies may offer minimized side reactivities with electrolytes, along with optimized battery performance.[300] For example, in the case of $LiMn_2O_4$ spinel-type materials, as the Mn dissolution from the material degrades the cycle stability, an effect that is magnified when used as nanosized electrodes with larger surface areas,[251,252] Kim et al. proposed that a truncated octahedral nanomorphology of $LiMn_2O_4$ can successfully mitigate the dissolution.[301] It was noted that the Mn dissolution is dependent on the lattice orientation of the surface contacting the electrolytes, which was the most favorable at the (1 1 0) surface.[301−303] Accordingly, it was demonstrated that truncating the reactive surface in the morphology could lead to a substantial reduction of the Mn dissolution, while the cycle and rate performances are maintained for nanosized $LiMn_2O_4$.

Given the anisotropic nature of the electrode material, thermodynamic information on the different crystal facets can also be useful in tailoring nanosized electrode materials for high structural and thermal properties. For example, in the case of $LiCoO_2$, it is known that a thermal runaway, which involves oxygen release from $LiCoO_2$ lattice, poses a safety problem for elevated-temperature applications. Moreover, this problem increases drastically with nanosize $LiCoO_2$ electrodes.[304] Interestingly, the (0 0 1) facet is much more resistant toward oxygen release, while it is relatively easy to induce oxygen release on the (0 1 2) and (1 0 4) facets. The oxygen release from those facets tends to trigger local structure transitions from the original layered structure ($R\bar{3}m$) to spinel ($Fd\bar{3}m$) and rock-salt ($Fm\bar{3}m$) structures.[305] The structural transitions further propagate from the side surfaces of the crystal to the core, accompanied by further oxygen loss and thermal decomposition. This implies that understanding the oxygen release reaction of each facet can help guide attempts to minimize thermal runaway of $LiCoO_2$ by morphology design.

Regarding the aggregation or coarsening of nanoparticles at elevated temperatures,[306] a thermodynamic approach to suppress the grain growth of nanostructured polycrystals has been evidenced in a few systems.[307−309] Mayr and Bedorf rationally designed a method to mechanically stabilize Cu nanostructures by grain-boundary doping with Bi.[310] Upon doping Bi atoms within the grain boundaries of nanocrystalline Cu, molecular dynamics (MD) calculations revealed the occurrence of a locally negative grain-boundary free energy, while the overall free energy remained positive. The presence of the locally negative free energy introduced by the grain boundary doping inhibited grain growth. This implies that dopants within the grain boundaries of active electrode materials, or locally negative grain-boundary free energies within nanocrystals may offer stable long-term stability of nanoparticles against aggregation in electrochemical systems.

4.2.2. Electrode-Level Considerations. Some limitations of nanosized active electrode materials can be addressed effectively by optimizing their electrode-level engineering. For example, accelerated transition metal dissolution from the larger surface area can be mitigated by forming a physical protection layer on the electrode surface. In addition, the aggregation of nanoparticles and the large interparticle resistance can be resolved by adopting a conductive carbon architecture in the electrode.[269,311,312] The strategies discussed here address the electrode-level considerations, modifying the function/shape of individual electrode components such as the binder and conductive agent or the packing approaches, in order to alleviate the shortcomings of the nanomaterials. Some of the strategies have also been intensively investigated in other electrochemical devices such as those for energy harvesting and water splitting, thus many review papers related to this "nanostrategy" provide useful points of view.[2,3,271,313−316]

4.2.2.1. Surface Modifications for Stability. The most widely practiced solution to the side reactions induced by surface reactivity is the improvement of the electrochemical/chemical stability of the surface using coatings or formation of physical protective layers. Such surface modifications are usually implemented using either direct coating of heterogeneous materials on the active materials by specific synthetic processes[317−320] or using additives in the electrolyte to trigger the formation of special SEI layers by electrochemical processes.[321−324] Both methods have proven to be effective in increasing chemical stability by avoiding the direct exposure of the electrode surface to the electrolyte/salt. These approaches have also resulted in remarkable improvements of the electrochemical stability of postlithium-ion battery systems, such as Li/sulfur[325−327] or aqueous[328−330] rechargeable battery systems, indicating that surface modification is a universal strategy that can be applied to electrochemical systems with similar problems.

Essentially, the materials used for surface coating or modification should meet the following conditions. (i) The material and its dimensions should allow reasonably fast lithium ion and electron conductivity. Otherwise, the battery will suffer from a high overpotential, resulting in a reduced power density and poor cycle life. In addition, due to the presence of many interparticle interfaces of nanomaterials, it is crucial that the materials used for coating or encapsulation have a high electrical conductivity and provide an effective electrical connection. (ii) The surface coating material should be chemically compatible to the active materials and electrolytes used in the battery and stable in the voltage range of the cycling. (iii) It is also essential for the coating material to exhibit mechanical compatibility with the electrode materials, which undergo volume changes with de/lithiation, either by their intrinsic properties or coating/encapsulating geometry. For example, for electrodes that undergo severe volumetric expansion during cycling, it is advantageous to have an encapsulation structure with a buffer space rather than a coating directly connected to the material because permanent breakage of the coating can occur with the volume changes.[331,332] Alternatively, anchored structures can be effective in utilizing the large active surface area of nanoparticles provided that the chemical/physical stability of the

DOI: 10.1021/acs.chemrev.9b00405
Chem. Rev. XXXX, XXX, XXX−XXX

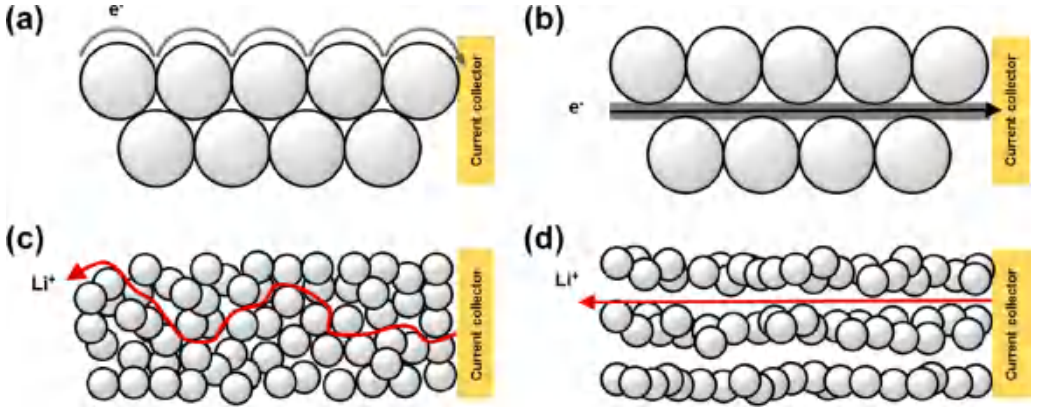

Figure 35. Schematic illustrations comparing the kinetic factors of nanoparticle-based electrodes with different structures. Electron flows in (a) carbon-coated nanoparticles and (b) an electrical-matrix-supported electrode with carbon-coated nanoparticles. The overall resistance of the electrode can be reduced by using both carbon-coating and electric wiring techniques. Guest-ion diffusion paths in (c) densely packed nanoparticles and (d) arranged nanoparticles with micropores. The diffusion of guest ions into electrodes with micropores is more advantageous.

particles is secured.[333−335] (iv) Finally, industrial aspects such as cost competitiveness, eco-friendliness, and large-scale synthesizability should be satisfied.

The most widely used materials for the surface modification of nanoparticles include carbon-based materials (amorphous carbon, graphitic carbon, graphene[333,336−339]), 2D materials (boron-nitride, phosphorene[340,341]), and inorganic materials (Al_2O_3, MgO, ZrO_2, or glassy materials[45,317,342−346]). Carbon materials have been widely used in both cathode and anode materials because of their low cost, high electrical conductivity, and good mechanical properties. The distinct properties of different carbon species and the availability of processing techniques have made carbon materials one of the most suitable coating/encapsulating agents for nanosized electrode materials.[2,347] Recently, 2D materials were also investigated as surface coating/encapsulation materials, as the physical and electrical properties of 2D materials can be engineered by modulating the number of layers.[348−351] Although only a few studies have demonstrated the application of 2D materials (except for graphene) to enhance the stability of lithium metal or the electrochemical properties of anode materials.[341,350,352] Its applicability is expected to be expanded in the future.

While surface modification can offer a viable way to reduce side reactions, it also compromises some of the beneficial nanophenomena, particularly those relying on the surface electrochemistry. The charge storage mechanisms at the interface or in pseudocapacitive materials can be passivated by the presence of the coating materials. Thus, this approach cannot be universally applied and their use is limited to certain classes of nanomaterials. Moreover, the additional surface modification process may not be cost-effective, and the actual cost may also increase depending on processes required to achieve a conformal coating on wide surfaces of the nanomaterials. Solution processes or chemical vapor deposition (CVD) may alternatively be used to increase the coating uniformity, but the increased cost resulting from the use of certain solvents or equipment is unavoidable. Conventional mechanothermal treatment methods can provide a relatively inexpensive process; however, it is challenging to achieve high uniformity throughout the entire nanoparticle sample.

4.2.2.2. Maximizing Kinetics within the Electrode. The electrochemical hysteresis of a nanomaterial is caused not only by thermodynamic effects but also kinetic factors originating from the nanofeatures of the material. In the ideal case, a round-trip galvanostatic curve with a high efficiency should be obtained for electrodes containing nanomaterials because the active surface area is large and the path through which lithium ions diffuse is relatively short. However, it is sometimes difficult to fully exploit the advantages of fast kinetics in nanosized electrodes because of practical problems, such as the electrical connection of each nanoparticle or the increase of interfacial resistance.[4,353] In addition, the structural complexity of the nanostructure, with limited pore connectivity, can severely elongate the diffusion paths of guest ions and impede charge transfer.[110,354,355] Thus, the electrochemical response of some nanoparticles is difficult to achieve and eventually leads to deterioration of the electrochemical properties, with higher hysteresis, lower power density, or reduced cycle retention.

Generally, to enhance the electrical connectivity among large numbers of nanoparticles, coating each particle with conductive materials could offer higher contact probability and reduced interfacial resistance. Remarkably improved electrochemical performances achieved using carbon or conductive materials have been documented in many coating studies, strongly supporting the basis of the coating effect.[312,318,356,357] While coating clearly alleviates the issue of electric connection for individual particles, it still presents challenges regarding elongated electrical paths through particle-to-particle surfaces, as schematically illustrated in Figure 35a,b. The electron path along the surface of nanoparticles is inordinately longer than a straight path to the current collector (Figure 35a,b), which causes a greater IR drop of the cells.[3] In this respect, it is necessary to shorten the overall electronic path in the electrode using conductive matrix agents, such as CNTs, graphene oxide, or 2D materials.[358−361] Other approaches include regulating the shape of the current collector or growing the nanomaterial directly on the current collector.[36,362−364] Through these approaches using nano-architectures, the challenges associated with the electrical connectivity can be efficiently resolved.

Nanomaterials generally exhibit low tap densities, which necessitates the use of thick electrodes to gain the desirable energy density. If the nanoparticles are too densely packed on the electrode, the electrode only contains nanoscale pores inside, and eventually some particles have limited access to the electrolyte, as schematically shown in Figure 35c. Thus, the overall diffusion path of ions becomes longer than that of an electrode possessing micropores, resulting in limited electro-

DOI: 10.1021/acs.chemrev.9b00405
Chem. Rev. XXXX, XXX, XXX−XXX

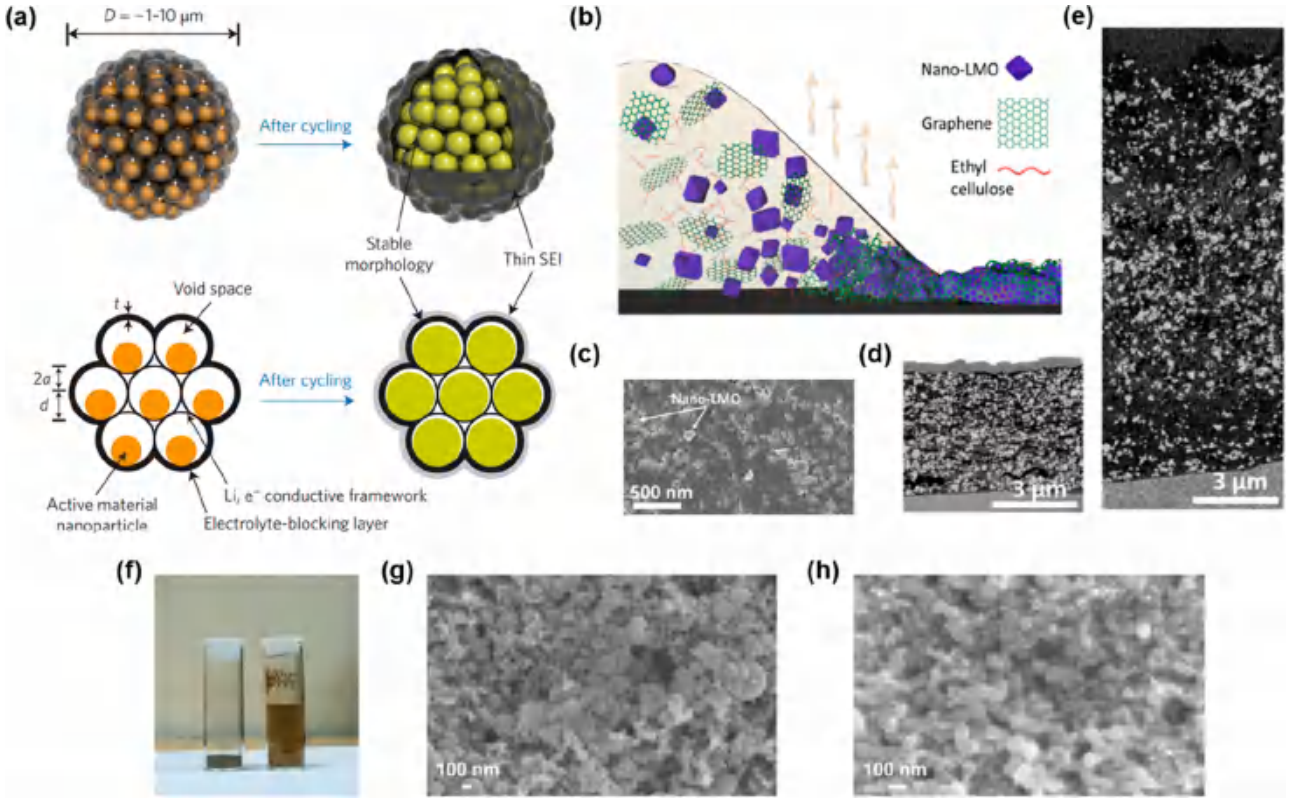

Figure 36. Various strategies for obtaining high-tap-density nanomaterials. (a) Schematic illustration of secondary particle design using Si nanoparticles.[269] Reproduced with permission of ref 269. Copyright 2014 Springer Nature. (b) Graphene/ethyl cellulose-supported electrode with high volumetric energy density. (c) Graphene flakes in the electrode. This makes the electrode more densely packed, resulting in a reduced electrode thickness (d) relative to that of an electrode prepared using the normal fabrication process (e).[311] Reproduced with permission of ref 311. Copyright 2017 American Chemical Society. (f) High-tap density Si nanoparticle obtained using a new binder (left) and pristine Si nanoparticles (right). SEM images showing that the particles are more densely packed when using a PPyMAA binder (g) compared to a controlled powder (h).[376] Reproduced with permission of ref 376. Copyright 2015 American Chemical Society.

chemical kinetics.[365] The ionic accessibility can be improved to some extent if the nanoparticles are well ordered using chemical or mechanical processes. However, the volumetric energy density and loading density should be simultaneously considered when using the dispersion strategy (Figure 35d). In this respect, researchers have attempted to assemble hierarchical structures wherein the nanomaterials are arranged consistently, which can simultaneously ensure the microporosity and higher packing density of the material. Some examples include the arrangement of nanorods in a row on current collectors[363,366] or the fabrication of secondary particles with internal alignment.[269,367] Studies that adopted such strategies successfully demonstrated higher electrochemical properties and volumetric energy densities than those of randomly distributed electrode structure.[3,274] The direct growth or distribution of nanoparticles on arranged conductive matrixes, such as graphene oxide or CNTs, have been shown to improve both ionic and electronic percolating paths.[368,369]

The optimization of the kinetic factors of the electrode can improve the uniformity of the electrochemical reaction, which in turn has a positive effect on the power density, charge/discharge efficiency, and cycle life of nanomaterials. However, it is worth noting that these approaches often result in the need for excessive conducting agent or matrix to cover the large nanoparticle surfaces, decreasing the practical specific and volumetric energy densities. Thus, the development of an advanced electrode fabrication method that meets the above conditions is necessary for viable commercialization.

4.2.2.3. Materials Packing toward High Energy Density. Recent studies have shown that the low tap density drawback of nanomaterials can be effectively overcome through the advanced process of stacking nanoparticles and fabricating electrodes. One of the main approaches includes the fabrication of the secondary structure by assembling nanoscale primary particles and forming microsized secondary particles.[370−374] A much higher tap density can be attained than in the original state without compensating for the specific energy density. Liu et al. suggested a hierarchically structured Si nanoparticle using microemulsion droplets.[269] The microscale secondary particles, which resembled a pomegranate, were designed such that each nanoparticle was separately encapsulated by a thin carbon layer with void space for volumetric change (Figure 36a). The coated nanoparticles were assembled into secondary particles encapsulated by a thick carbon layer, which prevented further mechanical isolation of the primary particles. With the pomegranate-like structure, the electrode density could be dramatically enhanced by 250% from 0.15 to 0.53 g/cm^3. The assembly of the nanosized primary particles into secondary particles was also practiced in the preparation of the nanoscale cathode materials. Wen et al. fabricated microsized secondary particles with $LiFePO_4$ nanoparticles using a spray-assisted method, achieving an electrode loading density of 2.6 g/cm^2, which was

DOI: 10.1021/acs.chemrev.9b00405
Chem. Rev. XXXX, XXX, XXX−XXX

approximately 40% higher than that of electrodes produced using the conventional casting method.[370] The electrodes were able to attain volumetric energy densities of up to 70% of the theoretical value of $LiFePO_4$.

Improvement of the low tap density of nanomaterials can also be achieved with the help of other electrode components.[311,339,375] Chen et al. was able to increase the volumetric energy density of nano-LMO using graphene nanoflakes and an ethylcellulose matrix. They used a graphene/ethylcellulose complex to form a slurry mixture with nano-LMO particles and then heated the mixture to remove the ethylcellulose (see the schematic illustration in Figure 36b).[311] During the decomposition of the ethylcellulose, the graphene flakes were strongly compressed against each other, forming a thin and binder-free electrode film with increased packing density, as shown in Figure 36c. The electrode thickness was reduced to less than 40% (Figure 36d) and the volumetric energy density was 30% higher than a conventional electrode (Figure 36e). Binders with strong adhesion forces can also be employed to effectively increase the tap density.[376] A new binder, poly 1-pyrenemethyl methacrylate-co-methacrylic acid (PPyMAA), provided a tap density of 0.5 g/cm^3 using ∼200 nm of nanosilicon particles (Figure 36f), with a first cycle efficiency of 82%. Parts g and h of Figure 36 show the nanosized Si particle with and without PPyMAA binder, respectively. As observed in the SEM images, the particles using the PPyMAA binder were clustered more densely and formed a network. It was suggested that the MAA structure incorporated in the PPyMAA induces strong covalent bonding with the Si particle surface, which minimizes the exposed surface area with the high tap density.

The low tap density of nanoparticles is a problem that can be surmounted by regulating the stacking of nanoparticles at the electrode level. However, the process used here needs to be scaled up to the commercialization level and must satisfy cost-effectiveness requirements at the same time. Moreover, the development of an electrode fabrication process while accounting for the surface characteristics of the nanomaterial will be critical in overcoming low tap density problems.

4.2.2.4. Multifunctional Binders for Nanomaterials. Poly vinylidene difluoride (PVDF), poly(acrylic acid) (PAA), and carboxymethyl cellulose (CMC), which are typical binders for commercialized batteries, do not have electrochemical activity in the practical voltage range, while the electrode generally contains a binder with a mass ratio of 1−5 wt %. Nanosized electrode materials generally require a large amount of conductive agent and exhibit larger volumes by weight, thus needing more binding agents than bulk materials. There have been attempts to address this issue of nanosized materials by imposing multiple functionalities on the binders.[377,378] Wu et al. redesigned the polymeric chain of the binder to retain electrical conductivity in order to improve the energy density of nanomaterials.[379] Chain tuning of a polymeric binder could also improve the ionic conductivity of the electrode in addition to its electrical conductivity. Facile Li-ion transport was possible along the side chain, which increases the polarity to enable better uptake of the electrolyte. Studies have also reported the improvement of the cycle life even with repeated volume changes in the electrode by using a binder with intrinsic electrical conductivity, thereby ensuring the presence of electrical networks in the electrode.[380,381]

There have also been attempts to accommodate the volume changes of nanosized electrode materials by fixing the nanoparticles to a 3D scaffold polymer binder using porous binder structures.[382] Employing a binder with a 3D interpenetrated network offered a better cycling stability because of its capability of reversible deformation upon volume change.[383] Recently, a new type of binder was reported that enables ring sliding based on a principle similar to the pulley stress-release mechanism for mitigating the volume expansion of the Si anode.[384] As a result, the pulverized particles in the electrodes could be reintegrated to prevent the loss of active materials as well as to prevent uncontrolled growth of SEI layers. Hence, it was possible to maintain a stable cycle life even in commercial-level areal capacities. This report implies that the molecular design of the binder can be an important part of the electrode redesign process, encompassing nanosized electrode materials.

4.2.3. Advanced New Techniques for Exploring Nanochemistry. Over the last two decades, the direct observation of micro/nanostructure changes upon electrochemical reactions has been actively pursued in the field of battery research; consequently, the understanding of battery chemistry has greatly progressed owing to these pioneering efforts.[46,105,385−387] Today, real-time observation at the nanoscale is becoming more important than ever: nanotechnology is playing an increasing role in rechargeable battery systems as researchers have begun to realize that electrochemical reactions at the nanoscale are far from thermodynamic equilibrium.[290,388,389] Reflecting these issues, recent advances in observation technology have led to new insights into the nanoscience of battery systems. In this section, we discuss the challenges of technology for the observation of nanosized electrode chemistry and then introduce advanced new tools to characterize this chemistry for rechargeable batteries.

Generally, these fields of study have three major challenges:

(i) Realization of actual battery conditions. To accurately monitor the behavior of nanomaterials, the observation should be implemented under the actual electrochemical conditions or, at least, in corresponding environments. However, battery systems used in observation equipment are significantly limited by the characteristics of the equipment. For example, the use of commercialized organic electrolytes is not compatible with vacuum equipment because of their high vapor pressures.[390,391] In addition, light/beam sources with high energies often cause severe electrolyte decomposition, damage to the active materials, and local heating, leading to an increase of the complexity of realizing battery conditions.[392] Thus, many studies have used ionic liquids, solid electrolytes with physical contacts, or encapsulated systems for better stability under the measuring conditions.[393,394] Although these alternative methods can facilitate understanding of the nanosized active materials, it is difficult to fully ensure the realistic behavior of active materials in practical cells. Moreover, it is necessary to manufacture single-particle or monoparticle-layer dispersed electrodes to achieve accurate observations; however, this step also presents another large challenge because of the fabrication of the nanocircuit and its control.

(ii) High spatial resolution. The electrochemical reactions at the nanoscale should be investigated with high spatial resolution with specific reaction information, such as subtle lattice changes or changes in the oxidation state of the redox center, occurred simultaneously. In general, apparatus using X-rays or electrons have theoretical spatial limit resolutions determined by the energy of the source, with a proportional relationship. However, the observations of real-time electro-

DOI: 10.1021/acs.chemrev.9b00405
Chem. Rev. XXXX, XXX, XXX−XXX

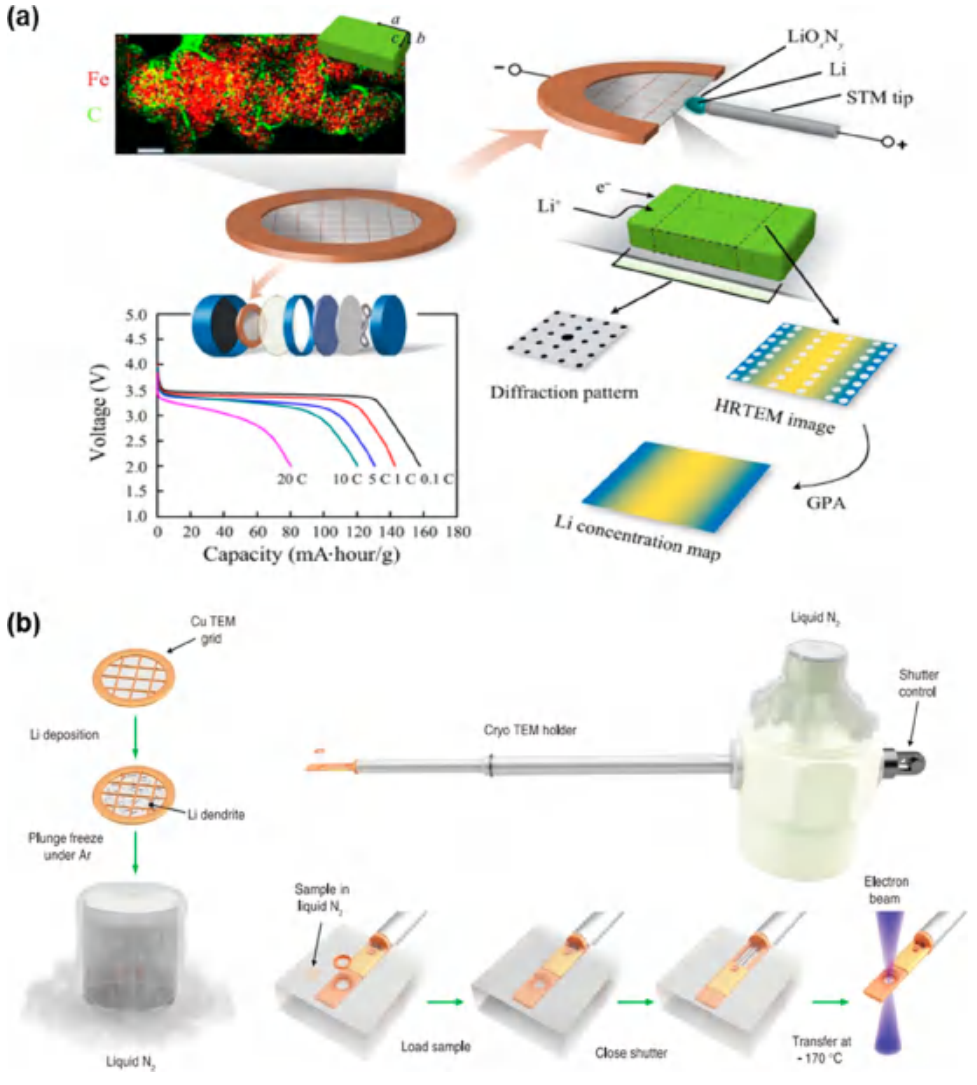

Figure 37. Schematic illustration of advanced new TEM techniques for nanomaterials. (a) GPA analysis using high-resolution TEM and an in situ electrochemical system, which can provide more accurate lattice images at the nanoscale.[395] Reproduced with permission of ref 395. Copyright 2018 American Association for the Advancement of Science. (b) Overall process for cryo-TEM measurement. Continuous cooling with liquid nitrogen effectively alleviates beam damage and enables the observation of soft materials.[398] Reproduced with permission of ref 398. Copyright 2017 American Association for the Advancement of Science.

chemical reactions are limited at their theoretical resolutions because of the complexity and sensitivity of battery systems.[392] Therefore, it is necessary to develop devices, including a detector or calibration tools, to increase the resolution or to use an advanced algorithm to interpret the response information in mild energy ranges.

(iii) Time-resolved information. The electrochemical reactions of nanoparticles often occur nonuniformly in each area, even though the overall cell capacity is proportional to the time and applied voltage/current.[389,395] Thus, a certain local area is most likely to react rigorously under high current density. Moreover, nanosized electrode materials exhibit significantly increased rate capabilities and fast relaxation behavior to reach the equilibrium state. Thus, collecting information over a very short time period is essential to further identify the rapid kinetics of nanomaterials. However, large time resolutions can cause significant difficulties in the precise interpretation of data because of a higher signal-to-noise level and relatively low intensity counts. Therefore, similar to the approaches used to overcome spatial resolution issues, the development of devices or algorithms to achieve high time resolution with qualified data is necessary.

These equipment and limitations are also discussed in depth in other review articles.[396,397] From here, the most recent major achievements in addressing the challenges outlined above, and promoting a new understanding of the electrochemical properties of nanomaterials, are introduced.

4.2.3.1. Advanced TEM Techniques for High Resolution. TEM is widely used for investigating atomic arrangements with high-resolution imaging up to the Angstrøm scale. However, some battery materials, such as Li metal and electrolytes, are highly vulnerable to electron-beam irradiation, making TEM study while maintaining the native state of the subject a large challenge. Moreover, the inherent local heating also causes serious damage or vibration in in situ electrochemical systems, creating further difficulties for the direct observation of battery operations. However, recent technological advances have significantly mitigated the traditional vulnerabilities of TEM.

High-resolution lattice imaging with advanced geometric phase analysis (GPA) has revealed a local Li concentration

DOI: 10.1021/acs.chemrev.9b00405
Chem. Rev. XXXX, XXX, XXX−XXX

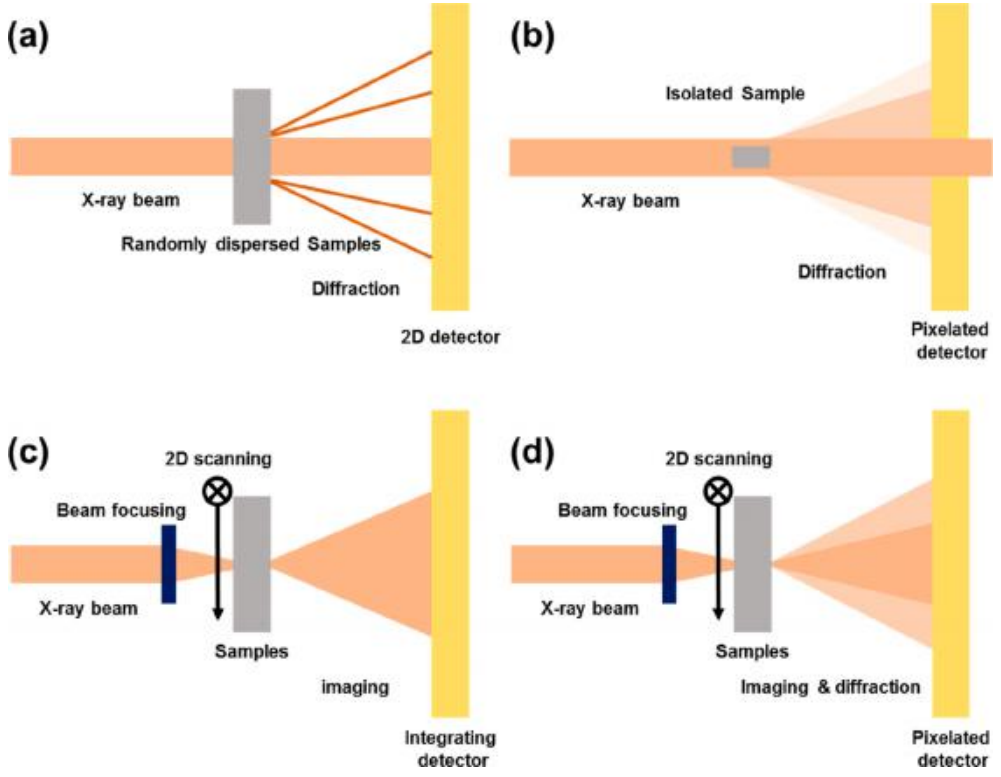

Figure 38. Schematic illustration of the operation of various X-ray-based equipment. (a) X-ray powder diffraction, (b) coherent diffractive imaging, (c) scanning transmission X-ray microscopy, and (d) ptychography technology.

reversal phenomenon during galvanostatic cycling.[395] The advanced algorithm used in GPA results in high time-resolved and position-resolved lattice images from high-resolution (HR)-TEM, enabling the investigation of sub-Angstrøm-scale lattice changes at the single-nanoparticle level using an in situ electrochemical tool (see Figure 37a). The authors were able to visualize the local lithium concentration change in areas as small as several nanometers (3 nm × 3 nm) using electron diffraction, revealing inhomogeneous intercalation in a single particle of nanosized $LiFePO_4$. In contrast to the generally accepted understanding of monotonic Li concentration changes, it was demonstrated that a reversal of the local Li concentration occurs in nanosized domains because of their different chemical potential curves depending on the local domains.

Moreover, the so-called cryotechnique significantly mitigates the effects of electron-beam irradiation of Li metals, allowing the native state of Li dendrites and its SEI layers to be observed even at a high acceleration voltage of 300 kV.[398] The SEI layer and Li metal are sensitive to the electron beam because of their weak atomic bonding and low melting points. However, as shown in Figure 37b, continuous liquid-nitrogen cooling during the entire sample preparation and measurement process greatly alleviates the decomposition of these soft materials. It was revealed that the single dendritic growth of Li metal in carbonate-based electrolytes has preferred facets with certain directions. It has also been demonstrated that the nanostructure of the SEI layer can be altered by using additives in the electrolytes. Whereas the standard carbonate-based electrolyte ethylene carbonate−dimethyl carbonate (EC−DEC) forms randomly distributed inorganic crystal domains in the amorphous matrix, a more ordered multilayer structure forms when 10 vol % fluoroethylene carbonate (FEC) was added to the electrolyte.

4.2.3.2. Superior Time-Resolved in Operando XRD. XRD is a typical diffraction-detecting technique used to investigate phase evolution using the Bragg diffraction fingerprints of crystalline materials.[399] This technique can provide quantitative microstructural information such as the single-crystal grain size or internal strain. Conventional XRD measurements provide a pattern for thermodynamically stable states because the electrode is measured in a relaxed state. In contrast, the patterns measured using in situ or in operando electrochemical systems can represent the nonequilibrium state of active materials, providing more comprehensive insight into the kinetics of batteries. However, the relatively long measurement time of conventional XRD, from a few minutes to hours, is insufficient to gather accurate information regarding dynamic states because of the rapid kinetics of nanomaterials. Therefore, synchrotron-based in-operando XRD with a 2D detector (as shown in the schematic of Figure 38a), which can provide higher diffraction intensity even for short measurement times because of the use of high-energy X-rays, plays an important role in dynamics studies of nanosized electrode materials.

Using in operando synchrotron XRD, Liu et al. observed metastable phases spanning the range of $0 < x < 1$ in Li_xFePO_4 (~190 nm).[46] They successfully measured the phase transition behavior at 5, 10, and 20 °C using a 2D diffraction detector with a data collection time of 3 s for each pattern. The time scale corresponds to 0.004Li, 0.008Li, and 0.017Li per formula unit change of $LiFePO_4$, respectively. They observed that the diffraction patterns broadened toward higher angles under higher current density and concluded that this feature originated from capturing the metastable phases between two

DOI: 10.1021/acs.chemrev.9b00405
Chem. Rev. XXXX, XXX, XXX−XXX

end members of phases rather than nucleation of the new phases. They analyzed the measured XRD patterns by fitting and compared them with XRD simulation results with multilithium composition phases. It was possible to analyze the phase distribution with high accuracy because the synchrotron beam has only a single peak for each Bragg position (unlike conventional XRD using a metal emission source that generates Kα1 and Kα2 peaks). This work represents important progress that maximizes the time and phase resolution and thus provides an in-depth understanding of the nonequilibrium behavior of nanomaterials.

4.2.3.3. X-ray Diffraction for Coherent Imaging. The coherence of X-rays from a synchrotron source is one of the key characteristics that allows structural information to be analyzed more accurately from diffractive information. Coherent diffractive imaging (CDI) uses a lens-less microscope taking advantage of the coherence of the beam and phase shifts in the specimen. Figure 38b presents a schematic illustration of CDI. The plane detector collects the intensity of the diffraction patterns containing large scattered vectors from the isolated single particle. If the collected information is converted into real space, one can obtain a high-resolution image of nanosized specimens. Moreover, when one measures the interference near the Bragg diffractive position of the sample with rocking in a small angle range, the 3D electron density images in real space can be rendered using sophisticated phase retrieval algorithms. The image has a relatively low resolution (~10 nm); however, it can provide a variety of structural information for nanomaterials from the diffractive properties, such as the elastic properties of or defect movements in the material.[400] Recently, these advanced Bragg CDI techniques have been combined with an in situ electrochemical system, enabling observations to be made of the inside of a single nanoparticle by focusing the X-ray beam.

Ulvestad et al. revealed three-dimensional strain evolution in a single $LiNi_{0.5}Mn_{1.5}O_4$ nanoparticle under in operando conditions.[401] They observed the stripe morphologies and coherency strain using the Bragg CDI technique and showed that the stripe formation required a critical size of above 50 nm. Moreover, the dependence of strain on the direction of charge/discharge was elucidated by the elastic energy landscape with femtojoule precision, directly showing hysteresis in a single nanoparticle. They also could track a single edge dislocation in a single $LiNi_{0.5}Mn_{1.5}O_4$ nanoparticle under electrochemical cycling.[402] The negative Poisson ratio observed by the authors could explain the phenomenon by which $LiNi_{0.5}Mn_{1.5}O_4$ does not undergo serious structural collapse or oxygen evolution even at high voltages. Moreover, it was visualized that the dislocation served as a nucleation starting point during phase transition, confirming theoretical expectations.[403] Coherent imaging technology, introduced relatively recently, can be used to directly investigate the nanomechanical behavior or defect characteristics of a single nanoparticle in real time as well as in 3D maps. Thus, it is believed that this imaging technology will be widely used to explore nanomaterials in the future.

4.2.3.4. Scanning Transmission X-ray Microscopy. Another imaging technology providing 2D maps is scanning transmission X-ray microscopy (STXM). This is a microscopy technique that scans a sample, as depicted in Figure 38c, with a nanofocused X-ray beam to obtain images and bring to light chemical information on reactions, such as X-ray fluorescence and the yield of electron emission or diffraction. By using a focused beam to scan a sample, synchrotron-based STXM can provide a deeper penetration depth and less damage to the material than an electron microscope, while having a higher resolution than an optical microscope.[400,404] The scanning method has many strengths for analyzing materials; however, there are limitations associated with the use of STXM. The focused beam size determines the resolution of the microscope; thus, advanced beam focusing techniques down to the nanoscale are required. In addition, it can take a long time to examine a large field of view, making it difficult to examine a large sample under in situ conditions. Rapid recent technological developments have led to focused beam sizes of less than 10 nm, and the time needed to acquire images has been gradually decreasing.[396] Through these efforts, STXM is becoming a suitable tool for observation of electrode materials without serious damage and with high spatial resolution. However, the decomposition and evaporation of electrolytes resulting from heating by the focused beam, although much less than with other techniques, still causes difficulties in introducing an in situ electrochemical system into STXM. Li et al. overcame these limitations by handling the sample rationally.[385] As soon as the cell was stopped, the electrolyte-containing salt was rapidly removed to eliminate the relaxation path in the electrode. Thus, the authors were able to take a frozen picture of the dynamic situation at the electrode using STXM. In another report, an electrolyte circulation system was installed in an in situ STXM system to effectively mitigate damage and vaporization of the electrolyte, and it was possible to directly observe the real-time behavior of a $LiFePO_4$ electrode.[389]

4.2.3.5. X-ray Ptychography. Ptychography technology is a next-generation imaging technology that combines the advantages of both STXM and CDI technologies. This revolutionary imaging tool simultaneously resolves the issues of the limited resolution of STXM and the selectivity on the objective of CDI.[400] The technique also uses focused, coherent X-rays, and the beam scans the specimen using a 2D axis. Thanks to the coherent beam, coherent diffractive patterns are obtained from the lattice, and this information is partially overlapped with the illumination imaging of the specimen (see Figure 38d). When phase-retrieval algorithms deconvolute the overlapped information from Fourier space, one can obtain high-resolution images in real space. A more detailed algorithm for ptychography imaging is described elsewhere.[400,405] X-ray ptychography can read chemical information changes with high resolution; thus, it is expected to play an important role in studying the electrochemical behavior of nanomaterials.

The relationship between the amount of carbon present and reaction order depending on particle size has been revealed by ptychography. Using $LiFePO_4$ particles distributed from 50 to 500 nm, Li et al. observed that if the amount of carbon in the electrode differs from 20 wt % to 5 wt %, electrochemical reactions occurred first near the carbon, regardless of the particle size. However, carbon-rich electrodes began to react from small $LiFePO_4$ particles because of their increased surface-to-volume ratios. This observation indicates that the electrochemical reaction of electrodes with nanoparticles is prioritized by electrical connectivity.[406] Moreover, ptychography has recently been used to obtain 3D maps of particle dispersion and chemical composition change in combination with tomography. Yu et al. successfully constructed a 3D map of a $LiFePO_4$ electrode at 50% SoC. With a resolution of 11 nm, the 3D map provided a comprehensive view of the phase

DOI: 10.1021/acs.chemrev.9b00405
Chem. Rev. XXXX, XXX, XXX−XXX

boundaries within a single particle as well as changes in phase transitions depending on the size and location of the particles.[407] Ptychography technology is expected to be combined with other imaging equipment as well as in situ electrochemical systems, providing an in-depth and comprehensive view of battery reactions on the nanoscale.

4.2.3.6. Advanced Nanosynthesis Techniques. Rationally designed nanostructures can open the possibility of identifying specific material properties, however, the shape control of nanomaterials is not a trivial task. The formation of nanoshapes is determined by the thermodynamic free energy balance between the bulk and surface under the applied conditions. Because of the large surface area of nanomaterials, they can be transformed into various shapes depending on the energy state of the surface. Most conventionally, hydrothermal[280,354] and solvothermal synthesis,[296,408] and sol−gel methods,[147,283] which apply variations of the surface chemical environment using certain solvents or additives, have been extensively employed for the synthesis of nanomaterials. Using these methods, a variety of nanostructures have been fabricated for common electrode materials, such as $LiCoO_2$, $LiFePO_4$, Si, and SiO_2, from 0D to 3D shapes (extensive information can be found in other review articles[409−412]). Depending on the type of solvent or additive, post-treatment processes have to be conducted to remove residual chemicals.

Physical vapor deposition (PVD),[413,414] chemical vapor deposition (CVD),[415,416] atomic layer deposition (ALD),[417,418] and pulsed laser deposition (PLD)[419,420] have been widely used both in the coating of active materials[421−423] and in producing film-type active materials. While these techniques are generally regarded as unsuitable for the mass production of battery materials, they can provide model film-type nanoscale geometries for the theoretical studies of nanophenomena. Moreover, the sequential deposition process can realize ideal interfaces between certain combinations of battery components, such as the active and solid-electrolyte or active and carbon additive interfaces, which can be helpful for investigating the interface chemistry at the nanoscale.[424−426] In particular, recent studies have been undertaken on the interfaces between solid electrolytes and active materials using well-defined model systems derived from this technique.[427−429]

Solution process exfoliation[430,431] and high-energy milling techniques,[10,15] which are typical top-down approaches, physically reduce the size of the original materials down to the nanoscale. The solution exfoliation process is often used in the fabrication of various 2D type materials, exfoliating layers from bulk states such as graphite or MoS_2 into single or groups of a few layers with large crystalline basal planes. The yield of solution exfoliation processes is typically low, however, recent research has led to some improvements.[432] High-energy ball milling, which involves strong collisions and breaks down the materials, offers a facile and simple route for the synthesis of nanocomposites or nanophases while preserving the characteristics of the parent materials. This technique allows the exploration of new metastable chemistry beyond that of the bulk materials,[10,15,144,154] however, the undefined defects of the surface and uneven morphologies produced often present major obstacles to these studies.

5. CONCLUDING REMARKS

Over the last two decades, nanostrategies have been extensively employed as extrinsic solutions for overcoming the physical and chemical limitations of electrode materials in battery reactions. This work has offered improved electrochemical performance and rich chemistry based on unprecedented phenomena driven by altered kinetics and thermodynamics. Furthermore, this new avenue of research is not only creating breakthroughs in rechargeable batteries and but is also expanding our understanding of materials. Herein we have reviewed general nanoscale phenomena in electrochemical reactions and overall battery performance in terms of kinetics, thermodynamics, and mechanics. Nanosizing accelerates reaction kinetics by shortening the diffusion length and widening the reaction-active area but also changes the thermodynamics and mechanical properties of the materials. The increased surface ratio leads to variation of the free energy of materials, changing the chemical potential of de/inserting ions sufficiently for manipulation of the voltage, reaction pathway, and even mechanical properties regarding the phase evolution. The increased impact of surface and stress on the reaction mechanism has provided new possibilities for controlling the reaction mechanism by modulating the size of the electrode particles, ultimately offering opportunities to overcome the limitations of current LIB chemistry. Several new strategies for designing electrode materials have been introduced based on nanoscale phenomena. Decoupled electron and ion storage in nanocomposite electrodes and pseudocapacitors has provided new insights for the exploration of electrode materials beyond conventional intercalation-based chemistry. In addition, the discovery of synthetic routes based on nonequilibrium thermodynamics and new chemical principles has spurred research into electrode materials with metastable states.

Finally, the inherent limitations of materials due to their surface reactivity are discussed, namely side reactions, particle aggregation, and chemical nonuniformity. The high surface-area-to-volume ratio of nanomaterials not only has a positive effect on capacitive electrochemical reactions in terms of kinetics but also causes undesired side reactions due to exposure of unstable surfaces to the external environment. Going one step further, general strategies to overcome these nanolimitations were introduced, along with state-of-the-art analytical approaches that enable in-depth understanding of nanoscale phenomena. The nanosizing strategy is a holey grail for LIBs in that it entails not only the opportunity to access rich chemistry but also is accompanied by formidable problems that must be solved before its wider application can be realized. We believe that this review can provide fresh insights into nanoscale phenomena and act as a guide for future research.

AUTHOR INFORMATION

Corresponding Author

*E-mail: matlgen1@snu.ac.kr.

ORCID

Kisuk Kang: 0000-0002-8696-1886

Author Contributions

‖These authors contributed equally to this work

Notes

The authors declare no competing financial interest.

Biographies

Sung-Kyun Jung received his Ph.D. degree in 2018 from the Department of Materials Science and Engineering of Seoul National

DOI: 10.1021/acs.chemrev.9b00405
Chem. Rev. XXXX, XXX, XXX−XXX

University. His research mainly focused on the design of nanocomposite cathode materials consisting of mixtures of lithium compounds and transition metal compounds. He is currently a staff researcher in the Samsung Advanced Institute of Technology.

Insang Hwang received a B.Sc. degree (2013) in Materials Science and Engineering from Seoul National University. He is currently a Ph.D. candidate in the Department of Materials Science and Engineering of Seoul National University. His focus is on developing high capacity cathode materials for next-generation Na and K batteries using nanocomposites of alkali ion compounds and transition metal compounds.

Donghee Chang received her Ph.D. in Materials Science Engineering from the University of Michigan in 2015 and worked as a postdoctoral researcher at University of California, Santa Barbara. She then moved to Seoul National University, supported by the Korea Research Fellowship program (KRF) as a postdoctoral researcher. Her research interests are understanding and predicting the thermodynamic, kinetic, and mechanical properties of various electrode and solid electrolyte materials for Li- and Na-ion batteries using first-principles calculations.

Kyu-Young Park received his Ph.D. degree in 2016 from the Department of Materials Science and Engineering of Seoul National University. Afterward, he worked at the Research Institute of Advanced Materials (RIAM) as a postdoctoral researcher until 2018. He is currently working at Northwestern University as a postdoctoral researcher. He has focused on the understanding of phase transitions and defect structures of electrode materials for rechargeable batteries using a combination of neutron and synchrotron techniques.

Sung Joo Kim received his Ph.D. degree from the Department of Materials Science and Engineering of the University of Michigan in 2015 and then worked as a postdoctoral researcher at the Korea Advanced Institute of Science & Technology (KAIST) until 2017. He then moved to Seoul National University and is currently working as a postdoctoral researcher. His research interest includes understanding reaction mechanisms of various electrode systems for rechargeable batteries using in situ transmission electron microscopy.

Won Mo Seong obtained his Ph.D. degree in materials science and engineering from Seoul National University in 2019. He is currently working as a postdoctoral researcher at the Research Institute of Advanced Materials (RIAM), Seoul National University. His research is mainly focused on understanding interfacial behavior between electrodes and electrolytes in rechargeable batteries as well as developing electrode materials for high-energy-density batteries.

Donggun Eum received his B.S. degree in energy engineering from Hanyang University in 2017. He is currently a Ph.D. candidate in the Department of Materials Science and Engineering of Seoul National University. His research is mainly focused on the design of new lithium-rich layered oxides and the elucidation of anionic redox mechanisms in lithium-ion batteries.

Jooha Park received his B.Sc. degree in materials science and engineering from Seoul National University in 2017. He is currently working as a Ph.D. student in Prof. Kang's group in the Department of Materials Science and Engineering, Seoul National University. His research interests are focused on graphite intercalation compounds for energy storage systems.

Byunghoon Kim received a B.Sc. degree (2016) from the Department of Materials Science and Engineering of Seoul National University and is now pursing his Ph.D. degree in the same department. His research interests lie in the study of layered materials for next-generation batteries and electrocatalyst materials for water electrolysis using computational tools such as first-principles calculations and molecular dynamics simulations.

Jaehoon Heo received his B.Sc. degree in materials science and engineering from Seoul National University in 2018. He is currently a Ph.D. candidate in Prof. Kang's group in the Department of Materials Science and Engineering, Seoul National University. His research is focused on nanosized materials for energy storage systems.

Jihyeon Kim received her B.Sc. degree in materials science and engineering from Seoul National University in 2017 and is a Ph.D. candidate under the supervision of Prof. Kang in the Department of Materials Science and Engineering, Seoul National University. Her research interests are focused on organic electrode materials for energy storage systems.

Kisuk Kang is a Professor of materials science and engineering at Seoul National University (SNU), where he received his B.Sc. degree. He completed his Ph.D. and postdoctoral studies at the Massachusetts Institute of Technology. He was a professor at the Korea Advanced Institute of Science and Technology from 2008 to 2011, before moving to SNU. Since 2013, he has been a tenured professor at SNU. His research laboratory focuses on the development of new materials for batteries, including state-of-the-art lithium ion batteries and beyond and electrocatalysts using a combination of experiments and ab initio calculations. He is currently a director of the Center for Materials Discovery for Batteries and the Samsung SDI-SNU Rechargeable Battery Center. He is also serving as Associate Dean (Research) of the College of Engineering at SNU. His published works in this field have been cited more than 24000 times, and he was selected as a Highly Cited Researcher in 2018 by Clarivate Analytics. He was a recipient of several awards, such as the Energy and Environmental Science Lectureship Award from the Royal Society of Chemistry, United Kingdom (2012), the Science Patriots Award from the Ministry of Science, Korea (2017), Scientist of the Month from the Ministry of Science, Korea (2017), and was selected as one of the 100 leaders in Technology by the National Academy of Engineering of Korea (2017).

ACKNOWLEDGMENTS

This work was supported by IBS-R006-A2 and Samsung Research Funding & Incubation Center of Samsung Electronics under project no. SRFC-TA1403-52. This work was also supported by the Korea Research Fellowship Program through the National Research Foundation of Korea (NRF) funded by the Ministry of Science and ICT under KRF grant no. 2016H1D3A1908716. This work was supported by the National Research Foundation of Korea (NRF) grant funded by the Korea government (MSIP) (no. 2018R1A2A1A05079249). This work was also supported by Creative Materials Discovery Program through the National Research Foundation of Korea (NRF) funded by the Ministry of Science, ICT, and Future Planning (NRF-2017M3D1A1039553).

REFERENCES

(1) Lee, K. T.; Cho, J. Roles of Nanosize in Lithium Reactive Nanomaterials for Lithium Ion Batteries. Nano Today 2011, 6, 28−41.
(2) Goriparti, S.; Miele, E.; De Angelis, F.; Di Fabrizio, E.; Proietti Zaccaria, R.; Capiglia, C. Review on Recent Progress of Nano-structured Anode Materials for Li-Ion Batteries. J. Power Sources 2014, 257, 421−443.
(3) Wang, Y.; Li, H.; He, P.; Hosono, E.; Zhou, H. Nano Active Materials for Lithium-Ion Batteries. Nanoscale 2010, 2, 1294−1305.

DOI: 10.1021/acs.chemrev.9b00405
Chem. Rev. XXXX, XXX, XXX−XXX

(4) Guo, Y.-G.; Hu, J.-S.; Wan, L.-J. Nanostructured Materials for Electrochemical Energy Conversion and Storage Devices. Adv. Mater. 2008, 20, 2878−2887.
(5) Van der Ven, A.; Wagemaker, M. Effect of Surface Energies and Nano-Particle Size Distribution on Open Circuit Voltage of Li-Electrodes. Electrochem. Commun. 2009, 11, 881−884.
(6) Meethong, N.; Huang, H.-Y. S.; Carter, W. C.; Chiang, Y.-M. Size-Dependent Lithium Miscibility Gap in Nanoscale $Li_{1-X}FePO_4$. Electrochem. Solid-State Lett. 2007, 10, A134−A138.
(7) Qian, D.; Hinuma, Y.; Chen, H.; Du, L.-S.; Carroll, K. J.; Ceder, G.; Grey, C. P.; Meng, Y. S. Electronic Spin Transition in Nanosize Stoichiometric Lithium Cobalt Oxide. J. Am. Chem. Soc. 2012, 134, 6096−6099.
(8) Shen, K.; Chen, H.; Klaver, F.; Mulder, F. M.; Wagemaker, M. Impact of Particle Size on the Non-Equilibrium Phase Transition of Lithium-Inserted Anatase Tio_2. Chem. Mater. 2014, 26, 1608−1615.
(9) Kim, S.-W.; Nam, K.-W.; Seo, D.-H.; Hong, J.; Kim, H.; Gwon, H.; Kang, K. Energy Storage in Composites of a Redox Couple Host and a Lithium Ion Host. Nano Today 2012, 7, 168−173.
(10) Jung, S.-K.; Kim, H.; Cho, M. G.; Cho, S.-P.; Lee, B.; Kim, H.; Park, Y.-U.; Hong, J.; Park, K.-Y.; Yoon, G.; Seong, W. M.; Cho, Y.; Oh, M. H.; Kim, H.; Gwon, H.; Hwang, I.; Hyeon, T.; Yoon, W.-S.; Kang, K. Lithium-Free Transition Metal Monoxides for Positive Electrodes in Lithium-Ion Batteries. Nat. Energy 2017, 2, 16208.
(11) Chen, C.-C.; Maier, J. Decoupling Electron and Ion Storage and the Path from Interfacial Storage to Artificial Electrodes. Nat. Energy 2018, 3, 102.
(12) Jung, S.-K.; Hwang, I.; Cho, S.-P.; Oh, K.; Ku, K.; Choi, I. R.; Kang, K. New Iron-Based Intercalation Host for Lithium-Ion Batteries. Chem. Mater. 2018, 30, 1956−1964.
(13) Lee, J.; Urban, A.; Li, X.; Su, D.; Hautier, G.; Ceder, G. Unlocking the Potential of Cation-Disordered Oxides for Rechargeable Lithium Batteries. Science 2014, 343, 519−522.
(14) Freire, M.; Kosova, N.; Jordy, C.; Chateigner, D.; Lebedev, O.; Maignan, A.; Pralong, V. A New Active Li−Mn−O Compound for High Energy Density Li-Ion Batteries. Nat. Mater. 2016, 15, 173−177.
(15) Lee, J.; Kitchaev, D. A.; Kwon, D.-H.; Lee, C.-W.; Papp, J. K.; Liu, Y.-S.; Lun, Z.; Clément, R. J.; Shi, T.; McCloskey, B. D.; et al. Reversible Mn^{2+}/Mn^{4+} Double Redox in Lithium-Excess Cathode Materials. Nature 2018, 556, 185−190.
(16) House, R. A.; Jin, L.; Maitra, U.; Tsuruta, K.; Somerville, J. W.; Förstermann, D. P.; Massel, F.; Duda, L.; Roberts, M. R.; Bruce, P. G. Lithium Manganese Oxyfluoride as a New Cathode Material Exhibiting Oxygen Redox. Energy Environ. Sci. 2018, 11, 926−932.
(17) Jamnik, J.; Maier, J. Nanocrystallinity Effects in Lithium Battery Materials Aspects of Nano-Ionics. Part Iv. Phys. Chem. Chem. Phys. 2003, 5, 5215−5220.
(18) Armstrong, A. R.; Armstrong, G.; Canales, J.; Bruce, P. G. Tio_2−B Nanowires as Negative Electrodes for Rechargeable Lithium Batteries. J. Power Sources 2005, 146, 501−506.
(19) Armstrong, G.; Armstrong, A. R.; Bruce, P. G.; Reale, P.; Scrosati, B. Tio_2(B) Nanowires as an Improved Anode Material for Lithium-Ion Batteries Containing $Lifepo_4$ or $Lini_{0.5}mn_{1.5}o_4$ Cathodes and a Polymer Electrolyte. Adv. Mater. 2006, 18, 2597−2600.
(20) Ren, Y.; Liu, Z.; Pourpoint, F.; Armstrong, A. R.; Grey, C. P.; Bruce, P. G. Nanoparticulate TiO_2(B): An Anode for Lithium-Ion Batteries. Angew. Chem. 2012, 124, 2206−2209.
(21) Li, X.; Wu, G.; Liu, X.; Li, W.; Li, M. Orderly Integration of Porous TiO_2(B) Nanosheets into Bunchy Hierarchical Structure for High-Rate and Ultralong-Lifespan Lithium-Ion Batteries. Nano Energy 2017, 31, 1−8.
(22) Borghols, W. J. H.; Wagemaker, M.; Lafont, U.; Kelder, E. M.; Mulder, F. M. Size Effects in the $Li_{4+X}ti_5o_{12}$ Spinel. J. Am. Chem. Soc. 2009, 131, 17786−17792.
(23) Haetge, J.; Hartmann, P.; Brezesinski, K.; Janek, J.; Brezesinski, T. Ordered Large-Pore Mesoporous $Li_4ti_5o_{12}$ Spinel Thin Film Electrodes with Nanocrystalline Framework for High Rate Rechargeable Lithium Batteries: Relationships among Charge Storage, Electrical Conductivity, and Nanoscale Structure. Chem. Mater. 2011, 23, 4384−4393.
(24) Feckl, J. M.; Fominykh, K.; Döblinger, M.; Fattakhova-Rohlfing, D.; Bein, T. Nanoscale Porous Framework of Lithium Titanate for Ultrafast Lithium Insertion. Angew. Chem., Int. Ed. 2012, 51, 7459−7463.
(25) Verde, M. G.; Baggetto, L.; Balke, N.; Veith, G. M.; Seo, J. K.; Wang, Z.; Meng, Y. S. Elucidating the Phase Transformation of $Li_4Ti_5O_{12}$ Lithiation at the Nanoscale. ACS Nano 2016, 10, 4312−4321.
(26) Brezesinski, K.; Wang, J.; Haetge, J.; Reitz, C.; Steinmueller, S. O.; Tolbert, S. H.; Smarsly, B. M.; Dunn, B.; Brezesinski, T. Pseudocapacitive Contributions to Charge Storage in Highly Ordered Mesoporous Group V Transition Metal Oxides with Iso-Oriented Layered Nanocrystalline Domains. J. Am. Chem. Soc. 2010, 132, 6982−6990.
(27) Kim, J. W.; Augustyn, V.; Dunn, B. The Effect of Crystallinity on the Rapid Pseudocapacitive Response of Nb_2O_5. Adv. Energy Mater. 2012, 2, 141−148.
(28) Augustyn, V.; Come, J.; Lowe, M. A.; Kim, J. W.; Taberna, P.-L.; Tolbert, S. H.; Abruña, H. D.; Simon, P.; Dunn, B. High-Rate Electrochemical Energy Storage through Li^+ Intercalation Pseudocapacitance. Nat. Mater. 2013, 12, 518−522.
(29) Lou, S.; Cheng, X.; Wang, L.; Gao, J.; Li, Q.; Ma, Y.; Gao, Y.; Zuo, P.; Du, C.; Yin, G. High-Rate Capability of Three-Dimensionally Ordered Macroporous T-Nb_2O_5 through Li^+ Intercalation Pseudocapacitance. J. Power Sources 2017, 361, 80−86.
(30) Chen, D.; Wang, J.-H.; Chou, T.-F.; Zhao, B.; El-Sayed, M. A.; Liu, M. Unraveling the Nature of Anomalously Fast Energy Storage in T-Nb_2O_5. J. Am. Chem. Soc. 2017, 139, 7071−7081.
(31) Shu, J. Study of the Interface between $Li_4ti_5o_{12}$ Electrodes and Standard Electrolyte Solutions in 0.0 − 5.0 V. Electrochem. Solid-State Lett. 2008, 11, A238−A240.
(32) Reddy, M. V.; Yu, T.; Sow, C. H.; Shen, Z. X.; Lim, C. T.; Subba Rao, G. V.; Chowdari, B. V. R. A-Fe_2O_3 Nanoflakes as an Anode Material for Li-Ion Batteries. Adv. Funct. Mater. 2007, 17, 2792−2799.
(33) Brezesinski, K.; Haetge, J.; Wang, J.; Mascotto, S.; Reitz, C.; Rein, A.; Tolbert, S. H.; Perlich, J.; Dunn, B.; Brezesinski, T. Ordered Mesoporous A-Fe_2O_3 (Hematite) Thin-Film Electrodes for Application in High Rate Rechargeable Lithium Batteries. Small 2011, 7, 407−414.
(34) Xu, X.; Cao, R.; Jeong, S.; Cho, J. Spindle-Like Mesoporous A-Fe_2O_3 Anode Material Prepared from Mof Template for High-Rate Lithium Batteries. Nano Lett. 2012, 12, 4988−4991.
(35) Guo, W.; Sun, W.; Lv, L.-P.; Kong, S.; Wang, Y. Microwave-Assisted Morphology Evolution of Fe-Based Metal−Organic Frameworks and Their Derived Fe_2o_3 Nanostructures for Li-Ion Storage. ACS Nano 2017, 11, 4198−4205.
(36) Li, Y.; Tan, B.; Wu, Y. Mesoporous Co_3o_4 Nanowire Arrays for Lithium Ion Batteries with High Capacity and Rate Capability. Nano Lett. 2008, 8, 265−270.
(37) Li, J.; He, K.; Meng, Q.; Li, X.; Zhu, Y.; Hwang, S.; Sun, K.; Gan, H.; Zhu, Y.; Mo, Y.; et al. Kinetic Phase Evolution of Spinel Cobalt Oxide During Lithiation. ACS Nano 2016, 10, 9577−9585.
(38) Bhojane, P.; Sinha, L.; Devan, R. S.; Shirage, P. M. Mesoporous Layered Hexagonal Platelets of Co_3O_4 Nanoparticles with (111) Facets for Battery Applications: High Performance and Ultra-High Rate Capability. Nanoscale 2018, 10, 1779−1787.
(39) Xiao, Y.; Hu, C.; Cao, M. High Lithium Storage Capacity and Rate Capability Achieved by Mesoporous Co_3o_4 Hierarchical Nanobundles. J. Power Sources 2014, 247, 49−56.
(40) Okubo, M.; Hosono, E.; Kim, J.; Enomoto, M.; Kojima, N.; Kudo, T.; Zhou, H.; Honma, I. Nanosize Effect on High-Rate Li-Ion Intercalation in $Licoo_2$ Electrode. J. Am. Chem. Soc. 2007, 129, 7444−7452.
(41) Scott, I. D.; Jung, Y. S.; Cavanagh, A. S.; Yan, Y.; Dillon, A. C.; George, S. M.; Lee, S.-H. Ultrathin Coatings on Nano-$LiCoO_2$ for Li-Ion Vehicular Applications. Nano Lett. 2011, 11, 414−418.

AQ

DOI: 10.1021/acs.chemrev.9b00405
Chem. Rev. XXXX, XXX, XXX−XXX

(42) Tai, Z.; Subramaniyam, C. M.; Chou, S.-L.; Chen, L.; Liu, H.-K.; Dou, S.-X. Few Atomic Layered Lithium Cathode Materials to Achieve Ultrahigh Rate Capability in Lithium-Ion Batteries. Adv. Mater. 2017, 29, 1700605.
(43) Gu, Y.; Chen, D.; Jiao, X. Synthesis and Electrochemical Properties of Nanostructured Licoo$_2$ Fibers as Cathode Materials for Lithium-Ion Batteries. J. Phys. Chem. B 2005, 109, 17901−17906.
(44) Xue, L.; Savilov, S. V.; Lunin, V. V.; Xia, H. Self-Standing Porous $LiCoO_2$ Nanosheet Arrays as 3d Cathodes for Flexible Li-Ion Batteries. Adv. Funct. Mater. 2018, 28, 1705836.
(45) Kang, B.; Ceder, G. Battery Materials for Ultrafast Charging and Discharging. Nature 2009, 458, 190−193.
(46) Liu, H.; Strobridge, F. C.; Borkiewicz, O. J.; Wiaderek, K. M.; Chapman, K. W.; Chupas, P. J.; Grey, C. P. Capturing Metastable Structures During High-Rate Cycling of Lifepo$_4$ Nanoparticle Electrodes. Science 2014, 344, 1252817.
(47) Peng, L.; Zhao, Y.; Ding, Y.; Yu, G. Self-Assembled Lifepo$_4$ Nanowires with High Rate Capability for Li-Ion Batteries. Chem. Commun. 2014, 50, 9569−9572.
(48) Put, B.; Vereecken, P. M.; Labyedh, N.; Sepulveda, A.; Huyghebaert, C.; Radu, I. P.; Stesmans, A. High Cycling Stability and Extreme Rate Performance in Nanoscaled $LiMn_2O_4$ Thin Films. ACS Appl. Mater. Interfaces 2015, 7, 22413−22420.
(49) Hua, W.-B.; Wang, S.-N.; Guo, X.-D.; Chou, S.-L.; Yin, K.; Zhong, B.-H.; Dou, S.-X. Vacuum Induced Self-Assembling Nanoporous $LiMn_2O_4$ for Lithium Ion Batteries with Superior High Rate Capability. Electrochim. Acta 2015, 186, 253−261.
(50) Tang, W.; Hou, Y.; Wang, F.; Liu, L.; Wu, Y.; Zhu, K. Limn$_2$o$_4$ Nanotube as Cathode Material of Second-Level Charge Capability for Aqueous Rechargeable Batteries. Nano Lett. 2013, 13, 2036−2040.
(51) Malik, R.; Burch, D.; Bazant, M.; Ceder, G. Particle Size Dependence of the Ionic Diffusivity. Nano Lett. 2010, 10, 4123−4127.
(52) Guo, B.; Ruan, H.; Zheng, C.; Fei, H.; Wei, M. Hierarchical Lifepo$_4$ with a Controllable Growth of the (010) Facet for Lithium-Ion Batteries. Sci. Rep. 2013, 3, 2788.
(53) Jiang, C.; Tang, Z.; Wang, S.; Zhang, Z. A Truncated Octahedral Spinel $LiMn_2O_4$ as High-Performance Cathode Material for Ultrafast and Long-Life Lithium-Ion Batteries. J. Power Sources 2017, 357, 144−148.
(54) Cai, Y.; Huang, S.-Z.; She, F.-S.; Liu, J.; Zhang, R.-L.; Huang, Z.-H.; Wang, F.-Y.; Wang, H.-E. Facile Synthesis of Well-Shaped Spinel $LiNi_{0.5}Mn_{1.5}O_4$ Nanoparticles as Cathode Materials for Lithium Ion Batteries. RSC Adv. 2016, 6, 2785−2792.
(55) Luo, C.; Huang, R.; Kevorkyants, R.; Pavanello, M.; He, H.; Wang, C. Self-Assembled Organic Nanowires for High Power Density Lithium Ion Batteries. Nano Lett. 2014, 14, 1596−1602.
(56) Wang, Y.; Ding, Y.; Pan, L.; Shi, Y.; Yue, Z.; Shi, Y.; Yu, G. Understanding the Size-Dependent Sodium Storage Properties of $Na_2C_6O_6$-Based Organic Electrodes for Sodium-Ion Batteries. Nano Lett. 2016, 16, 3329−3334.
(57) Wan, F.; Wu, X.-L.; Guo, J.-Z.; Li, J.-Y.; Zhang, J.-P.; Niu, L.; Wang, R.-S. Nanoeffects Promote the Electrochemical Properties of Organic $Na_2C_8H_4O_4$ as Anode Material for Sodium-Ion Batteries. Nano Energy 2015, 13, 450−457.
(58) Wang, S.; Wang, L.; Zhang, K.; Zhu, Z.; Tao, Z.; Chen, J. Organic Li$_4$c$_8$h$_2$o$_6$ Nanosheets for Lithium-Ion Batteries. Nano Lett. 2013, 13, 4404−4409.
(59) Peng, Z.; Freunberger, S. A.; Chen, Y.; Bruce, P. G. A Reversible and Higher-Rate Li-O_2 Battery. Science 2012, 337, 563−566.
(60) Zhao, C.; Yu, C.; Liu, S.; Yang, J.; Fan, X.; Huang, H.; Qiu, J. 3d Porous N-Doped Graphene Frameworks Made of Interconnected Nanocages for Ultrahigh-Rate and Long-Life Li−O_2 Batteries. Adv. Funct. Mater. 2015, 25, 6913−6920.
(61) Wu, F.; Xing, Y.; Zeng, X.; Yuan, Y.; Zhang, X.; Shahbazian-Yassar, R.; Wen, J.; Miller, D. J.; Li, L.; Chen, R.; et al. Platinum-Coated Hollow Graphene Nanocages as Cathode Used in Lithium-Oxygen Batteries. Adv. Funct. Mater. 2016, 26, 7626−7633.
(62) Li, F.; Tang, D.-M.; Zhang, T.; Liao, K.; He, P.; Golberg, D.; Yamada, A.; Zhou, H. Superior Performance of a Li−O_2 Battery with Metallic RuO_2 Hollow Spheres as the Carbon-Free Cathode. Adv. Energy Mater. 2015, 5, 1500294.
(63) Liao, K.; Wang, X.; Sun, Y.; Tang, D.; Han, M.; He, P.; Jiang, X.; Zhang, T.; Zhou, H. An Oxygen Cathode with Stable Full Discharge−Charge Capability Based on 2d Conducting Oxide. Energy Environ. Sci. 2015, 8, 1992−1997.
(64) Wang, F.; Wen, Z.; Shen, C.; Rui, K.; Wu, X.; Chen, C. Open Mesoporous Spherical Shell Structured Co_3O_4 with Highly Efficient Catalytic Performance in Li−O_2 Batteries. J. Mater. Chem. A 2015, 3, 7600−7606.
(65) Lee, G.-H.; Lee, S.; Kim, J.-C.; Kim, D. W.; Kang, Y.; Kim, D.-W. $MnMoO_4$ Electrocatalysts for Superior Long-Life and High-Rate Lithium-Oxygen Batteries. Adv. Energy Mater. 2017, 7, 1601741.
(66) Zhou, T.; Lv, W.; Li, J.; Zhou, G.; Zhao, Y.; Fan, S.; Liu, B.; Li, B.; Kang, F.; Yang, Q.-H. Twinborn TiO_2−Tin Heterostructures Enabling Smooth Trapping−Diffusion−Conversion of Polysulfides Towards Ultralong Life Lithium−Sulfur Batteries. Energy Environ. Sci. 2017, 10, 1694−1703.
(67) Sun, Z.; Zhang, J.; Yin, L.; Hu, G.; Fang, R.; Cheng, H.-M.; Li, F. Conductive Porous Vanadium Nitride/Graphene Composite as Chemical Anchor of Polysulfides for Lithium-Sulfur Batteries. Nat. Commun. 2017, 8, 14627.
(68) Xu, Z.-L.; Huang, J.-Q.; Chong, W. G.; Qin, X.; Wang, X.; Zhou, L.; Kim, J.-K. In Situ Tem Study of Volume Expansion in Porous Carbon Nanofiber/Sulfur Cathodes with Exceptional High-Rate Performance. Adv. Energy Mater. 2017, 7, 1602078.
(69) Seo, D.-H.; Park, K.-Y.; Kim, H.; Jung, S.-K.; Park, M.-S.; Kang, K. Intrinsic Nanodomains in Triplite $LiFeSO_4F$ and Its Implication in Lithium-Ion Diffusion. Adv. Energy Mater. 2018, 8, 1701408.
(70) Kim, J. C.; Seo, D.-H.; Chen, H.; Ceder, G. The Effect of Antisite Disorder and Particle Size on Li Intercalation Kinetics in Monoclinic $LiMnBO_3$. Adv. Energy Mater. 2015, 5, 1401916.
(71) Yamada, A.; Koizumi, H.; Nishimura, S.-i.; Sonoyama, N.; Kanno, R.; Yonemura, M.; Nakamura, T.; Kobayashi, Y. Room-Temperature Miscibility Gap in Li_xFePO_4. Nat. Mater. 2006, 5, 357−360.
(72) Wagemaker, M.; Borghols, W. J. H.; Mulder, F. M. Large Impact of Particle Size on Insertion Reactions. A Case for Anatase Li_xtio$_2$. J. Am. Chem. Soc. 2007, 129, 4323−4327.
(73) Gao, N.; Yan, Y. Characterisation of Surface Wettability Based on Nanoparticles. Nanoscale 2012, 4, 2202−2218.
(74) Liu, J.; Papadakis, R.; Li, H. Experimental Observation of Size-Dependent Behavior in Surface Energy of Gold Nanoparticles through Atomic Force Microscope. Appl. Phys. Lett. 2018, 113, 083108.
(75) Awada, H.; Castelein, G.; Brogly, M. Quantitative Determination of Surface Energy Using Atomic Force Microscopy: The Case of Hydrophobic/Hydrophobic Contact and Hydrophilic/Hydrophilic Contact. Surf. Interface Anal. 2005, 37, 755−764.
(76) Ma, W.; Zhang, C.; Liu, C.; Nan, X.; Fu, H.; Cao, G. Impacts of Surface Energy on Lithium Ion Intercalation Properties of V_2O_5. ACS Appl. Mater. Interfaces 2016, 8, 19542−19549.
(77) Zhang, C.; Wang, K.; Liu, C.; Nan, X.; Fu, H.; Ma, W.; Li, Z.; Cao, G. Effects of High Surface Energy on Lithium-Ion Intercalation Properties of Ni-Doped Li_3VO_4. NPG Asia Mater. 2016, 8, No. e287.
(78) Kang, J. W.; Kim, D. H.; Mathew, V.; Lim, J. S.; Gim, J. H.; Kim, J. Particle Size Effect of Anatase TiO_2 Nanocrystals for Lithium-Ion Batteries. J. Electrochem. Soc. 2011, 158, A59−A62.
(79) Wang, R.; Lang, J.; Liu, Y.; Lin, Z.; Yan, X. Ultra-Small, Size-Controlled $Ni(OH)_2$ Nanoparticles: Elucidating the Relationship between Particle Size and Electrochemical Performance for Advanced Energy Storage Devices. NPG Asia Mater. 2015, 7, No. e183.
(80) Wang, F.; Robert, R.; Chernova, N. A.; Pereira, N.; Omenya, F.; Badway, F.; Hua, X.; Ruotolo, M.; Zhang, R.; Wu, L.; et al. Conversion Reaction Mechanisms in Lithium Ion Batteries: Study of the Binary Metal Fluoride Electrodes. J. Am. Chem. Soc. 2011, 133, 18828−18836.

DOI: 10.1021/acs.chemrev.9b00405
Chem. Rev. XXXX, XXX, XXX−XXX

(81) Yamakawa, N.; Jiang, M.; Grey, C. P. Investigation of the Conversion Reaction Mechanisms for Binary Copper(II) Compounds by Solid-State NMR Spectroscopy and X-Ray Diffraction. Chem. Mater. 2009, 21, 3162−3176.
(82) Yamakawa, N.; Jiang, M.; Key, B.; Grey, C. P. Identifying the Local Structures Formed During Lithiation of the Conversion Material, Iron Fluoride, in a Li Ion Battery: A Solid-State NMR, X-Ray Diffraction, and Pair Distribution Function Analysis Study. J. Am. Chem. Soc. 2009, 131, 10525−10536.
(83) Liu, P.; Vajo, J. J.; Wang, J. S.; Li, W.; Liu, J. Thermodynamics and Kinetics of the Li/FeF_3 Reaction by Electrochemical Analysis. J. Phys. Chem. C 2012, 116, 6467−6473.
(84) Badway, F.; Mansour, A. N.; Pereira, N.; Al-Sharab, J. F.; Cosandey, F.; Plitz, I.; Amatucci, G. G. Structure and Electrochemistry of Copper Fluoride Nanocomposites Utilizing Mixed Conducting Matrices. Chem. Mater. 2007, 19, 4129−4141.
(85) Seo, J. K.; Cho, H.-M.; Takahara, K.; Chapman, K. W.; Borkiewicz, O. J.; Sina, M.; Shirley Meng, Y. Revisiting the Conversion Reaction Voltage and the Reversibility of the CuF_2 Electrode in Li-Ion Batteries. Nano Res. 2017, 10, 4232−4244.
(86) Kobayashi, G.; Nishimura, S.-i.; Park, M.-S.; Kanno, R.; Yashima, M.; Ida, T.; Yamada, A. Isolation of Solid Solution Phases in Size-Controlled Lixfepo4 at Room Temperature. Adv. Funct. Mater. 2009, 19, 395−403.
(87) Wagemaker, M.; Singh, D. P.; Borghols, W. J. H.; Lafont, U.; Haverkate, L.; Peterson, V. K.; Mulder, F. M. Dynamic Solubility Limits in Nanosized Olivine Lifepo4. J. Am. Chem. Soc. 2011, 133, 10222−10228.
(88) Chen, G.; Song, X.; Richardson, T. J. Electron Microscopy Study of the $LiFePO_4$ to $FePO_4$ Phase Transition. Electrochem. Solid-State Lett. 2006, 9, A295−A298.
(89) Meethong, N.; Huang, H. Y. S.; Speakman, S. A.; Carter, W. C.; Chiang, Y. M. Strain Accommodation During Phase Transformations in Olivine-Based Cathodes as a Materials Selection Criterion for High-Power Rechargeable Batteries. Adv. Funct. Mater. 2007, 17, 1115−1123.
(90) Wagemaker, M.; Mulder, F. M.; Van der Ven, A. The Role of Surface and Interface Energy on Phase Stability of Nanosized Insertion Compounds. Adv. Mater. 2009, 21, 2703−2709.
(91) Bock, D. C.; Pelliccione, C. J.; Zhang, W.; Timoshenko, J.; Knehr, K. W.; West, A. C.; Wang, F.; Li, Y.; Frenkel, A. I.; Takeuchi, E. S.; et al. Size Dependent Behavior of Fe_3O_4 Crystals During Electrochemical (De)Lithiation: An in Situ X-Ray Diffraction, Ex Situ X-Ray Absorption Spectroscopy, Transmission Electron Microscopy and Theoretical Investigation. Phys. Chem. Chem. Phys. 2017, 19, 20867−20880.
(92) Luo, L.; Zhao, B.; Xiang, B.; Wang, C.-M. Size-Controlled Intercalation-to-Conversion Transition in Lithiation of Transition-Metal Chalcogenides—$NbSe_3$. ACS Nano 2016, 10, 1249−1255.
(93) Liu, X. H.; Zhang, L. Q.; Zhong, L.; Liu, Y.; Zheng, H.; Wang, J. W.; Cho, J.-H.; Dayeh, S. A.; Picraux, S. T.; Sullivan, J. P.; et al. Ultrafast Electrochemical Lithiation of Individual Si Nanowire Anodes. Nano Lett. 2011, 11, 2251−2258.
(94) Jia, Z.; Li, T. Stress-Modulated Driving Force for Lithiation Reaction in Hollow Nano-Anodes. J. Power Sources 2015, 275, 866−876.
(95) Yang, H.; Liang, W.; Guo, X.; Wang, C.-M.; Zhang, S. Strong Kinetics-Stress Coupling in Lithiation of Si and Ge Anodes. Extreme Mech. Lett. 2015, 2, 1−6.
(96) Gu, M.; Yang, H.; Perea, D. E.; Zhang, J.-G.; Zhang, S.; Wang, C.-M. Bending-Induced Symmetry Breaking of Lithiation in Germanium Nanowires. Nano Lett. 2014, 14, 4622−4627.
(97) Ding, B.; Wu, H.; Xu, Z.; Li, X.; Gao, H. Stress Effects on Lithiation in Silicon. Nano Energy 2017, 38, 486−493.
(98) Park, S.; Lee, C. W.; Kim, J.-C.; Song, H. J.; Shim, H.-W.; Lee, S.; Kim, D.-W. Heteroepitaxy-Induced Rutile VO_2 with Abundantly Exposed (002) Facets for High Lithium Electroactivity. ACS Energy Lett. 2016, 1, 216−224.
(99) Muralidharan, N.; Brock, C. N.; Cohn, A. P.; Schauben, D.; Carter, R. E.; Oakes, L.; Walker, D. G.; Pint, C. L. Tunable Mechanochemistry of Lithium Battery Electrodes. ACS Nano 2017, 11, 6243−6251.
(100) Shi, F.; Song, Z.; Ross, P. N.; Somorjai, G. A.; Ritchie, R. O.; Komvopoulos, K. Failure Mechanisms of Single-Crystal Silicon Electrodes in Lithium-Ion Batteries. Nat. Commun. 2016, 7, 11886.
(101) Berla, L. A.; Lee, S. W.; Cui, Y.; Nix, W. D. Mechanical Behavior of Electrochemically Lithiated Silicon. J. Power Sources 2015, 273, 41−51.
(102) Zhao, K.; Pharr, M.; Vlassak, J. J.; Suo, Z. Fracture of Electrodes in Lithium-Ion Batteries Caused by Fast Charging. J. Appl. Phys. 2010, 108, 073517.
(103) Liu, X. H.; Zhong, L.; Huang, S.; Mao, S. X.; Zhu, T.; Huang, J. Y. Size-Dependent Fracture of Silicon Nanoparticles During Lithiation. ACS Nano 2012, 6, 1522−1531.
(104) Ryu, I.; Choi, J. W.; Cui, Y.; Nix, W. D. Size-Dependent Fracture of Si Nanowire Battery Anodes. J. Mech. Phys. Solids 2011, 59, 1717−1730.
(105) Wang, H.; Jang, Y. I.; Huang, B.; Sadoway, D. R.; Chiang, Y. M. Tem Study of Electrochemical Cycling-Induced Damage and Disorder in $LiCoO_2$ Cathodes for Rechargeable Lithium Batteries. J. Electrochem. Soc. 1999, 146, 473−480.
(106) Yao, Y.; McDowell, M. T.; Ryu, I.; Wu, H.; Liu, N.; Hu, L.; Nix, W. D.; Cui, Y. Interconnected Silicon Hollow Nanospheres for Lithium-Ion Battery Anodes with Long Cycle Life. Nano Lett. 2011, 11, 2949−2954.
(107) Lee, W.-J.; Chun, Y.-G.; Jang, S.-J.; Paek, S.-M.; Oh, J.-M. Hierarchical Nanostructure of RuO_2 Hollow Spheres with Enhanced Lithium Ion Storage and Cyclic Performance. J. Alloys Compd. 2017, 711, 611−616.
(108) Ding, S.; Chen, J. S.; Qi, G.; Duan, X.; Wang, Z.; Giannelis, E. P.; Archer, L. A.; Lou, X. W. Formation of SnO_2 Hollow Nanospheres inside Mesoporous Silica Nanoreactors. J. Am. Chem. Soc. 2011, 133, 21−23.
(109) Feng, Y.; Li, X.; Shao, Z.; Wang, H. Morphology-Dependent Performance of Zn_2GeO_4 as a High-Performance Anode Material for Rechargeable Lithium Ion Batteries. J. Mater. Chem. A 2015, 3, 15274−15279.
(110) Yan, N.; Wang, F.; Zhong, H.; Li, Y.; Wang, Y.; Hu, L.; Chen, Q. Hollow Porous SiO_2 Nanocubes Towards High-Performance Anodes for Lithium-Ion Batteries. Sci. Rep. 2013, 3, 1568.
(111) Zhu, M.; Park, J.; Sastry, A. M. Fracture Analysis of the Cathode in Li-Ion Batteries: A Simulation Study. J. Electrochem. Soc. 2012, 159, A492−A498.
(112) Sun, H.; Xin, G.; Hu, T.; Yu, M.; Shao, D.; Sun, X.; Lian, J. High-Rate Lithiation-Induced Reactivation of Mesoporous Hollow Spheres for Long-Lived Lithium-Ion Batteries. Nat. Commun. 2014, 5, 4526.
(113) Luo, L.; Yang, H.; Yan, P.; Travis, J. J.; Lee, Y.; Liu, N.; Molina Piper, D.; Lee, S.-H.; Zhao, P.; George, S. M.; et al. Surface-Coating Regulated Lithiation Kinetics and Degradation in Silicon Nanowires for Lithium Ion Battery. ACS Nano 2015, 9, 5559−5566.
(114) Liu, Y.; Liu, X. H.; Nguyen, B.-M.; Yoo, J.; Sullivan, J. P.; Picraux, S. T.; Huang, J. Y.; Dayeh, S. A. Tailoring Lithiation Behavior by Interface and Bandgap Engineering at the Nanoscale. Nano Lett. 2013, 13, 4876−4883.
(115) Su, J.; Cao, M.; Ren, L.; Hu, C. Fe_3O_4−Graphene Nanocomposites with Improved Lithium Storage and Magnetism Properties. J. Phys. Chem. C 2011, 115, 14469−14477.
(116) Lian, P.; Zhu, X.; Xiang, H.; Li, Z.; Yang, W.; Wang, H. Enhanced Cycling Performance of Fe_3O_4−Graphene Nanocomposite as an Anode Material for Lithium-Ion Batteries. Electrochim. Acta 2010, 56, 834−840.
(117) Wang, H.; Cui, L.-F.; Yang, Y.; Sanchez Casalongue, H.; Robinson, J. T.; Liang, Y.; Cui, Y.; Dai, H. Mn_3O_4− Graphene Hybrid as a High-Capacity Anode Material for Lithium Ion Batteries. J. Am. Chem. Soc. 2010, 132, 13978−13980.

DOI: 10.1021/acs.chemrev.9b00405
Chem. Rev. XXXX, XXX, XXX−XXX

(118) Kim, J.; Kim, H.; Kang, K. Conversion-Based Cathode Materials for Rechargeable Sodium Batteries. Adv. Energy Mater. 2018, 8, 1702646.
(119) Yu, S. H.; Lee, S. H.; Lee, D. J.; Sung, Y. E.; Hyeon, T. Conversion Reaction-Based Oxide Nanomaterials for Lithium Ion Battery Anodes. Small 2016, 12, 2146−2172.
(120) Wu, F.; Yushin, G. Conversion Cathodes for Rechargeable Lithium and Lithium-Ion Batteries. Energy Environ. Sci. 2017, 10, 435−459.
(121) Cabana, J.; Monconduit, L.; Larcher, D.; Palacin, M. R. Beyond Intercalation-Based Li-Ion Batteries: The State of the Art and Challenges of Electrode Materials Reacting through Conversion Reactions. Adv. Mater. 2010, 22, E170−E192.
(122) Conte, D. E.; Pinna, N. J. M. f. R. A Review on the Application of Iron (III) Fluorides as Positive Electrodes for Secondary Cells. Mater. Renew. Sustain. Energy 2014, 3, 37.
(123) Arai, H.; Okada, S.; Sakurai, Y.; Yamaki, J.-i. Cathode Performance and Voltage Estimation of Metal Trihalides. J. Power Sources 1997, 68, 716−719.
(124) Badway, F.; Pereira, N.; Cosandey, F.; Amatucci, G. Carbon-Metal Fluoride Nanocomposites Structure and Electrochemistry of FeF_3: C. J. Electrochem. Soc. 2003, 150, A1209−A1218.
(125) Li, L.; Jacobs, R.; Gao, P.; Gan, L.; Wang, F.; Morgan, D.; Jin, S. Origins of Large Voltage Hysteresis in High-Energy-Density Metal Fluoride Lithium-Ion Battery Conversion Electrodes. J. Am. Chem. Soc. 2016, 138, 2838−2848.
(126) Liao, P.; MacDonald, B. L.; Dunlap, R.; Dahn, J. Combinatorially Prepared $[LiF]_{1-X}Fe_X$ Nanocomposites for Positive Electrode Materials in Li-Ion Batteries. Chem. Mater. 2008, 20, 454−461.
(127) Hori, H.; Okada, S. Reconversion Reaction of LiF/Fe Composite Thin Film Cathodes for Lithium-Ion Battery. Electrochemistry 2015, 83, 909−913.
(128) Li, T.; Chen, Z. X.; Ai, X. P.; Cao, Y. L.; Yang, H. X. LiF/Fe Nanocomposite as a Lithium-Rich and High Capacity Conversion Cathode Material for Li-Ion Batteries. J. Power Sources 2012, 217, 54−58.
(129) Das, B.; Pohl, A.; Chakravadhanula, V.; Kübel, C.; Fichtner, M. $LiF/Fe/V_2O_5$ Nanocomposite as High Capacity Cathode for Lithium Ion Batteries. J. Power Sources 2014, 267, 203−211.
(130) Pohl, A.; Guda, A.; Shapovalov, V.; Witte, R.; Das, B.; Scheiba, F.; Rothe, J.; Soldatov, A.; Fichtner, M. Oxidation State and Local Structure of a High-Capacity LiF/Fe (V_2O_5) Conversion Cathode for Li-Ion Batteries. Acta Mater. 2014, 68, 179−188.
(131) Prakash, R.; Wall, C.; Mishra, A. K.; Kübel, C.; Ghafari, M.; Hahn, H.; Fichtner, M. Modified Synthesis of [Fe/LiF/C] Nanocomposite, and Its Application as Conversion Cathode Material in Lithium Batteries. J. Power Sources 2011, 196, 5936−5944.
(132) Zhang, S.; Lu, Y.; Xu, G.; Li, Y.; Zhang, X. LiF/Fe/C Nanofibres as a High-Capacity Cathode Material for Li-Ion Batteries. J. Phys. D: Appl. Phys. 2012, 45, 395301.
(133) Ma, R.; Dong, Y.; Xi, L.; Yang, S.; Lu, Z.; Chung, C. Fabrication of LiF/Fe/Graphene Nanocomposites as Cathode Material for Lithium-Ion Batteries. ACS Appl. Mater. Interfaces 2013, 5, 892−897.
(134) Amatucci, G.; Pereira, N.; Badway, F.; Sina, M.; Cosandey, F.; Ruotolo, M.; Cao, C. Formation of Lithium Fluoride/Metal Nanocomposites for Energy Storage through Solid State Reduction of Metal Fluorides. J. Fluorine Chem. 2011, 132, 1086−1094.
(135) Zhao, Y.; Wei, K.; Wu, H.; Ma, S.; Li, J.; Cui, Y.; Dong, Z.; Cui, Y.; Li, C. LiF Splitting Catalyzed by Dual Metal Nanodomains for an Efficient Fluoride Conversion Cathode. ACS Nano 2019, 13, 2490−2500.
(136) Wang, F.; Kim, S.-W.; Seo, D.-H.; Kang, K.; Wang, L.; Su, D.; Vajo, J. J.; Wang, J.; Graetz, J. Ternary Metal Fluorides as High-Energy Cathodes with Low Cycling Hysteresis. Nat. Commun. 2015, 6, 6668.
(137) Poizot, P.; Laruelle, S.; Grugeon, S.; Dupont, L.; Tarascon, J. M. Nano-Sized Transition-Metal Oxides as Negative-Electrode Materials for Lithium-Ion Batteries. Nature 2000, 407, 496−499.
(138) Zhong, K.; Xia, X.; Zhang, B.; Li, H.; Wang, Z.; Chen, L. Mno Powder as Anode Active Materials for Lithium Ion Batteries. J. Power Sources 2010, 195, 3300−3308.
(139) Zhang, L.; Dambournet, D.; Iadecola, A.; Batuk, D.; Borkiewicz, O. J.; Wiaderek, K. M.; Salager, E.; Shao, M.; Chen, G.; Tarascon, J.-M. Origin of the High Capacity Manganese-Based Oxyfluoride Electrodes for Rechargeable Batteries. Chem. Mater. 2018, 30, 5362−5372.
(140) Dimov, N.; Kitajou, A.; Hori, H.; Kobayashi, E.; Okada, S. Electrochemical Splitting of LiF: A New Approach to Lithium-Ion Battery Materials. ECS Trans. 2014, 58, 87−99.
(141) Zhang, L.; Chen, G.; Berg, E. J.; Tarascon, J. M. Triggering the in Situ Electrochemical Formation of High Capacity Cathode Material from Mno. Adv. Energy Mater. 2017, 7, 1602200.
(142) Kawamura, T.; Okada, S.; Yamaki, J.-i. Decomposition Reaction of $LiPF_6$-Based Electrolytes for Lithium Ion Cells. J. Power Sources 2006, 156, 547−554.
(143) Zhang, L.; Batuk, D.; Chen, G.; Tarascon, J.-M. Electrochemically Activated MnO as a Cathode Material for Sodium-Ion Batteries. Electrochem. Commun. 2017, 77, 81−84.
(144) Jung, S. K.; Hwang, I.; Choi, I. R.; Yoon, G.; Park, J. H.; Park, K. Y.; Kang, K. Chemical Origins of Electrochemical Overpotential in Surface-Conversion Nanocomposite Cathodes. Adv. Energy Mater. 2019, 9, 1900503.
(145) Tomita, Y.; Nasu, H.; Izumi, Y.; Arai, J.; Otsuka, S.; Yamane, Y.; Yamada, K.; Kohno, Y.; Kobayashi, K. Synthesis and Charge-Discharge Properties of LiF-NiO Composite as a Cathode Material for Li-Ion Batteries. J. Power Sources 2016, 329, 406−411.
(146) Tomita, Y.; Kimura, N.; Izumi, Y.; Arai, J.; Kohno, Y.; Kobayashi, K. Synthesis and Electrochemical Properties of 4LiF-$NiMn_2O_4$ Composite as a Cathode Material for Li-Ion Batteries. J. Power Sources 2017, 354, 34−40.
(147) Tawa, S.; Sato, Y.; Orikasa, Y.; Matsumoto, K.; Hagiwara, R. Lithium Fluoride/Iron Difluoride Composite Prepared by a Fluorolytic Sol−Gel Method: Its Electrochemical Behavior and Charge−Discharge Mechanism as a Cathode Material for Lithium Secondary Batteries. J. Power Sources 2019, 412, 180−188.
(148) Hwang, I.; Jung, S.-K.; Jeong, E.-S.; Kim, H.; Cho, S.-P.; Ku, K.; Kim, H.; Yoon, W.-S.; Kang, K. $NaF-FeF_2$ Nanocomposite: New Type of Na-Ion Battery Cathode Material. Nano Res. 2017, 10, 4388−4397.
(149) Kitajou, A.; Ishado, Y.; Inoishi, A.; Okada, S. Amorphous $XLiF\text{-}FeSO_4$ ($1 \leq X \leq 2$) Composites as a Cathode Material for Lithium Ion Batteries. Solid State Ionics 2018, 326, 48−51.
(150) Barpanda, P.; Ati, M.; Melot, B. C.; Rousse, G.; Chotard, J.-N.; Doublet, M.-L.; Sougrati, M. T.; Corr, S.; Jumas, J.-C.; Tarascon, J.-M. A 3.90 V Iron-Based Fluorosulphate Material for Lithium-Ion Batteries Crystallizing in the Triplite Structure. Nat. Mater. 2011, 10, 772−779.
(151) Recham, N.; Chotard, J. N.; Dupont, L.; Delacourt, C.; Walker, W.; Armand, M.; Tarascon, J.-M. 6 V Lithium-Based Fluorosulphate Insertion Positive Electrode for Lithium-Ion Batteries. Nat. Mater. 2010, 9, 68−74.
(152) Zhou, Y. N.; Sina, M.; Pereira, N.; Yu, X.; Amatucci, G. G.; Yang, X. Q.; Cosandey, F.; Nam, K. W. $FeO_{0.7}F_{1.3}$/C Nanocomposite as a High-Capacity Cathode Material for Sodium-Ion Batteries. Adv. Funct. Mater. 2015, 25, 696−703.
(153) Pereira, N.; Badway, F.; Wartelsky, M.; Gunn, S.; Amatucci, G. Iron Oxyfluorides as High Capacity Cathode Materials for Lithium Batteries. J. Electrochem. Soc. 2009, 156, A407−A416.
(154) Hwang, I.; Jung, S.-K.; Cho, S.-P.; Kang, K. In Operando Formation of New Iron-Oxyfluoride Host Structure for Na-Ion Storage from NaF−FeO Nanocomposite. Energy Storage Mater. 2019, 23, 427−433.
(155) Kataoka, R.; Kitta, M.; Takeichi, N.; Kiyobayashi, T. Electrochemical in Situ Synthesis: A New Synthesis Route for

DOI: 10.1021/acs.chemrev.9b00405
Chem. Rev. XXXX, XXX, XXX−XXX

Redox Active Manganese Oxides for Rechargeable Sodium Ion Battery through Initial Charge Process. J. Electrochem. Soc. 2017, 164, A226−A230.
(156) Balaya, P.; Li, H.; Kienle, L.; Maier, J. Fully Reversible Homogeneous and Heterogeneous Li Storage in RuO_2 with High Capacity. Adv. Funct. Mater. 2003, 13, 621−625.
(157) Chen, C.-C.; Fu, L.; Maier, J. Synergistic, Ultrafast Mass Storage and Removal in Artificial Mixed Conductors. Nature 2016, 536, 159−164.
(158) Chen, C.-C.; Maier, J. Space Charge Storage in Composites: Thermodynamics. Phys. Chem. Chem. Phys. 2017, 19, 6379−6396.
(159) Fu, L.; Chen, C.-C.; Samuelis, D.; Maier, J. Thermodynamics of Lithium Storage at Abrupt Junctions: Modeling and Experimental Evidence. Phys. Rev. Lett. 2014, 112, 208301.
(160) Li, H.; Balaya, P.; Maier, J. Li-Storage Via Heterogeneous Reaction in Selected Binary Metal Fluorides and Oxides. J. Electrochem. Soc. 2004, 151, A1878−A1885.
(161) Chen, C.-C.; Maier, J. Increased Storage through Heterogeneous Doping. Chem. Mater. 2018, 30, 5041−5049.
(162) Fu, L.; Tang, K.; Oh, H.; Manickam, K.; Bräuniger, T.; Chandran, C. V.; Menzel, A.; Hirscher, M.; Samuelis, D.; Maier, J. Job-Sharing" Storage of Hydrogen in Ru/Li_2O Nanocomposites. Nano Lett. 2015, 15, 4170−4175.
(163) Yu, X.; Yun, S.; Yeon, J. S.; Bhattacharya, P.; Wang, L.; Lee, S. W.; Hu, X.; Park, H. S. Emergent Pseudocapacitance of 2d Nanomaterials. Adv. Energy Mater. 2018, 8, 1702930.
(164) Shao, Y.; El-Kady, M. F.; Sun, J.; Li, Y.; Zhang, Q.; Zhu, M.; Wang, H.; Dunn, B.; Kaner, R. B. Design and Mechanisms of Asymmetric Supercapacitors. Chem. Rev. 2018, 118, 9233−9280.
(165) Trasatti, S.; Buzzanca, G. Ruthenium Dioxide: A New Interesting Electrode Material. Solid State Structure and Electrochemical Behaviour. J. Electroanal. Chem. Interfacial Electrochem. 1971, 29, A1−A5.
(166) Hu, C.-C.; Chang, K.-H.; Lin, M.-C.; Wu, Y.-T. Design and Tailoring of the Nanotubular Arrayed Architecture of Hydrous RuO_2 for Next Generation Supercapacitors. Nano Lett. 2006, 6, 2690−2695.
(167) Toupin, M.; Brousse, T.; Bélanger, D. Charge Storage Mechanism of MnO_2 Electrode Used in Aqueous Electrochemical Capacitor. Chem. Mater. 2004, 16, 3184−3190.
(168) Ragupathy, P.; Vasan, H.; Munichandraiah, N. Synthesis and Characterization of Nano-MnO_2 for Electrochemical Supercapacitor Studies. J. Electrochem. Soc. 2008, 155, A34−A40.
(169) Chen, Z.; Augustyn, V.; Wen, J.; Zhang, Y.; Shen, M.; Dunn, B.; Lu, Y. High-Performance Supercapacitors Based on Intertwined CNT/V_2O_5 Nanowire Nanocomposites. Adv. Mater. 2011, 23, 791−795.
(170) Sathiya, M.; Prakash, A.; Ramesha, K.; Tarascon, J. M.; Shukla, A. V_2O_5-Anchored Carbon Nanotubes for Enhanced Electrochemical Energy Storage. J. Am. Chem. Soc. 2011, 133, 16291−16299.
(171) Wang, J.; Polleux, J.; Lim, J.; Dunn, B. Pseudocapacitive Contributions to Electrochemical Energy Storage in TiO_2 (Anatase) Nanoparticles. J. Phys. Chem. C 2007, 111, 14925−14931.
(172) Griffith, K. J.; Forse, A. C.; Griffin, J. M.; Grey, C. P. High-Rate Intercalation without Nanostructuring in Metastable Nb_2O_5 Bronze Phases. J. Am. Chem. Soc. 2016, 138, 8888−8899.
(173) Gogotsi, Y.; Penner, R. M. Energy Storage in Nanomaterials−Capacitive, Pseudocapacitive, or Battery-Like? ACS Nano 2018, 12, 2081−2083.
(174) Conway, B. E. Transition from "Supercapacitor" to "Battery" Behavior in Electrochemical Energy Storage. J. Electrochem. Soc. 1991, 138, 1539−1548.
(175) Lindström, H.; Södergren, S.; Solbrand, A.; Rensmo, H.; Hjelm, J.; Hagfeldt, A.; Lindquist, S.-E. Li^+ Ion Insertion in TiO_2 (Anatase). 2. Voltammetry on Nanoporous Films. J. Phys. Chem. B 1997, 101, 7717−7722.
(176) Brezesinski, T.; Wang, J.; Polleux, J.; Dunn, B.; Tolbert, S. H. Templated Nanocrystal-Based Porous TiO_2 Films for Next-Generation Electrochemical Capacitors. J. Am. Chem. Soc. 2009, 131, 1802−1809.
(177) Liu, T. C.; Pell, W.; Conway, B.; Roberson, S. Behavior of Molybdenum Nitrides as Materials for Electrochemical Capacitors Comparison with Ruthenium Oxide. J. Electrochem. Soc. 1998, 145, 1882−1888.
(178) Cao, A. M.; Hu, J. S.; Liang, H. P.; Wan, L. J. Self-Assembled Vanadium Pentoxide (V_2O_5) Hollow Microspheres from Nanorods and Their Application in Lithium-Ion Batteries. Angew. Chem., Int. Ed. 2005, 44, 4391−4395.
(179) Pan, A.; Wu, H. B.; Yu, L.; Lou, X. W. Template-Free Synthesis of VO_2 Hollow Microspheres with Various Interiors and Their Conversion into V_2O_5 for Lithium-Ion Batteries. Angew. Chem. 2013, 125, 2282−2286.
(180) Su, D.; Wang, G. Single-Crystalline Bilayered V_2O_5 Nanobelts for High-Capacity Sodium-Ion Batteries. ACS Nano 2013, 7, 11218−11226.
(181) Ali, G.; Lee, J. H.; Oh, S. H.; Cho, B. W.; Nam, K.-W.; Chung, K. Y. interfaces Investigation of the Na Intercalation Mechanism into Nanosized V_2O_5/C Composite Cathode Material for Na-Ion Batteries. ACS Appl. Mater. Interfaces 2016, 8, 6032−6039.
(182) Gautam, G. S.; Canepa, P.; Malik, R.; Liu, M.; Persson, K.; Ceder, G. First-Principles Evaluation of Multi-Valent Cation Insertion into Orthorhombic V_2O_5. Chem. Commun. 2015, 51, 13619−13622.
(183) Amatucci, G.; Badway, F.; Singhal, A.; Beaudoin, B.; Skandan, G.; Bowmer, T.; Plitz, I.; Pereira, N.; Chapman, T.; Jaworski, R. Investigation of Yttrium and Polyvalent Ion Intercalation into Nanocrystalline Vanadium Oxide. J. Electrochem. Soc. 2001, 148, A940−A950.
(184) Le, D.; Passerini, S.; Coustier, F.; Guo, J.; Soderstrom, T.; Owens, B.; Smyrl, W. Intercalation of Polyvalent Cations into V_2O_5 Aerogels. Chem. Mater. 1998, 10, 682−684.
(185) Ohzuku, T.; Sawai, K.; Hirai, T. Electrochemistry of L-Niobium Pentoxide a Lithium/Non-Aqueous Cell. J. Power Sources 1987, 19, 287−299.
(186) Kumagai, N.; Koishikawa, Y.; Komaba, S.; Koshiba, N. Thermodynamics and Kinetics of Lithium Intercalation into Nb_2O_5 Electrodes for a 2 V Rechargeable Lithium Battery. J. Electrochem. Soc. 1999, 146, 3203−3210.
(187) Wilkening, M.; Iwaniak, W.; Heine, J.; Epp, V.; Kleinert, A.; Behrens, M.; Nuspl, G.; Bensch, W.; Heitjans, P. Microscopic Li Self-Diffusion Parameters in the Lithiated Anode Material $Li_{4+X}Ti_5O_{12}$ ($0 \leq X \leq 3$) Measured by 7 Li Solid State Nmr. Phys. Chem. Chem. Phys. 2007, 9, 6199−6202.
(188) Liu, Z.; Huang, X. Factors That Affect Activation Energy for Li Diffusion in $LiFePO_4$: A First-Principles Investigation. Solid State Ionics 2010, 181, 907−913.
(189) Sun, W.; Dacek, S. T.; Ong, S. P.; Hautier, G.; Jain, A.; Richards, W. D.; Gamst, A. C.; Persson, K. A.; Ceder, G. The Thermodynamic Scale of Inorganic Crystalline Metastability. Sci. Adv. 2016, 2, No. e1600225.
(190) Kitchaev, D. A.; Lun, Z.; Richards, W. D.; Ji, H.; Clément, R. J.; Balasubramanian, M.; Kwon, D.-H.; Dai, K.; Papp, J. K.; Lei, T.; et al. Design Principles for High Transition Metal Capacity in Disordered Rocksalt Li-Ion Cathodes. Energy Environ. Sci. 2018, 11, 2159−2171.
(191) Fecht, H.; Hellstern, E.; Fu, Z.; Johnson, W. Nanocrystalline Metals Prepared by High-Energy Ball Milling. Metall. Trans. A 1990, 21, 2333−2337.
(192) Kim, J.-J.; Choi, Y.; Suresh, S.; Argon, A. Nanocrystallization During Nanoindentation of a Bulk Amorphous Metal Alloy at Room Temperature. Science 2002, 295, 654−657.
(193) Shi, T.; Xiao, P.; Kwon, D.-H.; Sai Gautam, G.; Chakarawet, K.; Kim, H.; Bo, S.-H.; Ceder, G. Shear-Assisted Formation of Cation-Disordered Rocksalt $NaMO_2$ (M= Fe, Mn). Chem. Mater. 2018, 30, 8811−8821.
(194) Baláž, P.; Achimovičová, M.; Baláž, M.; Billik, P.; Cherkezova-Zheleva, Z.; Criado, J. M.; Delogu, F.; Dutková, E.; Gaffet, E.; Gotor, F. J.; et al. Hallmarks of Mechanochemistry: From Nanoparticles to Technology. Chem. Soc. Rev. 2013, 42, 7571−7637.

DOI: 10.1021/acs.chemrev.9b00405
Chem. Rev. XXXX, XXX, XXX−XXX

(195) Tan, D.; García, F. Main Group Mechanochemistry: From Curiosity to Established Protocols. Chem. Soc. Rev. 2019, 48, 2274−2292.
(196) Boldyreva, E. Mechanochemistry of Inorganic and Organic Systems: What Is Similar, What Is Different? Chem. Soc. Rev. 2013, 42, 7719−7738.
(197) Hara, K. O.; Yamasue, E.; Okumura, H.; Ishihara, K. N. Formation of Metastable Phases by High-Energy Ball Milling in the Ti-O System. J. Phys. Conf. Ser. 2009, 144, 012021.
(198) Freire, M.; Lebedev, O.; Maignan, A.; Jordy, C.; Pralong, V. Nanostructured Li_2MnO_3: A Disordered Rock Salt Type Structure for High Energy Density Li Ion Batteries. J. Mater. Chem. A 2017, 5, 21898−21902.
(199) Sato, K.; Nakayama, M.; Glushenkov, A. M.; Mukai, T.; Hashimoto, Y.; Yamanaka, K.; Yoshimura, M.; Ohta, T.; Yabuuchi, N. Na-Excess Cation-Disordered Rocksalt Oxide: $Na_{1.3}Nb_{0.3}Mn_{0.4}O_2$. Chem. Mater. 2017, 29, 5043−5047.
(200) Rana, J.; Stan, M.; Kloepsch, R.; Li, J.; Schumacher, G.; Welter, E.; Zizak, I.; Banhart, J.; Winter, M. Structural Changes in Li_2MnO_3 Cathode Material for Li-Ion Batteries. Adv. Energy Mater. 2014, 4, 1300998.
(201) Freire, M.; Diaz-Lopez, M.; Bordet, P.; Colin, C.; Lebedev, O.; Kosova, N.; Jordy, C.; Chateigner, D.; Chuvilin, A.; Maignan, A.; Pralong, V. Investigation of the Exceptional Charge Performance of the $0.93Li_{4-X}Mn_2O_5$−$0.07Li_2O$ Composite Cathode for Li-Ion Batteries. J. Mater. Chem. A 2018, 6, 5156−5165.
(202) Yao, Z.; Kim, S.; He, J.; Hegde, V. I.; Wolverton, C. Interplay of Cation and Anion Redox in $Li_4Mn_2O_5$ Cathode Material and Prediction of Improved $Li_4(Mn, M)_2O_5$ Electrodes for Li-Ion Batteries. Sci. Adv. 2018, 4, No. eaao6754.
(203) Diaz-Lopez, M.; Freire, M.; Joly, Y.; Colin, C. V.; Fischer, H. E.; Blanc, N.; Boudet, N.; Pralong, V.; Bordet, P. Local Structure and Lithium Diffusion Pathways in $Li_4Mn_2O_5$ High Capacity Cathode Probed by Total Scattering and Xanes. Chem. Mater. 2018, 30, 3060−3070.
(204) Van der Ven, A.; Ceder, G. Lithium Diffusion Mechanisms in Layered Intercalation Compounds. J. Power Sources 2001, 97, 529−531.
(205) Yabuuchi, N.; Takeuchi, M.; Nakayama, M.; Shiiba, H.; Ogawa, M.; Nakayama, K.; Ohta, T.; Endo, D.; Ozaki, T.; Inamasu, T.; et al. High-Capacity Electrode Materials for Rechargeable Lithium Batteries: Li_3NbO_4-Based System with Cation-Disordered Rocksalt Structure. Proc. Natl. Acad. Sci. U. S. A. 2015, 112, 7650−7655.
(206) Lee, J.; Seo, D.-H.; Balasubramanian, M.; Twu, N.; Li, X.; Ceder, G. A New Class of High Capacity Cation-Disordered Oxides for Rechargeable Lithium Batteries: Li−Ni−Ti−Mo Oxides. Energy Environ. Sci. 2015, 8, 3255−3265.
(207) Yabuuchi, N.; Nakayama, M.; Takeuchi, M.; Komaba, S.; Hashimoto, Y.; Mukai, T.; Shiiba, H.; Sato, K.; Kobayashi, Y.; Nakao, A.; Yonemura, M.; Yamanaka, K.; Mitsuhara, K.; Ohta, T. Origin of Stabilization and Destabilization in Solid-State Redox Reaction of Oxide Ions for Lithium-Ion Batteries. Nat. Commun. 2016, 7, 13814.
(208) Kang, K.; Carlier, D.; Reed, J.; Arroyo, E. M.; Ceder, G.; Croguennec, L.; Delmas, C. Synthesis and Electrochemical Properties of Layered $Li_{0.9}Ni_{0.45}Ti_{0.55}O_2$. Chem. Mater. 2003, 15, 4503−4507.
(209) Yabuuchi, N.; Takeuchi, M.; Komaba, S.; Ichikawa, S.; Ozaki, T.; Inamasu, T. Synthesis and Electrochemical Properties of $Li_{1.3}Nb_{0.3}V_{0.4}O_2$ as a Positive Electrode Material for Rechargeable Lithium Batteries. Chem. Commun. 2016, 52, 2051−2054.
(210) Yabuuchi, N.; Tahara, Y.; Komaba, S.; Kitada, S.; Kajiya, Y. Synthesis and Electrochemical Properties of Li_4MoO_5−NiO Binary System as Positive Electrode Materials for Rechargeable Lithium Batteries. Chem. Mater. 2016, 28, 416−419.
(211) Nakajima, M.; Yabuuchi, N. Lithium-Excess Cation-Disordered Rocksalt-Type Oxide with Nanoscale Phase Segregation: $Li_{1.25}Nb_{0.25}V_{0.5}O_2$. Chem. Mater. 2017, 29, 6927−6935.
(212) Assat, G.; Tarascon, J.-M. Fundamental Understanding and Practical Challenges of Anionic Redox Activity in Li-Ion Batteries. Nat. Energy 2018, 3, 373−386.
(213) Li, B.; Xia, D. Anionic Redox in Rechargeable Lithium Batteries. Adv. Mater. 2017, 29, 1701054.
(214) Richards, W. D.; Dacek, S. T.; Kitchaev, D. A.; Ceder, G. Fluorination of Lithium-Excess Transition Metal Oxide Cathode Materials. Adv. Energy Mater. 2018, 8, 1701533.
(215) Delmas, C.; Brèthes, S.; Ménétrier, M. Ω-Lixv2o5 — a New Electrode Material for Rechargeable Lithium Batteries. J. Power Sources 1991, 34, 113−118.
(216) Twu, N.; Li, X.; Urban, A.; Balasubramanian, M.; Lee, J.; Liu, L.; Ceder, G. Designing New Lithium-Excess Cathode Materials from Percolation Theory: Nanohighways in $Li_xNi_{2-4x/3}Sb_{x/3}O_2$. Nano Lett. 2015, 15, 596−602.
(217) Hong, J.; Lim, H.-D.; Lee, M.; Kim, S.-W.; Kim, H.; Oh, S.-T.; Chung, G.-C.; Kang, K. Critical Role of Oxygen Evolved from Layered Li−Excess Metal Oxides in Lithium Rechargeable Batteries. Chem. Mater. 2012, 24, 2692−2697.
(218) Mohanty, D.; Mazumder, B.; Devaraj, A.; Sefat, A. S.; Huq, A.; David, L. A.; Payzant, E. A.; Li, J.; Wood, D. L.; Daniel, C. Resolving the Degradation Pathways in High-Voltage Oxides for High-Energy-Density Lithium-Ion Batteries; Alternation in Chemistry, Composition and Crystal Structures. Nano Energy 2017, 36, 76−84.
(219) Chen, R.; Ren, S.; Knapp, M.; Wang, D.; Witter, R.; Fichtner, M.; Hahn, H. Disordered Lithium-Rich Oxyfluoride as a Stable Host for Enhanced Li+ Intercalation Storage. Adv. Energy Mater. 2015, 5, 1401814.
(220) Ménétrier, M.; Bains, J.; Croguennec, L.; Flambard, A.; Bekaert, E.; Jordy, C.; Biensan, P.; Delmas, C. Nmr Evidence of Lif Coating Rather Than Fluorine Substitution in Li-$(Ni_{0.425}Mn_{0.425}Co_{0.15})O_2$. J. Solid State Chem. 2008, 181, 3303−3307.
(221) Croguennec, L.; Bains, J.; Ménétrier, M.; Flambard, A.; Bekaert, E.; Jordy, C.; Biensan, P.; Delmas, C. Synthesis of "$Li_{1.1}(Ni_{0.425}Mn_{0.425}Co_{0.15})_{0.9}O_{1.8}F_{0.2}$" Materials by Different Routes: Is There Fluorine Substitution for Oxygen? J. Electrochem. Soc. 2009, 156, A349−A355.
(222) Jouanneau, S.; Dahn, J. R. Influence of Lif Additions on $Li[Ni_XCo_{1-2x}Mn_X]O_2$ Materials: Sintering, Structure, and Lithium Insertion Properties. J. Electrochem. Soc. 2004, 151, A1749−A1754.
(223) Li, D.; Sasaki, Y.; Kobayakawa, K.; Noguchi, H.; Sato, Y. Preparation, Morphology and Electrochemical Characteristics of $LiNi_{1/3}Mn_{1/3}Co_{1/3}O_2$ with Lif Addition. Electrochim. Acta 2006, 52, 643−648.
(224) Min, J. W.; Gim, J.; Song, J.; Ryu, W.-H.; Lee, J.-W.; Kim, Y.-I.; Kim, J.; Im, W. B. Simple, Robust Metal Fluoride Coating on Layered $Li_{1.23}Ni_{0.13}Co_{0.14}Mn_{0.56}O_2$ and Its Effects on Enhanced Electrochemical Properties. Electrochim. Acta 2013, 100, 10−17.
(225) Du, G.; NuLi, Y.; Yang, J.; Wang, J. Fluorine-Doped $LiNi_{0.5}Mn_{1.5}O_4$ for 5v Cathode Materials of Lithium-Ion Battery. Mater. Res. Bull. 2008, 43, 3607−3613.
(226) Song, J. H.; Kapylou, A.; Choi, H. S.; Yu, B. Y.; Matulevich, E.; Kang, S. H. Suppression of Irreversible Capacity Loss in Li-Rich Layered Oxide by Fluorine Doping. J. Power Sources 2016, 313, 65−72.
(227) Zheng, J.; Wu, X.; Yang, Y. Improved Electrochemical Performance of $Li[Li_{0.2}Mn_{0.54}Ni_{0.13}Co_{0.13}]O_2$ Cathode Material by Fluorine Incorporation. Electrochim. Acta 2013, 105, 200−208.
(228) Oh, S.-W.; Park, S.-H.; Kim, J.-H.; Bae, Y. C.; Sun, Y.-K. Improvement of Electrochemical Properties of $LiNi_{0.5}Mn_{1.5}O_4$ Spinel Material by Fluorine Substitution. J. Power Sources 2006, 157, 464−470.
(229) Kang, S. H.; Belharouak, I.; Sun, Y. K.; Amine, K. Effect of Fluorine on the Electrochemical Properties of Layered $Li(Ni_{0.5}Mn_{0.5})$-O_2 Cathode Materials. J. Power Sources 2005, 146, 650−653.
(230) Palacín, M. R.; Le Cras, F.; Seguin, L.; Anne, M.; Chabre, Y.; Tarascon, J. M.; Amatucci, G.; Vaughan, G.; Strobel, P. In Situstructural Study of 4V-Range Lithium Extraction/Insertion in Fluorine-Substituted $LiMn_2O_4$. J. Solid State Chem. 1999, 144, 361−371.
(231) Ren, S.; Chen, R.; Maawad, E.; Dolotko, O.; Guda, A. A.; Shapovalov, V.; Wang, D.; Hahn, H.; Fichtner, M. Improved Voltage

DOI: 10.1021/acs.chemrev.9b00405
Chem. Rev. XXXX, XXX, XXX−XXX

and Cycling for Li^+ Intercalation in High-Capacity Disordered Oxyfluoride Cathodes. Adv. Sci. 2015, 2, 1500128.
(232) Chen, R.; Ren, S.; Yavuz, M.; Guda, A. A.; Shapovalov, V.; Witter, R.; Fichtner, M.; Hahn, H. Li+ Intercalation in Isostructural Li_2VO_3 and Li_2VO_2F with O^{2-} and Mixed O^{2-}/F^- Anions. Phys. Chem. Chem. Phys. 2015, 17, 17288−17295.
(233) Wang, X.; Lin, Y.-C.; Zhou, H.; Omenya, F.; Chu, I.-H.; Karki, K.; Sallis, S.; Rana, J.; Piper, L. F. J.; Chernova, N. A.; et al. Structural Changes in a High-Energy Density VO_2F Cathode Upon Heating and Li Cycling. ACS Appl. Energy Mater. 2018, 1, 4514−4521.
(234) Chen, R.; Ren, S.; Mu, X.; Maawad, E.; Zander, S.; Hempelmann, R.; Hahn, H. High-Performance Low-Temperature Li^+ Intercalation in Disordered Rock-Salt Li−Cr−V Oxyfluorides. ChemElectroChem 2016, 3, 892−895.
(235) Takeda, N.; Hoshino, S.; Xie, L.; Chen, S.; Ikeuchi, I.; Natsui, R.; Nakura, K.; Yabuuchi, N. Reversible Li Storage for Nanosize Cation/Anion-Disordered Rocksalt-Type Oxyfluorides: $LiMoO_2$ − XLiF ($0 \leq X \leq 2$) Binary System. J. Power Sources 2017, 367, 122−129.
(236) Chen, R.; Maawad, E.; Knapp, M.; Ren, S.; Beran, P.; Witter, R.; Hempelmann, R. Lithiation-Driven Structural Transition of VO_2F into Disordered Rock-Salt Li_xVO_2F. RSC Adv. 2016, 6, 65112−65118.
(237) Pralong, V.; Gopal, V.; Caignaert, V.; Duffort, V.; Raveau, B. Lithium-Rich Rock-Salt-Type Vanadate as Energy Storage Cathode: $Li_{2-X}VO_3$. Chem. Mater. 2012, 24, 12−14.
(238) Lun, Z.; Ouyang, B.; Kitchaev, D. A.; Clément, R. J.; Papp, J. K.; Balasubramanian, M.; Tian, Y.; Lei, T.; Shi, T.; McCloskey, B. D.; Lee, J.; Ceder, G. Improved Cycling Performance of Li-Excess Cation-Disordered Cathode Materials Upon Fluorine Substitution. Adv. Energy Mater. 2019, 9, 1802959.
(239) Kim, S.-W.; Pereira, N.; Chernova, N. A.; Omenya, F.; Gao, P.; Whittingham, M. S.; Amatucci, G. G.; Su, D.; Wang, F. Structure Stabilization by Mixed Anions in Oxyfluoride Cathodes for High-Energy Lithium Batteries. ACS Nano 2015, 9, 10076−10084.
(240) Rajput, S.; Pittman, C. U., Jr; Mohan, D. Magnetic Magnetite (Fe_3O_4) Nanoparticle Synthesis and Applications for Lead (Pb^{2+}) and Chromium (Cr^{6+}) Removal from Water. J. Colloid Interface Sci. 2016, 468, 334−346.
(241) Raimondi, F.; Scherer, G. G.; Kötz, R.; Wokaun, A. Nanoparticles in Energy Technology: Examples from Electrochemistry and Catalysis. Angew. Chem., Int. Ed. 2005, 44, 2190−2209.
(242) Zaghib, K.; Nadeau, G.; Kinoshita, K. Effect of Graphite Particle Size on Irreversible Capacity Loss. J. Electrochem. Soc. 2000, 147, 2110−2115.
(243) Kim, H.; Kim, M. G.; Jeong, H. Y.; Nam, H.; Cho, J. A New Coating Method for Alleviating Surface Degradation of Li-$Ni_{0.6}Co_{0.2}Mn_{0.2}O_2$ Cathode Material: Nanoscale Surface Treatment of Primary Particles. Nano Lett. 2015, 15, 2111−2119.
(244) Jung, S. K.; Gwon, H.; Hong, J.; Park, K. Y.; Seo, D. H.; Kim, H.; Hyun, J.; Yang, W.; Kang, K. Understanding the Degradation Mechanisms of $LiNi_{0.5}Co_{0.2}Mn_{0.3}O_2$ Cathode Material in Lithium Ion Batteries. Adv. Energy Mater. 2014, 4, 1300787.
(245) Lin, F.; Markus, I. M.; Nordlund, D.; Weng, T.-C.; Asta, M. D.; Xin, H. L.; Doeff, M. M. Surface Reconstruction and Chemical Evolution of Stoichiometric Layered Cathode Materials for Lithium-Ion Batteries. Nat. Commun. 2014, 5, 3529.
(246) Li, L.; Xu, M.; Yao, Q.; Chen, Z.; Song, L.; Zhang, Z.; Gao, C.; Wang, P.; Yu, Z.; Lai, Y. Alleviating Surface Degradation of Nickel-Rich Layered Oxide Cathode Material by Encapsulating with Nanoscale Li-Ions/Electrons Superionic Conductors Hybrid Membrane for Advanced Li-Ion Batteries. ACS Appl. Mater. Interfaces 2016, 8, 30879−30889.
(247) Luo, K.; Roberts, M. R.; Hao, R.; Guerrini, N.; Pickup, D. M.; Liu, Y.-S.; Edström, K.; Guo, J.; Chadwick, A. V.; Duda, L. C.; Bruce, P. G. Charge-Compensation in 3d-Transition-Metal-Oxide Intercalation Cathodes through the Generation of Localized Electron Holes on Oxygen. Nat. Chem. 2016, 8, 684−691.
(248) Luo, K.; Roberts, M. R.; Guerrini, N.; Tapia-Ruiz, N.; Hao, R.; Massel, F.; Pickup, D. M.; Ramos, S.; Liu, Y.-S.; Guo, J.; et al. Anion Redox Chemistry in the Cobalt Free 3d Transition Metal Oxide Intercalation Electrode $Li[Li_{0.2}Ni_{0.2}Mn_{0.6}]O_2$. J. Am. Chem. Soc. 2016, 138, 11211−11218.
(249) Hong, J.; Gwon, H.; Jung, S.-K.; Ku, K.; Kang, K. Review—Lithium-Excess Layered Cathodes for Lithium Rechargeable Batteries. J. Electrochem. Soc. 2015, 162, A2447−A2467.
(250) Renfrew, S. E.; McCloskey, B. D. Residual Lithium Carbonate Predominantly Accounts for First Cycle Co2 and Co Outgassing of Li-Stoichiometric and Li-Rich Layered Transition-Metal Oxides. J. Am. Chem. Soc. 2017, 139, 17853−17860.
(251) Kim, J.-H.; Pieczonka, N. P. W.; Yang, L. Challenges and Approaches for High-Voltage Spinel Lithium-Ion Batteries. ChemPhysChem 2014, 15, 1940−1954.
(252) Ochida, M.; Domi, Y.; Doi, T.; Tsubouchi, S.; Nakagawa, H.; Yamanaka, T.; Abe, T.; Ogumi, Z. Influence of Manganese Dissolution on the Degradation of Surface Films on Edge Plane Graphite Negative-Electrodes in Lithium-Ion Batteries. J. Electrochem. Soc. 2012, 159, A961−A966.
(253) Gallus, D. R.; Schmitz, R.; Wagner, R.; Hoffmann, B.; Nowak, S.; Cekic-Laskovic, I.; Schmitz, R. W.; Winter, M. The Influence of Different Conducting Salts on the Metal Dissolution and Capacity Fading of Ncm Cathode Material. Electrochim. Acta 2014, 134, 393−398.
(254) Pieczonka, N. P. W.; Liu, Z.; Lu, P.; Olson, K. L.; Moote, J.; Powell, B. R.; Kim, J.-H. Understanding Transition-Metal Dissolution Behavior in $LiNi_{0.5}Mn_{1.5}O_4$ High-Voltage Spinel for Lithium Ion Batteries. J. Phys. Chem. C 2013, 117, 15947−15957.
(255) Krtil, P.; Kavan, L.; Novák, P. Oxidation of Acetonitrile-Based Electrolyte Solutions at High Potentials: An in Situ Fourier Transform Infrared Spectroscopy Study. J. Electrochem. Soc. 1993, 140, 3390−3395.
(256) Fan, X.; Chen, L.; Borodin, O.; Ji, X.; Chen, J.; Hou, S.; Deng, T.; Zheng, J.; Yang, C.; Liou, S.-C.; et al. Non-Flammable Electrolyte Enables Li-Metal Batteries with Aggressive Cathode Chemistries. Nat. Nanotechnol. 2018, 13, 715−722.
(257) Lee, S.; Kwon, G.; Ku, K.; Yoon, K.; Jung, S.-K.; Lim, H.-D.; Kang, K. Recent Progress in Organic Electrodes for Li and Na Rechargeable Batteries. Adv. Mater. 2018, 30, 1704682.
(258) Courtney, I. A.; McKinnon, W. R.; Dahn, J. R. On the Aggregation of Tin in Sno Composite Glasses Caused by the Reversible Reaction with Lithium. J. Electrochem. Soc. 1999, 146, 59−68.
(259) Guo, B.; Shu, J.; Tang, K.; Bai, Y.; Wang, Z.; Chen, L. Nano-Sn/Hard Carbon Composite Anode Material with High-Initial Coulombic Efficiency. J. Power Sources 2008, 177, 205−210.
(260) Wang, F.; Yu, H.-C.; Chen, M.-H.; Wu, L.; Pereira, N.; Thornton, K.; Van der Ven, A.; Zhu, Y.; Amatucci, G. G.; Graetz, J. Tracking Lithium Transport and Electrochemical Reactions in Nanoparticles. Nat. Commun. 2012, 3, 1201.
(261) Zhu, Z.; Wang, S.; Du, J.; Jin, Q.; Zhang, T.; Cheng, F.; Chen, J. Ultrasmall Sn Nanoparticles Embedded in Nitrogen-Doped Porous Carbon as High-Performance Anode for Lithium-Ion Batteries. Nano Lett. 2014, 14, 153−157.
(262) Hotze, E. M.; Phenrat, T.; Lowry, G. V. Nanoparticle Aggregation: Challenges to Understanding Transport and Reactivity in the Environment. J. Environ. Qual. 2010, 39, 1909−1924.
(263) Verwey, E. J. W.; Overbeek, J. T. G. Theory of the Stability of Lyophobic Colloids: The Interaction of Sol Particles Having an Electric Double Layer; Elsevier: New York, 1948.
(264) Derjaguin, B.; Landau, L. Theory of the Stability of Strongly Charged Lyophobic Sols and of the Adhesion of Strongly Charged Particles in Solution of Electrolytes. Acta Physicochim. URSS 1941, 14, 633−662.
(265) Hahn, M. W.; Abadzic, D.; O'Melia, C. R. Aquasols: On the Role of Secondary Minima. Environ. Sci. Technol. 2004, 38, 5915−5924.
(266) Chung, S.-Y.; Choi, S.-Y.; Kim, T.-H.; Lee, S. Surface-Orientation-Dependent Distribution of Subsurface Cation-Exchange

DOI: 10.1021/acs.chemrev.9b00405
Chem. Rev. XXXX, XXX, XXX−XXX

Defects in Olivine-Phosphate Nanocrystals. ACS Nano 2015, 9, 850−859.
(267) Park, J.; Lee, E.; Hwang, N.-M.; Kang, M.; Kim, S. C.; Hwang, Y.; Park, J.-G.; Noh, H.-J.; Kim, J.-Y.; Park, J.-H.; et al. One-Nanometer-Scale Size-Controlled Synthesis of Monodisperse Magnetic Iron Oxide Nanoparticles. Angew. Chem. 2005, 117, 2932−2937.
(268) Kim, B. H.; Lee, N.; Kim, H.; An, K.; Park, Y. I.; Choi, Y.; Shin, K.; Lee, Y.; Kwon, S. G.; Na, H. B.; et al. Large-Scale Synthesis of Uniform and Extremely Small-Sized Iron Oxide Nanoparticles for High-Resolution T1Magnetic Resonance Imaging Contrast Agents. J. Am. Chem. Soc. 2011, 133, 12624−12631.
(269) Liu, N.; Lu, Z.; Zhao, J.; McDowell, M. T.; Lee, H.-W.; Zhao, W.; Cui, Y. A Pomegranate-Inspired Nanoscale Design for Large-Volume-Change Lithium Battery Anodes. Nat. Nanotechnol. 2014, 9, 187.
(270) Abu-Lebdeh, Y.; Davidson, I. Nanotechnology for Lithium-Ion Batteries; Springer Science & Business Media, 2012.
(271) Sun, Y.; Liu, N.; Cui, Y. Promises and Challenges of Nanomaterials for Lithium-Based Rechargeable Batteries. Nat. Energy 2016, 1, 16071.
(272) Jung, D. S.; Hwang, T. H.; Park, S. B.; Choi, J. W. Spray Drying Method for Large-Scale and High-Performance Silicon Negative Electrodes in Li-Ion Batteries. Nano Lett. 2013, 13, 2092−2097.
(273) Jin, Y.; Zhu, B.; Lu, Z.; Liu, N.; Zhu, J. Challenges and Recent Progress in the Development of Si Anodes for Lithium-Ion Battery. Adv. Energy Mater. 2017, 7, 1700715.
(274) Lin, D.; Lu, Z.; Hsu, P.-C.; Lee, H. R.; Liu, N.; Zhao, J.; Wang, H.; Liu, C.; Cui, Y. A High Tap Density Secondary Silicon Particle Anode Fabricated by Scalable Mechanical Pressing for Lithium-Ion Batteries. Energy Environ. Sci. 2015, 8, 2371−2376.
(275) Kim, S.-O.; Manthiram, A. A Facile, Low-Cost Synthesis of High-Performance Silicon-Based Composite Anodes with High Tap Density for Lithium-Ion Batteries. J. Mater. Chem. A 2015, 3, 2399−2406.
(276) Zheng, H.; Li, J.; Song, X.; Liu, G.; Battaglia, V. S. A Comprehensive Understanding of Electrode Thickness Effects on the Electrochemical Performances of Li-Ion Battery Cathodes. Electrochim. Acta 2012, 71, 258−265.
(277) Du, Z.; Wood, D. L.; Daniel, C.; Kalnaus, S.; Li, J. Understanding Limiting Factors in Thick Electrode Performance as Applied to High Energy Density Li-Ion Batteries. J. Appl. Electrochem. 2017, 47, 405−415.
(278) Zheng, H.; Tan, L.; Liu, G.; Song, X.; Battaglia, V. S. Calendering Effects on the Physical and Electrochemical Properties of $Li[Ni_{1/3}Mn_{1/3}Co_{1/3}]O_2$ Cathode. J. Power Sources 2012, 208, 52−57.
(279) Berckmans, G.; Messagie, M.; Smekens, J.; Omar, N.; Vanhaverbeke, L.; Van Mierlo, J. Cost Projection of State of the Art Lithium-Ion Batteries for Electric Vehicles up to 2030. Energies 2017, 10, 1314.
(280) Xing, Z.; Ju, Z.; Yang, J.; Xu, H.; Qian, Y. One-Step Hydrothermal Synthesis of $ZnFe_2O_4$ Nano-Octahedrons as a High Capacity Anode Material for Li-Ion Batteries. Nano Res. 2012, 5, 477−485.
(281) Hsu, K.-F.; Tsay, S.-Y.; Hwang, B.-J. Synthesis and Characterization of Nano-Sized Lifepo4 Cathode Materials Prepared by a Citric Acid-Based Sol−Gel Route. J. Mater. Chem. 2004, 14, 2690−2695.
(282) Tang, W.; Wang, X. J.; Hou, Y. Y.; Li, L. L.; Sun, H.; Zhu, Y. S.; Bai, Y.; Wu, Y. P.; Zhu, K.; van Ree, T. Nano $LiMn_2O_4$ as Cathode Material of High Rate Capability for Lithium Ion Batteries. J. Power Sources 2012, 198, 308−311.
(283) Sharma, N.; Shaju, K. M.; Subba Rao, G. V.; Chowdari, B. V. R. Sol−Gel Derived Nano-Crystalline $CaSnO_3$ as High Capacity Anode Material for Li-Ion Batteries. Electrochem. Commun. 2002, 4, 947−952.
(284) Fan, X.; Zhu, Y.; Luo, C.; Suo, L.; Lin, Y.; Gao, T.; Xu, K.; Wang, C. Pomegranate-Structured Conversion-Reaction Cathode with a Built-in Li Source for High-Energy Li-Ion Batteries. ACS Nano 2016, 10, 5567−5577.
(285) Park, J.; An, K.; Hwang, Y.; Park, J.-G.; Noh, H.-J.; Kim, J.-Y.; Park, J.-H.; Hwang, N.-M.; Hyeon, T. Ultra-Large-Scale Syntheses of Monodisperse Nanocrystals. Nat. Mater. 2004, 3, 891−895.
(286) Pokropivny, V. V.; Skorokhod, V. V. Classification of Nanostructures by Dimensionality and Concept of Surface Forms Engineering in Nanomaterial Science. Mater. Sci. Eng., C 2007, 27, 990−993.
(287) Tiwari, J. N.; Tiwari, R. N.; Kim, K. S. Zero-Dimensional, One-Dimensional, Two-Dimensional and Three-Dimensional Nanostructured Materials for Advanced Electrochemical Energy Devices. Prog. Mater. Sci. 2012, 57, 724−803.
(288) Chen, R.; Zhao, T.; Zhang, X.; Li, L.; Wu, F. Advanced Cathode Materials for Lithium-Ion Batteries Using Nanoarchitectonics. Nanoscale Horiz 2016, 1, 423−444.
(289) Lim, J.; Choi, E.; Mathew, V.; Kim, D.; Ahn, D.; Gim, J.; Kang, S.-H.; Kim, J. Enhanced High-Rate Performance of $Li_4Ti_5O_{12}$ Nanoparticles for Rechargeable Li-Ion Batteries. J. Electrochem. Soc. 2011, 158, A275−A280.
(290) Bai, P.; Cogswell, D. A.; Bazant, M. Z. Suppression of Phase Separation in Lifepo4 Nanoparticles During Battery Discharge. Nano Lett. 2011, 11, 4890−4896.
(291) Park, M.-H.; Kim, M. G.; Joo, J.; Kim, K.; Kim, J.; Ahn, S.; Cui, Y.; Cho, J. Silicon Nanotube Battery Anodes. Nano Lett. 2009, 9, 3844−3847.
(292) Cui, L.-F.; Ruffo, R.; Chan, C. K.; Peng, H.; Cui, Y. Crystalline-Amorphous Core−Shell Silicon Nanowires for High Capacity and High Current Battery Electrodes. Nano Lett. 2009, 9, 491−495.
(293) Ding, Y.-L.; Xie, J.; Cao, G.-S.; Zhu, T.-J.; Yu, H.-M.; Zhao, X.-B. Single-Crystalline Limn2o4 Nanotubes Synthesized Via Template-Engaged Reaction as Cathodes for High-Power Lithium Ion Batteries. Adv. Funct. Mater. 2011, 21, 348−355.
(294) Peng, L.; Zhu, Y.; Chen, D.; Ruoff, R. S.; Yu, G. Two-Dimensional Materials for Beyond-Lithium-Ion Batteries. Adv. Energy Mater. 2016, 6, 1600025.
(295) Zhao, Y.; Peng, L.; Liu, B.; Yu, G. Single-Crystalline $LiFePO_4$ Nanosheets for High-Rate Li-Ion Batteries. Nano Lett. 2014, 14, 2849−2853.
(296) Wang, L.; He, X.; Sun, W.; Wang, J.; Li, Y.; Fan, S. Crystal Orientation Tuning of Lifepo4 Nanoplates for High Rate Lithium Battery Cathode Materials. Nano Lett. 2012, 12, 5632−5636.
(297) Kim, H.; Lim, H.-D.; Kim, S.-W.; Hong, J.; Seo, D.-H.; Kim, D.-C.; Jeon, S.; Park, S.; Kang, K. Scalable Functionalized Graphene Nano-Platelets as Tunable Cathodes for High-Performance Lithium Rechargeable Batteries. Sci. Rep. 2013, 3, 1506.
(298) Hu, Z.; Wang, L.; Zhang, K.; Wang, J.; Cheng, F.; Tao, Z.; Chen, J. MoS_2 Nanoflowers with Expanded Interlayers as High-Performance Anodes for Sodium-Ion Batteries. Angew. Chem., Int. Ed. 2014, 53, 12794−12798.
(299) Yue, Q.; Jiang, H.; Hu, Y.; Jia, G.; Li, C. Mesoporous Single-Crystalline V_2O_5 Nanorods Assembled into Hollow Microspheres as Cathode Materials for High-Rate and Long-Life Lithium-Ion Batteries. Chem. Commun. 2014, 50, 13362−13365.
(300) Wang, L.; Zhou, F.; Meng, Y. S.; Ceder, G. First-Principles Study of Surface Properties of $LiFePO_4$: Surface Energy, Structure, Wulff Shape, and Surface Redox Potential. Phys. Rev. B: Condens. Matter Mater. Phys. 2007, 76, 165435.
(301) Kim, J.-S.; Kim, K.; Cho, W.; Shin, W. H.; Kanno, R.; Choi, J. W. A Truncated Manganese Spinel Cathode for Excellent Power and Lifetime in Lithium-Ion Batteries. Nano Lett. 2012, 12, 6358−6365.
(302) Hosono, E.; Kudo, T.; Honma, I.; Matsuda, H.; Zhou, H. Synthesis of Single Crystalline Spinel $LiMn_2O_4$ Nanowires for a Lithium Ion Battery with High Power Density. Nano Lett. 2009, 9, 1045−1051.
(303) Hirayama, M.; Ido, H.; Kim, K.; Cho, W.; Tamura, K.; Mizuki, J. i.; Kanno, R. Dynamic Structural Changes at $LiMn_2O_4$/Electrolyte

DOI: 10.1021/acs.chemrev.9b00405
Chem. Rev. XXXX, XXX, XXX−XXX

Interface During Lithium Battery Reaction. J. Am. Chem. Soc. 2010, 132, 15268−15276.
(304) Furushima, Y.; Yanagisawa, C.; Nakagawa, T.; Aoki, Y.; Muraki, N. Thermal Stability and Kinetics of Delithiated $LiCoO_2$. J. Power Sources 2011, 196, 2260−2263.
(305) Sharifi-Asl, S.; Soto, F. A.; Nie, A.; Yuan, Y.; Asayesh-Ardakani, H.; Foroozan, T.; Yurkiv, V.; Song, B.; Mashayek, F.; Klie, R. F.; et al. Facet-Dependent Thermal Instability in $LiCoO_2$. Nano Lett. 2017, 17, 2165−2171.
(306) Gleiter, H. Nanostructured Materials: Basic Concepts and Microstructure. Acta Mater. 2000, 48, 1−29.
(307) Darling, K. A.; VanLeeuwen, B. K.; Koch, C. C.; Scattergood, R. O. Thermal Stability of Nanocrystalline Fe−Zr Alloys. Mater. Sci. Eng., A 2010, 527, 3572−3580.
(308) Millett, P. C.; Selvam, R. P.; Saxena, A. Stabilizing Nanocrystalline Materials with Dopants. Acta Mater. 2007, 55, 2329−2336.
(309) Krill, C. E.; Ehrhardt, H.; Birringer, R. Thermodynamic Stabilization of Nanocrystallinity. Z. Metallkd. 2005, 96, 1134−1141.
(310) Mayr, S. G.; Bedorf, D. Stabilization of Cu Nanostructures by Grain Boundary Doping with Bi: Experiment Versus Molecular Dynamics Simulation. Phys. Rev. B: Condens. Matter Mater. Phys. 2007, 76, 024111.
(311) Chen, K.-S.; Xu, R.; Luu, N. S.; Secor, E. B.; Hamamoto, K.; Li, Q.; Kim, S.; Sangwan, V. K.; Balla, I.; Guiney, L. M.; et al. Comprehensive Enhancement of Nanostructured Lithium-Ion Battery Cathode Materials Via Conformal Graphene Dispersion. Nano Lett. 2017, 17, 2539−2546.
(312) Oh, S. W.; Myung, S.-T.; Oh, S.-M.; Oh, K. H.; Amine, K.; Scrosati, B.; Sun, Y.-K. Double Carbon Coating of $LiFePO_4$ as High Rate Electrode for Rechargeable Lithium Batteries. Adv. Mater. 2010, 22, 4842−4845.
(313) Chen, H. M.; Chen, C. K.; Liu, R.-S.; Zhang, L.; Zhang, J.; Wilkinson, D. P. Nano-Architecture and Material Designs for Water Splitting Photoelectrodes. Chem. Soc. Rev. 2012, 41, 5654−5671.
(314) Wang, Z. L.; Wu, W. Nanotechnology-Enabled Energy Harvesting for Self-Powered Micro-/Nanosystems. Angew. Chem., Int. Ed. 2012, 51, 11700−11721.
(315) Qi, Y.; McAlpine, M. C. Nanotechnology-Enabled Flexible and Biocompatible Energy Harvesting. Energy Environ. Sci. 2010, 3, 1275−1285.
(316) Joy, J.; Mathew, J.; George, S. C. Nanomaterials for Photoelectrochemical Water Splitting − Review. Int. J. Hydrogen Energy 2018, 43, 4804−4817.
(317) Lee, S.-W.; Kim, K.-S.; Moon, H.-S.; Kim, H.-J.; Cho, B.-W.; Cho, W.-I.; Ju, J.-B.; Park, J.-W. Electrochemical Characteristics of Al_2O_3-Coated Lithium Manganese Spinel as a Cathode Material for a Lithium Secondary Battery. J. Power Sources 2004, 126, 150−155.
(318) Zhu, G.-N.; Liu, H.-J.; Zhuang, J.-H.; Wang, C.-X.; Wang, Y.-G.; Xia, Y.-Y. Carbon-Coated Nano-Sized $Li_4Ti_5O_{12}$ Nanoporous Micro-Sphere as Anode Material for High-Rate Lithium-Ion Batteries. Energy Environ. Sci. 2011, 4, 4016−4022.
(319) Zhou, G.; Wang, D.-W.; Li, F.; Zhang, L.; Li, N.; Wu, Z.-S.; Wen, L.; Lu, G. Q.; Cheng, H.-M. Graphene-Wrapped Fe_3O_4 Anode Material with Improved Reversible Capacity and Cyclic Stability for Lithium Ion Batteries. Chem. Mater. 2010, 22, 5306−5313.
(320) Wu, S.; Xu, R.; Lu, M.; Ge, R.; Iocozzia, J.; Han, C.; Jiang, B.; Lin, Z. Graphene-Containing Nanomaterials for Lithium-Ion Batteries. Adv. Energy Mater. 2015, 5, 1500400.
(321) Chen, L.; Wang, K.; Xie, X.; Xie, J. Effect of Vinylene Carbonate (VC) as Electrolyte Additive on Electrochemical Performance of Si Film Anode for Lithium Ion Batteries. J. Power Sources 2007, 174, 538−543.
(322) Zhang, S. S. A Review on Electrolyte Additives for Lithium-Ion Batteries. J. Power Sources 2006, 162, 1379−1394.
(323) Xu, M.; Liu, Y.; Li, B.; Li, W.; Li, X.; Hu, S. Tris (Pentafluorophenyl) Phosphine: An Electrolyte Additive for High Voltage Li-Ion Batteries. Electrochem. Commun. 2012, 18, 123−126.
(324) Chen, Z.; Amine, K. Bifunctional Electrolyte Additive for Lithium-Ion Batteries. Electrochem. Commun. 2007, 9, 703−707.
(325) Wu, F.; Lee, J. T.; Nitta, N.; Kim, H.; Borodin, O.; Yushin, G. Lithium Iodide as a Promising Electrolyte Additive for Lithium−Sulfur Batteries: Mechanisms of Performance Enhancement. Adv. Mater. 2015, 27, 101−108.
(326) Yang, Y.; Yu, G.; Cha, J. J.; Wu, H.; Vosgueritchian, M.; Yao, Y.; Bao, Z.; Cui, Y. Improving the Performance of Lithium−Sulfur Batteries by Conductive Polymer Coating. ACS Nano 2011, 5, 9187−9193.
(327) Ji, X.; Lee, K. T.; Nazar, L. F. A Highly Ordered Nanostructured Carbon−Sulphur Cathode for Lithium−Sulphur Batteries. Nat. Mater. 2009, 8, 500−506.
(328) Wang, Y.; Yi, J.; Xia, Y. Recent Progress in Aqueous Lithium-Ion Batteries. Adv. Energy Mater. 2012, 2, 830−840.
(329) Tang, W.; Liu, L.; Zhu, Y.; Sun, H.; Wu, Y.; Zhu, K. An Aqueous Rechargeable Lithium Battery of Excellent Rate Capability Based on a Nanocomposite of MoO_3 Coated with Ppy and $LiMn_2O_4$. Energy Environ. Sci. 2012, 5, 6909−6913.
(330) Suo, L.; Borodin, O.; Gao, T.; Olguin, M.; Ho, J.; Fan, X.; Luo, C.; Wang, C.; Xu, K. Water-in-Salt" Electrolyte Enables High-Voltage Aqueous Lithium-Ion Chemistries. Science 2015, 350, 938−943.
(331) Li, Y.; Yan, K.; Lee, H.-W.; Lu, Z.; Liu, N.; Cui, Y. Growth of Conformal Graphene Cages on Micrometre-Sized Silicon Particles as Stable Battery Anodes. Nat. Energy 2016, 1, 15029.
(332) Lee, W. J.; Hwang, T. H.; Hwang, J. O.; Kim, H. W.; Lim, J.; Jeong, H. Y.; Shim, J.; Han, T. H.; Kim, J. Y.; Choi, J. W.; et al. N-Doped Graphitic Self-Encapsulation for High Performance Silicon Anodes in Lithium-Ion Batteries. Energy Environ. Sci. 2014, 7, 621−626.
(333) Wu, Z.-S.; Ren, W.; Wen, L.; Gao, L.; Zhao, J.; Chen, Z.; Zhou, G.; Li, F.; Cheng, H.-M. Graphene Anchored with Co_3O_4 Nanoparticles as Anode of Lithium Ion Batteries with Enhanced Reversible Capacity and Cyclic Performance. ACS Nano 2010, 4, 3187−3194.
(334) Li, N.; Jin, S. X.; Liao, Q. Y.; Wang, C. X. Zno Anchored on Vertically Aligned Graphene: Binder-Free Anode Materials for Lithium-Ion Batteries. ACS Appl. Mater. Interfaces 2014, 6, 20590−20596.
(335) Jian, Z.; Zhao, B.; Liu, P.; Li, F.; Zheng, M.; Chen, M.; Shi, Y.; Zhou, H. Fe_2O_3 Nanocrystals Anchored onto Graphene Nanosheets as the Anode Material for Low-Cost Sodium-Ion Batteries. Chem. Commun. 2014, 50, 1215−1217.
(336) Noh, M.; Kwon, Y.; Lee, H.; Cho, J.; Kim, Y.; Kim, M. G. Amorphous Carbon-Coated Tin Anode Material for Lithium Secondary Battery. Chem. Mater. 2005, 17, 1926−1929.
(337) Rahman, M. M.; Wang, J.-Z.; Hassan, M. F.; Wexler, D.; Liu, H. K. Amorphous Carbon Coated High Grain Boundary Density Dual Phase $Li_4Ti_5O_{12}$-TiO_2: A Nanocomposite Anode Material for Li-Ion Batteries. Adv. Energy Mater. 2011, 1, 212−220.
(338) Ng, S. H.; Wang, J.; Wexler, D.; Chew, S. Y.; Liu, H. K. Amorphous Carbon-Coated Silicon Nanocomposites: A Low-Temperature Synthesis Via Spray Pyrolysis and Their Application as High-Capacity Anodes for Lithium-Ion Batteries. J. Phys. Chem. C 2007, 111, 11131−11138.
(339) Liu, H.; Li, W.; Shen, D.; Zhao, D.; Wang, G. Graphitic Carbon Conformal Coating of Mesoporous TiO_2 Hollow Spheres for High-Performance Lithium Ion Battery Anodes. J. Am. Chem. Soc. 2015, 137, 13161−13166.
(340) Fan, Y.; Yang, Z.; Hua, W.; Liu, D.; Tao, T.; Rahman, M. M.; Lei, W.; Huang, S.; Chen, Y. Functionalized Boron Nitride Nanosheets/Graphene Interlayer for Fast and Long-Life Lithium−Sulfur Batteries. Adv. Energy Mater. 2017, 7, 1602380.
(341) Kim, Y.; Koo, D.; Ha, S.; Jung, S. C.; Yim, T.; Kim, H.; Oh, S. K.; Kim, D.-M.; Choi, A.; Kang, Y.; et al. Two-Dimensional Phosphorene-Derived Protective Layers on a Lithium Metal Anode for Lithium-Oxygen Batteries. ACS Nano 2018, 12, 4419−4430.

DOI: 10.1021/acs.chemrev.9b00405
Chem. Rev. XXXX, XXX, XXX−XXX

(342) Cho, J.; Kim, Y. J.; Park, B. Novel Licoo2 Cathode Material with Al_2O_3 Coating for a Li Ion Cell. Chem. Mater. 2000, 12, 3788−3791.
(343) Shim, J.-H.; Lee, S.; Park, S. S. Effects of Mgo Coating on the Structural and Electrochemical Characteristics of $LiCoO_2$ as Cathode Materials for Lithium Ion Battery. Chem. Mater. 2014, 26, 2537−2543.
(344) Gnanaraj, J. S.; Pol, V. G.; Gedanken, A.; Aurbach, D. Improving the High-Temperature Performance of $LiMn_2O_4$ Spinel Electrodes by Coating the Active Mass with MgO Via a Sonochemical Method. Electrochem. Commun. 2003, 5, 940−945.
(345) Hu, S.-K.; Cheng, G.-H.; Cheng, M.-Y.; Hwang, B.-J.; Santhanam, R. Cycle Life Improvement of ZrO_2-Coated Spherical $LiNi_{1/3}Co_{1/3}Mn_{1/3}O_2$ Cathode Material for Lithium Ion Batteries. J. Power Sources 2009, 188, 564−569.
(346) Lu, J.; Peng, Q.; Wang, W.; Nan, C.; Li, L.; Li, Y. Nanoscale Coating of $LiMO_2$ (M = Ni, Co, Mn) Nanobelts with Li^+-Conductive Li_2TiO_3: Toward Better Rate Capabilities for Li-Ion Batteries. J. Am. Chem. Soc. 2013, 135, 1649−1652.
(347) Zhao, Y.; Li, X.; Yan, B.; Li, D.; Lawes, S.; Sun, X. Significant Impact of 2d Graphene Nanosheets on Large Volume Change Tin-Based Anodes in Lithium-Ion Batteries: A Review. J. Power Sources 2015, 274, 869−884.
(348) Raccichini, R.; Varzi, A.; Passerini, S.; Scrosati, B. The Role of Graphene for Electrochemical Energy Storage. Nat. Mater. 2015, 14, 271−279.
(349) Xu, M.; Liang, T.; Shi, M.; Chen, H. Graphene-Like Two-Dimensional Materials. Chem. Rev. 2013, 113, 3766−3798.
(350) Yan, K.; Lee, H.-W.; Gao, T.; Zheng, G.; Yao, H.; Wang, H.; Lu, Z.; Zhou, Y.; Liang, Z.; Liu, Z.; et al. Ultrathin Two-Dimensional Atomic Crystals as Stable Interfacial Layer for Improvement of Lithium Metal Anode. Nano Lett. 2014, 14, 6016−6022.
(351) Kucinskis, G.; Bajars, G.; Kleperis, J. Graphene in Lithium Ion Battery Cathode Materials: A Review. J. Power Sources 2013, 240, 66−79.
(352) Li, H.; Tay, R. Y.; Tsang, S. H.; Liu, W.; Teo, E. H. T. Reduced Graphene Oxide/Boron Nitride Composite Film as a Novel Binder-Free Anode for Lithium Ion Batteries with Enhanced Performances. Electrochim. Acta 2015, 166, 197−205.
(353) Gaberscek, M.; Moskon, J.; Erjavec, B.; Dominko, R.; Jamnik, J. The Importance of Interphase Contacts in Li Ion Electrodes: The Meaning of the High-Frequency Impedance Arc. Electrochem. Solid-State Lett. 2008, 11, A170−A174.
(354) Jung, H.-G.; Oh, S. W.; Ce, J.; Jayaprakash, N.; Sun, Y.-K. Mesoporous TiO_2 Nano Networks: Anode for High Power Lithium Battery Applications. Electrochem. Commun. 2009, 11, 756−759.
(355) Bae, C.-J.; Erdonmez, C. K.; Halloran, J. W.; Chiang, Y.-M. Design of Battery Electrodes with Dual-Scale Porosity to Minimize Tortuosity and Maximize Performance. Adv. Mater. 2013, 25, 1254−1258.
(356) Zhang, W.-M.; Wu, X.-L.; Hu, J.-S.; Guo, Y.-G.; Wan, L.-J. Carbon Coated Fe_3O_4 Nanospindles as a Superior Anode Material for Lithium-Ion Batteries. Adv. Funct. Mater. 2008, 18, 3941−3946.
(357) Li, H.; Zhou, H. Enhancing the Performances of Li-Ion Batteries by Carbon-Coating: Present and Future. Chem. Commun. 2012, 48, 1201−1217.
(358) Cui, L.-F.; Hu, L.; Choi, J. W.; Cui, Y. Light-Weight Free-Standing Carbon Nanotube-Silicon Films for Anodes of Lithium Ion Batteries. ACS Nano 2010, 4, 3671−3678.
(359) Bhuvaneswari, M. S.; Bramnik, N. N.; Ensling, D.; Ehrenberg, H.; Jaegermann, W. Synthesis and Characterization of Carbon Nano Fiber/Lifepo4 Composites for Li-Ion Batteries. J. Power Sources 2008, 180, 553−560.
(360) Zhu, X.; Zhu, Y.; Murali, S.; Stoller, M. D.; Ruoff, R. S. Nanostructured Reduced Graphene Oxide/Fe_2O_3 Composite as a High-Performance Anode Material for Lithium Ion Batteries. ACS Nano 2011, 5, 3333−3338.
(361) Zhou, X.; Wang, F.; Zhu, Y.; Liu, Z. Graphene Modified $LiFePO_4$ Cathode Materials for High Power Lithium Ion Batteries. J. Mater. Chem. 2011, 21, 3353−3358.
(362) Taberna, P. L.; Mitra, S.; Poizot, P.; Simon, P.; Tarascon, J. M. High Rate Capabilities Fe_3O_4-Based Cu Nano-Architectured Electrodes for Lithium-Ion Battery Applications. Nat. Mater. 2006, 5, 567−573.
(363) Chan, C. K.; Zhang, X. F.; Cui, Y. High Capacity Li Ion Battery Anodes Using Ge Nanowires. Nano Lett. 2008, 8, 307−309.
(364) Zhang, H.; Yu, X.; Braun, P. V. Three-Dimensional Bicontinuous Ultrafast-Charge and -Discharge Bulk Battery Electrodes. Nat. Nanotechnol. 2011, 6, 277−281.
(365) Wu, M.-S.; Liao, T.-L.; Wang, Y.-Y.; Wan, C.-C. Assessment of the Wettability of Porous Electrodes for Lithium-Ion Batteries. J. Appl. Electrochem. 2004, 34, 797−805.
(366) Liu, J.; Li, Y.; Huang, X.; Ding, R.; Hu, Y.; Jiang, J.; Liao, L. Direct Growth of SnO_2 Nanorod Array Electrodes for Lithium-Ion Batteries. J. Mater. Chem. 2009, 19, 1859−1864.
(367) Sun, C.; Rajasekhara, S.; Goodenough, J. B.; Zhou, F. Monodisperse Porous Lifepo4Microspheres for a High Power Li-Ion Battery Cathode. J. Am. Chem. Soc. 2011, 133, 2132−2135.
(368) Xiao, Q.; Fan, Y.; Wang, X.; Susantyoko, R. A.; Zhang, Q. A Multilayer Si/CNT Coaxial Nanofiber LIB Anode with a High Areal Capacity. Energy Environ. Sci. 2014, 7, 655−661.
(369) Yang, J.; Wang, J.; Wang, D.; Li, X.; Geng, D.; Liang, G.; Gauthier, M.; Li, R.; Sun, X. 3D Porous $LiFePO_4$/Graphene Hybrid Cathodes with Enhanced Performance for Li-Ion Batteries. J. Power Sources 2012, 208, 340−344.
(370) Wen, L.; Hu, X.; Luo, H.; Li, F.; Cheng, H. Open-Pore $LiFePO_4$/C Microspheres with High Volumetric Energy Density for Lithium Ion Batteries. Particuology 2015, 22, 24−29.
(371) Chou, S.-L.; Wang, J.-Z.; Liu, H.-K.; Dou, S.-X. Rapid Synthesis of $Li_4Ti_5O_{12}$ Microspheres as Anode Materials and Its Binder Effect for Lithium-Ion Battery. J. Phys. Chem. C 2011, 115, 16220−16227.
(372) Wang, M.; Yang, Y.; Zhang, Y. Synthesis of Micro-Nano Hierarchical Structured $LiFePO_4$/C Composite with Both Superior High-Rate Performance and High Tap Density. Nanoscale 2011, 3, 4434−4439.
(373) Yi, R.; Dai, F.; Gordin, M. L.; Chen, S.; Wang, D. Micro-Sized Si-C Composite with Interconnected Nanoscale Building Blocks as High-Performance Anodes for Practical Application in Lithium-Ion Batteries. Adv. Energy Mater. 2013, 3, 295−300.
(374) Cao, A.; Manthiram, A. Shape-Controlled Synthesis of High Tap Density Cathode Oxides for Lithium Ion Batteries. Phys. Chem. Chem. Phys. 2012, 14, 6724−6728.
(375) Han, F.; Li, D.; Li, W.-C.; Lei, C.; Sun, Q.; Lu, A.-H. Nanoengineered Polypyrrole-Coated Fe_2O_3@C Multifunctional Composites with an Improved Cycle Stability as Lithium-Ion Anodes. Adv. Funct. Mater. 2013, 23, 1692−1700.
(376) Zhao, H.; Wei, Y.; Qiao, R.; Zhu, C.; Zheng, Z.; Ling, M.; Jia, Z.; Bai, Y.; Fu, Y.; Lei, J.; et al. Conductive Polymer Binder for High-Tap-Density Nanosilicon Material for Lithium-Ion Battery Negative Electrode Application. Nano Lett. 2015, 15, 7927−7932.
(377) Lahiri, I.; Oh, S.-W.; Hwang, J. Y.; Cho, S.; Sun, Y.-K.; Banerjee, R.; Choi, W. High Capacity and Excellent Stability of Lithium Ion Battery Anode Using Interface-Controlled Binder-Free Multiwall Carbon Nanotubes Grown on Copper. ACS Nano 2010, 4, 3440−3446.
(378) Luo, S.; Wang, K.; Wang, J.; Jiang, K.; Li, Q.; Fan, S. Binder-Free $LiCoO_2$/Carbon Nanotube Cathodes for High-Performance Lithium Ion Batteries. Adv. Mater. 2012, 24, 2294−2298.
(379) Wu, M.; Xiao, X.; Vukmirovic, N.; Xun, S.; Das, P. K.; Song, X.; Olalde-Velasco, P.; Wang, D.; Weber, A. Z.; Wang, L.-W.; et al. Toward an Ideal Polymer Binder Design for High-Capacity Battery Anodes. J. Am. Chem. Soc. 2013, 135, 12048−12056.
(380) Liu, G.; Xun, S.; Vukmirovic, N.; Song, X.; Olalde-Velasco, P.; Zheng, H.; Battaglia, V. S.; Wang, L.; Yang, W. Polymers with

DOI: 10.1021/acs.chemrev.9b00405
Chem. Rev. XXXX, XXX, XXX−XXX

Tailored Electronic Structure for High Capacity Lithium Battery Electrodes. Adv. Mater. 2011, 23, 4679−4683.
(381) Xun, S.; Song, X.; Battaglia, V.; Liu, G. Conductive Polymer Binder-Enabled Cycling of Pure Tin Nanoparticle Composite Anode Electrodes for a Lithium-Ion Battery. J. Electrochem. Soc. 2013, 160, A849−A855.
(382) Guo, J.; Wang, C. A Polymer Scaffold Binder Structure for High Capacity Silicon Anode of Lithium-Ion Battery. Chem. Commun. 2010, 46, 1428−1430.
(383) Song, J.; Zhou, M.; Yi, R.; Xu, T.; Gordin, M. L.; Tang, D.; Yu, Z.; Regula, M.; Wang, D. Interpenetrated Gel Polymer Binder for High-Performance Silicon Anodes in Lithium-Ion Batteries. Adv. Funct. Mater. 2014, 24, 5904−5910.
(384) Choi, S.; Kwon, T.-w.; Coskun, A.; Choi, J. W. Highly Elastic Binders Integrating Polyrotaxanes for Silicon Microparticle Anodes in Lithium Ion Batteries. Science 2017, 357, 279−283.
(385) Li, Y.; El Gabaly, F.; Ferguson, T. R.; Smith, R. B.; Bartelt, N. C.; Sugar, J. D.; Fenton, K. R.; Cogswell, D. A.; Kilcoyne, A. L. D.; Tyliszczak, T.; et al. Current-Induced Transition from Particle-by-Particle to Concurrent Intercalation in Phase-Separating Battery Electrodes. Nat. Mater. 2014, 13, 1149−1156.
(386) Courtney, I. A.; Dahn, J. R. Electrochemical and in Situ X-Ray Diffraction Studies of the Reaction of Lithium with Tin Oxide Composites. J. Electrochem. Soc. 1997, 144, 2045−2052.
(387) Delmas, C.; Maccario, M.; Croguennec, L.; Le Cras, F.; Weill, F. Lithium Deintercalation in $LiFePO_4$ Nanoparticles Via a Domino-Cascade Model. Nat. Mater. 2008, 7, 665−671.
(388) Malik, R.; Zhou, F.; Ceder, G. Kinetics of Non-Equilibrium Lithium Incorporation in $LiFePO_4$. Nat. Mater. 2011, 10, 587−590.
(389) Lim, J.; Li, Y.; Alsem, D. H.; So, H.; Lee, S. C.; Bai, P.; Cogswell, D. A.; Liu, X.; Jin, N.; Yu, Y.-S.; et al. Origin and Hysteresis of Lithium Compositional Spatiodynamics within Battery Primary Particles. Science 2016, 353, 566−571.
(390) Armand, M.; Endres, F.; MacFarlane, D. R.; Ohno, H.; Scrosati, B. Ionic-Liquid Materials for the Electrochemical Challenges of the Future. Nat. Mater. 2009, 8, 621−629.
(391) Scrosati, B.; Garche, J. Lithium Batteries: Status, Prospects and Future. J. Power Sources 2010, 195, 2419−2430.
(392) Egerton, R. F.; Li, P.; Malac, M. Radiation Damage in the Tem and Sem. Micron 2004, 35, 399−409.
(393) Liu, X. H.; Huang, J. Y. In Situ Tem Electrochemistry of Anode Materials in Lithium Ion Batteries. Energy Environ. Sci. 2011, 4, 3844−3860.
(394) Park, J. Y.; Kim, S. J.; Chang, J. H.; Seo, H. K.; Lee, J. Y.; Yuk, J. M. Atomic Visualization of a Non-Equilibrium Sodiation Pathway in Copper Sulfide. Nat. Commun. 2018, 9, 922.
(395) Zhang, W.; Yu, H.-C.; Wu, L.; Liu, H.; Abdellahi, A.; Qiu, B.; Bai, J.; Orvananos, B.; Strobridge, F. C.; Zhou, X.; et al. Localized Concentration Reversal of Lithium During Intercalation into Nanoparticles. Sci. Adv. 2018, 4, No. eaao2608.
(396) Lin, F.; Liu, Y.; Yu, X.; Cheng, L.; Singer, A.; Shpyrko, O. G.; Xin, H. L.; Tamura, N.; Tian, C.; Weng, T.-C.; et al. Synchrotron X-Ray Analytical Techniques for Studying Materials Electrochemistry in Rechargeable Batteries. Chem. Rev. 2017, 117, 13123−13186.
(397) Wolf, M.; May, B. M.; Cabana, J. Visualization of Electrochemical Reactions in Battery Materials with X-Ray Microscopy and Mapping. Chem. Mater. 2017, 29, 3347−3362.
(398) Li, Y.; Li, Y.; Pei, A.; Yan, K.; Sun, Y.; Wu, C.-L.; Joubert, L.-M.; Chin, R.; Koh, A. L.; Yu, Y.; et al. Atomic Structure of Sensitive Battery Materials and Interfaces Revealed by Cryo−Electron Microscopy. Science 2017, 358, 506−510.
(399) Harks, P. P. R. M. L.; Mulder, F. M.; Notten, P. H. L. In Situ Methods for Li-Ion Battery Research: A Review of Recent Developments. J. Power Sources 2015, 288, 92−105.
(400) Pfeiffer, F. X-Ray Ptychography. Nat. Photonics 2018, 12, 9−17.
(401) Ulvestad, A.; Singer, A.; Cho, H.-M.; Clark, J. N.; Harder, R.; Maser, J.; Meng, Y. S.; Shpyrko, O. G. Single Particle Nanomechanics in Operando Batteries Via Lensless Strain Mapping. Nano Lett. 2014, 14, 5123−5127.
(402) Ulvestad, A.; Singer, A.; Clark, J. N.; Cho, H. M.; Kim, J. W.; Harder, R.; Maser, J.; Meng, Y. S.; Shpyrko, O. G. Topological Defect Dynamics in Operando Battery Nanoparticles. Science 2015, 348, 1344−1347.
(403) Dollins, C. C. Nucleation on Dislocations. Acta Metall. 1970, 18, 1209−1215.
(404) Thibault, P.; Dierolf, M.; Menzel, A.; Bunk, O.; David, C.; Pfeiffer, F. High-Resolution Scanning X-Ray Diffraction Microscopy. Science 2008, 321, 379−382.
(405) Shapiro, D. A.; Yu, Y.-S.; Tyliszczak, T.; Cabana, J.; Celestre, R.; Chao, W.; Kaznatcheev, K.; Kilcoyne, A. L. D.; Maia, F.; Marchesini, S.; et al. Chemical Composition Mapping with Nanometre Resolution by Soft X-Ray Microscopy. Nat. Photonics 2014, 8, 765−769.
(406) Li, Y.; Meyer, S.; Lim, J.; Lee, S. C.; Gent, W. E.; Marchesini, S.; Krishnan, H.; Tyliszczak, T.; Shapiro, D.; Kilcoyne, A. L. D.; et al. Effects of Particle Size, Electronic Connectivity, and Incoherent Nanoscale Domains on the Sequence of Lithiation in $LiFePO_4$ Porous Electrodes. Adv. Mater. 2015, 27, 6591−6597.
(407) Yu, Y.-S.; Farmand, M.; Kim, C.; Liu, Y.; Grey, C. P.; Strobridge, F. C.; Tyliszczak, T.; Celestre, R.; Denes, P.; Joseph, J.; Krishnan, H.; Maia, F. R. N. C.; Kilcoyne, A. L. D.; Marchesini, S.; Leite, T. P. C.; Warwick, T.; Padmore, H.; Cabana, J.; Shapiro, D. A. Three-Dimensional Localization of Nanoscale Battery Reactions Using Soft X-Ray Tomography. Nat. Commun. 2018, 9, 921.
(408) Murugan, A. V.; Muraliganth, T.; Manthiram, A. Comparison of Microwave Assisted Solvothermal and Hydrothermal Syntheses of Lifepo4/C Nanocomposite Cathodes for Lithium Ion Batteries. J. Phys. Chem. C 2008, 112, 14665−14671.
(409) Lu, J.; Chen, Z.; Ma, Z.; Pan, F.; Curtiss, L. A.; Amine, K. The Role of Nanotechnology in the Development of Battery Materials for Electric Vehicles. Nat. Nanotechnol. 2016, 11, 1031−1038.
(410) Wang, Y.; Cao, G. Developments in Nanostructured Cathode Materials for High-Performance Lithium-Ion Batteries. Adv. Mater. 2008, 20, 2251−2269.
(411) Wu, H.; Cui, Y. Designing Nanostructured Si Anodes for High Energy Lithium Ion Batteries. Nano Today 2012, 7, 414−429.
(412) Ma, D.; Cao, Z.; Hu, A. Si-Based Anode Materials for Li-Ion Batteries: A Mini Review. Nano-Micro Lett. 2014, 6, 347−358.
(413) Wang, K.; Huang, Y.; Wang, M.; Yu, M.; Zhu, Y.; Wu, J. Pvd Amorphous Carbon Coated 3d $NiCo_2O_4$ on Carbon Cloth as Flexible Electrode for Both Sodium and Lithium Storage. Carbon 2017, 125, 375−383.
(414) Chen, X.; Gerasopoulos, K.; Guo, J.; Brown, A.; Wang, C.; Ghodssi, R.; Culver, J. N. Virus-Enabled Silicon Anode for Lithium-Ion Batteries. ACS Nano 2010, 4, 5366−5372.
(415) Wang, W.; Epur, R.; Kumta, P. N. Vertically Aligned Silicon/Carbon Nanotube (Vascnt) Arrays: Hierarchical Anodes for Lithium-Ion Battery. Electrochem. Commun. 2011, 13, 429−432.
(416) Hu, L.; Wu, H.; Hong, S. S.; Cui, L.; McDonough, J. R.; Bohy, S.; Cui, Y. Si Nanoparticle-Decorated Si Nanowire Networks for Li-Ion Battery Anodes. Chem. Commun. 2011, 47, 367−369.
(417) Aravindan, V.; Jinesh, K. B.; Prabhakar, R. R.; Kale, V. S.; Madhavi, S. Atomic Layer Deposited (ALD) SnO_2 Anodes with Exceptional Cycleability for Li-Ion Batteries. Nano Energy 2013, 2, 720−725.
(418) Foong, T. R. B.; Shen, Y.; Hu, X.; Sellinger, A. Template-Directed Liquid Ald Growth of TiO_2 Nanotube Arrays: Properties and Potential in Photovoltaic Devices. Adv. Funct. Mater. 2010, 20, 1390−1396.
(419) Yu, X. Q.; He, Y.; Sun, J. P.; Tang, K.; Li, H.; Chen, L. Q.; Huang, X. J. Nanocrystalline Mno Thin Film Anode for Lithium Ion Batteries with Low Overpotential. Electrochem. Commun. 2009, 11, 791−794.
(420) Kuwata, N.; Kumar, R.; Toribami, K.; Suzuki, T.; Hattori, T.; Kawamura, J. Thin Film Lithium Ion Batteries Prepared Only by Pulsed Laser Deposition. Solid State Ionics 2006, 177, 2827−2832.

DOI: 10.1021/acs.chemrev.9b00405
Chem. Rev. XXXX, XXX, XXX−XXX

(421) Fu, K.; Xue, L.; Yildiz, O.; Li, S.; Lee, H.; Li, Y.; Xu, G.; Zhou, L.; Bradford, P. D.; Zhang, X. Effect of Cvd Carbon Coatings on Si@ Cnf Composite as Anode for Lithium-Ion Batteries. Nano Energy 2013, 2, 976−986.
(422) Zhang, H.; Deng, Q.; Zhou, A.; Liu, X.; Li, J. Porous $Li_2C_8H_4O_4$ Coated with N-Doped Carbon by Using Cvd as an Anode Material for Li-Ion Batteries. J. Mater. Chem. A 2014, 2, 5696−5702.
(423) Jung, Y. S.; Lu, P.; Cavanagh, A. S.; Ban, C.; Kim, G.-H.; Lee, S.-H.; George, S. M.; Harris, S. J.; Dillon, A. C. Unexpected Improved Performance of Ald Coated $LiCoO_2$/Graphite Li-Ion Batteries. Adv. Energy Mater. 2013, 3, 213−219.
(424) Kato, T.; Hamanaka, T.; Yamamoto, K.; Hirayama, T.; Sagane, F.; Motoyama, M.; Iriyama, Y. In-Situ $Li_7La_3Zr_2O_{12}$/$LiCoO_2$ Interface Modification for Advanced All-Solid-State Battery. J. Power Sources 2014, 260, 292−298.
(425) Yu, X.; Chen, X.; Buchholz, D. B.; Li, Q.; Wu, J.; Fenter, P. A.; Bedzyk, M. J.; Dravid, V. P.; Barnett, S. A. Pulsed Laser Deposition and Characterization of Heteroepitaxial $LiMn_2O_4$/$La_{0.5}Sr_{0.5}CoO_3$ Bilayer Thin Films as Model Lithium Ion Battery Cathodes. ACS Appl. Nano Mater. 2018, 1, 642−653.
(426) Schichtel, P.; Geiß, M.; Leichtweiß, T.; Sann, J.; Weber, D. A.; Janek, J. On the Impedance and Phase Transition of Thin Film All-Solid-State Batteries Based on the $Li_4Ti_5O_{12}$ System. J. Power Sources 2017, 360, 593−604.
(427) Kozen, A. C.; Pearse, A. J.; Lin, C.-F.; Noked, M.; Rubloff, G. W. Atomic Layer Deposition of the Solid Electrolyte Lipon. Chem. Mater. 2015, 27, 5324−5331.
(428) Sakuda, A.; Hayashi, A.; Ohtomo, T.; Hama, S.; Tatsumisago, M. All-Solid-State Lithium Secondary Batteries Using $LiCoO_2$ Particles with Pulsed Laser Deposition Coatings of Li_2S−P_2S_5 Solid Electrolytes. J. Power Sources 2011, 196, 6735−6741.
(429) Kim, S.; Hirayama, M.; Taminato, S.; Kanno, R. Epitaxial Growth and Lithium Ion Conductivity of Lithium-Oxide Garnet for an All Solid-State Battery Electrolyte. Dalton Trans 2013, 42, 13112−13117.
(430) Bang, G. S.; Nam, K. W.; Kim, J. Y.; Shin, J.; Choi, J. W.; Choi, S.-Y. Effective Liquid-Phase Exfoliation and Sodium Ion Battery Application of MoS_2 Nanosheets. ACS Appl. Mater. Interfaces 2014, 6, 7084−7089.
(431) Wei, D.; Grande, L.; Chundi, V.; White, R.; Bower, C.; Andrew, P.; Ryhänen, T. Graphene from Electrochemical Exfoliation and Its Direct Applications in Enhanced Energy Storage Devices. Chem. Commun. 2012, 48, 1239−1241.
(432) Hernandez, Y.; Nicolosi, V.; Lotya, M.; Blighe, F. M.; Sun, Z.; De, S.; McGovern, I. T.; Holland, B.; Byrne, M.; Gun'Ko, Y. K.; et al. High-Yield Production of Graphene by Liquid-Phase Exfoliation of Graphite. Nat. Nanotechnol. 2008, 3, 563−568.

DOI: 10.1021/acs.chemrev.9b00405
Chem. Rev. XXXX, XXX, XXX−XXX